UNIVERSIDAD AUTÓNOMA DE NUEVO LEÓN
FACULTAD DE INGENIERÍA MECÁNICA Y ELÉCTRICA

THESIS

ACOUSTO-ULTRASONICS-BASED STRUCTURAL HEALTH MONITORING SYSTEM IN SINGLE LAP SHEAR BONDED JOINTS

PRESENTED BY

RODRIGO SALAZAR COLUNGA

AS PARTIAL FULFILLMENT OF THE REQUIREMENTS FOR THE DEGREE OF MASTER OF SCIENCE IN AERONAUTICAL ENGINEERING WITH ORIENTATION IN STRUCTURES

OCTOBER, 2022

UNIVERSIDAD AUTÓNOMA DE NUEVO LEÓN
FACULTAD DE INGENIERÍA MECÁNICA Y ELÉCTRICA
SUBDIRECCIÓN DE ESTUDIOS DE POSGRADO

THESIS

ACOUSTO-ULTRASONICS-BASED STRUCTURAL HEALTH MONITORING SYSTEM IN SINGLE LAP SHEAR BONDED JOINTS

PRESENTED BY

RODRIGO SALAZAR COLUNGA

AS PARTIAL FULFILLMENT OF THE REQUIREMENTS FOR THE DEGREE OF MASTER OF SCIENCE IN AERONAUTICAL ENGINEERING WITH ORIENTATION IN STRUCTURES

SAN NICOLÁS DE LOS GARZA, NUEVO LEÓN, MÉXICO OCTOBER, 2022

UNIVERSIDAD AUTÓNOMA DE NUEVO LEÓN
Facultad de Ingeniería Mecánica y Eléctrica
Posgrado

Los miembros del Comité de Evaluación de Tesis recomendamos que la Tesis "Acousto-ultrasonics-based Structural Health Monitoring System in Single Lap Shear Bonded Joints", realizada por el estudiante Rodrigo Salazar Colunga, con número de matrícula 1719101, sea aceptada para su defensa como requisito parcial para obtener el grado de Maestría en ingeniería aeronáutica con orientación en estructuras.

El Comité de Evaluación de Tesis

Dr. Pedro López Cruz
Director

Dr. Marcías Martínez
Co-director

Dr. Diego Francisco Ledezma Ramírez
Revisor

Dr. Pablo Ernesto Tapia González
Revisor

Dr. Martín Castillo Morales
Revisor

Vo.Bo.

Dr. Simón Martínez Martínez
Subdirector de Estudios de Posgrado

Institución 190001

Programa 563511

Acta Núm. 4145

Ciudad Universitaria, a 24 de marzo del 2023

Abstract

In the Structural Health Monitoring (SHM) field, Acousto-Ultrasonic (AU) methods are active techniques successfully used for detecting the presence of damage and localizing it using Guided Lamb waves (GLWs) on plate-like structures. It is envisioned to be of great potential use for assessing damages within bonded structures. These structures are set to achieve weight reduction objectives in the aerospace industry. The goal of SHM is to ensure the safety of these type of structures. To achieve these goals, certifications requirements must be met. A numerical AU Time Reversal Method (TRM) method is being considered for damage detection of an Aluminum Alloy 5083 Single Lap Shear Joint (SLSJ). The joint considered in our study is adhesively bonded with a viscoelastic ProSet® ADV176/276 adhesive system [1] and manufactured following the configuration outlined in ASTM Standard D1002. Standard material characterization testing following ASTM E8 and D638 was evaluated as part of this study. The structural integrity of the bonded joints was analyzed though a computational finite element model (FEM) developed in ABAQUS CAE^{TM}. A pitch-catch active sensing method with piezoelectric Lead Zirconate Titanate (PZT) transducers and the use of a 5-cycle Hanning window was considered for interrogating the health of the structure. This study focused on the use of SHM systems to assess the structural integrity of bonded joints without considering environmental effects. The results obtained in this study show how the TRM method can be successfully applied to bonded joints when edge reflections are controlled on a pristine and damage configuration. Moreover, the introduction of an innovative technique to introduce damage on FEA models to make an accurate damage detection of real-like damages. The results obtained as part of this study open the need for further studies.

Acknowledgements

Firstly, I would like to thank my supervisor Professor Pedro Lopez for guiding me during the first year of my master's degree and for giving me the possibility to complete my thesis in the United States of America.

Secondly, special thanks to my co-supervisor Professor Marcias Martinez from Clarkson University, who I am happy to say, he was not just my thesis co-supervisor but ultimately, he has become a great mentor and friend. He believed and encouraged me from the first day along while providing me all the resources and guidance for the realization of this thesis. His enthusiasm, patience and immense expertise motivated me through the nine months I spend at his laboratory. I am very grateful to him for everything.

It is my great fortune to have met and befriended many great people throughout my period in the US. Joshua Alamo, Juliana Garcia, Monica Damiani, Dr. Daniel Massana, Anna Tverdokhlebova, Dr. Alessandro Baldassare, Dr. Lissette Fernandez, Todd Mull and Minhaz Morshed, who make Potsdam feel like home. I am very grateful to them for the great moments, encouraging words and their friendship.

I would like to also thank Diana Carvalho. She has been a decisive support from the beginning to the end of my degree. I am deeply grateful to her for listening to my long monologues and encouraged me not to give up in the though moments.

More importantly, I would like to express my special thanks to all my family, especially my parents. Their unconditional love and support were a significant driving force during this stage of my life. I am thankful for them to remind me every day that everything that we achieve is thanks to God.

Finally, I would like to thank the National Council for Science and Technology (CONACYT) for the funding provided during the degree.

This work relates to Department of Navy award N00014-21-1-2057 issued by the Office of Naval Research. The United States Government has a royalty-free license throughout the world in all copyrightable material contained herein. Any opinions, findings, and conclusions or recommendations expressed in this material are those of the author(s) and do not necessarily reflect the views of the Office of Naval Research.

Acronyms

AA	Aluminum Alloy
AE	Acoustic Emission
ASTM	American Society for Testing and Materials
AU	Acousto-Ultrasonic
BdB	Broad-Band
CAD	Computer-aided design
CAE	Computer-aided engineering
DI	Damage Index
DIC	Digital Image Correlation
FAA	Federal Aviation Administration
FCTF	Frequencies Compensation Transfer Function
FEM	Finite Element Model
GLWs	Guided Lamb waves
HolSIP	Holistic Structural Integrity Process
HW	Hann Window
LOV	Limit of Validity
NDE	Non-Destructive Evaluation
NDI	Non-Destructive Inspection
NRB	Non-Reflective Boundaries
NwB	Narrow-Band
PLB	Pencil-Lead Break
PZT	Lead Zirconate Titanate
SHM	Structural Health Monitoring
SLSJ	Single Lap Shear Joints
SRM	Stiffness Reduction Method
TRM	Time Reversal Method
UTS	Ultimate Tensile Stress

Table of Contents

List of Figures

List of Tables

2. Introduction

2.1. Background and motivation

The mandate for greater fuel efficiency has given rise to the development of lightweight structures without compromising safety across the aerospace industry. Adhesively bonded joints are one of the techniques envisioned for eliminating mechanical fasteners in structures, thus providing the desired weight reduction. However, the presence of defects in the adhesive bond line may compromise the structural integrity of the adhesively bonded joints and potentially lead to premature failures. Structural Health Monitoring (SHM) systems have the possibility to reduce failure risks on structural joints. This is achieved with information captured by SHM systems, while processing algorithms inform the user of potential integrity issues within the structure. The aerospace community has been working on identification and monitoring of crack growth on critical components. Assessment of the development of damage is fundamental for employing bonded joints in the aeronautical industry. SHM systems for assessing damages within structures are commonly categorized as passive or active sensing techniques. Acousto-ultrasonic (AU) is one of the active techniques that when integrated into a structure can gather real-time data of the structural integrity of these joints and thus provide an early warning. It is envisioned that the use of this technique will lead to the implementation of a novel AU-based SHM on bonded joints.

2.2. Scientific question

Being able to monitor and predict when a bonded joint will start to fail is one of the primary requirements by the certification authorities for their widespread usage in primary structures [2], [3]. Guided Lamb waves (GLWs) on plate-like structures have been successfully studied due to their ability to travel long distances along a structure. These types of waves can be generated and recorded using piezoelectric transducers such as, Lead Zirconate Titanate (PZT) actuators and sensors. In a traditional scenario, a transducer Y registers an emitted signal through the structure transmitted from transducer X. The sensed signal, after post-processing, is prone to indicate the presence of damage signatures. Following that, if a time reversal method is employed to the received signal on transducer Y and send it back to transducer X, this can be compared with the initial emitted one to determinate the presence of damage. One of the main challenges for damage detection on structural single lap shear bonded joints is the limited range for usable frequencies. Therefore, with the use of an AU-based SHM system, this works aims at assessing the integrity of the adhesive on single lap shear bonded joints, to answer the main scientific question:

- Is it possible to monitor the integrity and determine when the adhesive of single lap shear bonded joints start to fail using time reversibility of Lamb waves?

2.3. Objective and approach

To answer the scientific question, the following approach will be considered. The first step was to perform an adequate literature review about GLWs and Time Reversal Method (TRM) found in the open literature. Experimental and ABAQUS CAE^{TM} computational model of a metal-to-metal Single Lap Shear Joint (SLSJ) was developed based on ASTM D1002 standard dimensions. The material properties used as input for the finite element model were gathered from standard mechanical testing and technical data sheets from suppliers [1]. The finite element model of the AU-based damage detection system was developed by preliminary results collected from different models' iterations to monitor the integrity of the SLSJ bond line.

2.4. Dissertation outline

This dissertation is divided into 6 chapters:

- Chapter 1 encloses the motivations of this study with the to-be answered scientific question, the objectives, approach, and the dissertation outline.
- Chapter 3 contains a literary review of the bonded joints, description of SHM systems and AU, the theory of elastic waves including the explanation of GLWs, and its usage in the SHM field. TRM concepts and applications are also explained in this chapter.

- Chapter 4 consists of a state-of-the-art on the use of Lamb waves in the SHM field and the application of the TRM. This section will address the gaps of reliable damage detection on bonded joints and the importance of this thesis work.
- Chapter 5 consists of a detailed explanation of the methodology employed for the AU-based SHM. This includes material characterization, SLSJ manufacture and computational considerations for the finite element model.
- Chapter 6 mainly focus on the acoustic-ultrasonic results obtained from the finite element model for the fulfillment of this thesis dissertation.
- Chapter 7 is a discussion of the results obtained from the finite element model and outlines the conclusions. It also presents suggestions and future works on this topic.

3. Literary review

3.1. Bonded joints

The tendency to fabricate bonded structures in the aerospace industry is growing fast over the use of mechanical fasteners. They provide more advantages on the structure, such as, weight reductions, the absence of stress concentrations and ability to join dissimilar materials [4], [5]. On the other hand, bonded joints are still unreliable on primary aeronautical structures. To achieve widespread acceptance of bonded joints in primary structures, the certification authorities have very specific regulations. According to the Advisory Circular 20-107B from the Federal Aviation Administration (FAA), any bonded joint must be substantiated by: i) applying mechanical fasteners in order to allow for a fail-safe condition; ii) proof testing of each individual joint; or iii) reliable and consistent monitoring techniques that will worn of the loss of structural integrity [2]. The existing Non-Destructive Inspection (NDI) methods are currently not mature enough for ensuring a reliable and consistent monitoring. Reliable SHM techniques are intended to fulfill this structural need. Being able to validate the load capacity can prevent the catastrophic loss of the airplane. The limit load capacity property relies primarily on manufacturing processes of the bonded joints, however proof testing to limit load and raise the question on the production of defects after testing. Potential development of defects such as voids, inclusions, kissing bonds and pre-existing cracks, as shown on Figure 1 [6], are prone to be present on SLSJ. The existence of defects result in a severe reduction of the bond strength, which will cause a threat on the reliability of the structural integrity of the bonded joint [7]–[10].

These types of defects cannot always be avoided in the manufacturing process hence the need to provide real-time information about the existence and evolution of damages in the structure. This is essential for the safe usage of adhesives in primary aircraft fuselage and wing structures. Integrated SHM sensors embedded in the structure may provide a suitable solution to achieve the certification of adhesively bonded joints required by the FAA.

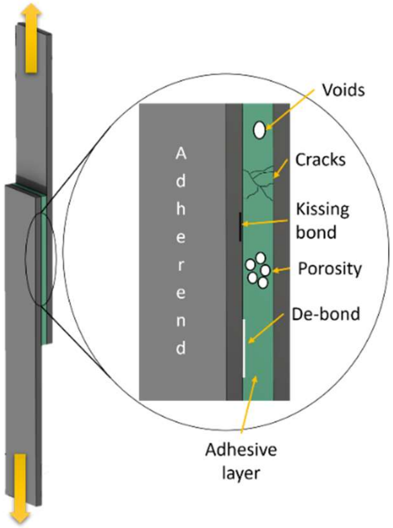

Figure 1. Types of damages on single lap shear bonded joints [6]

3.2. Structural health monitoring

An intentional or unintentional change in a structure/mechanical system adversely affecting the ability to perform its designed function, at any moment of the service life is known as damage.

Unfortunate accidents such as Aloha Airline Flight 243 shown in Figure 2 [11], serve as a reminder and motivation to the manufacturers and maintenance teams to maintain safety of aeronautical structures. SHM technologies are meant to help to avoid catastrophes like this one.

Figure 2. Damage Cause to Aloha Airline Flight 243 [11]

SHM, a non-destructive and continuous monitoring of structural systems, has presented itself as a solution as a cost-effective and reliable damage detection method [12]. SHM systems consist of a permanently integrated network of sensors, such as PZT sensors attached to the structure, on board data acquisition, computing facilities, and algorithms to assess the structural integrity as shown in Figure 3 [13][14].

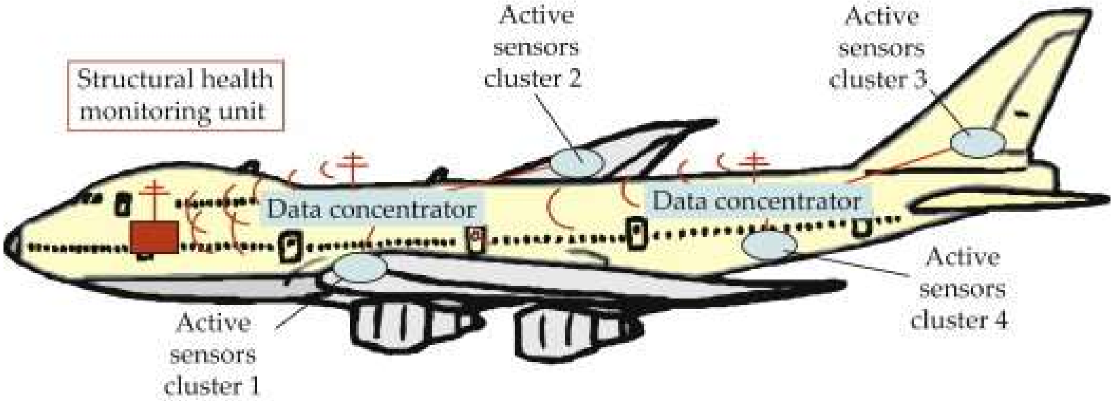

Figure 3. Generic illustration of a SHM system [13]

These integrated systems have the main purpose to reduce complicated inspections, unnecessary maintenance's costs, and catastrophic failures by reaching the safety required standards for the structures during their service life (Limit of Validity (LOV) range). This concept is a limit to life extension of structures, where any nucleation nor propagation of damage will occur in the structure before reaching the limit. The LOV has to be indicated and supported by testing evidence, analysis and, if available, service experience [15].

Many researchers and organizations have their own definition of SHM. An adequate concept of SHM for this work was taken from Farrar and Worden (2007) as: "the observation of a structure or mechanical system over time using periodically spaced measurements, the extraction of damage sensitive features from these measurements, and the statistical analysis of these features to determine the current state of health"[16]. Sielski (2012) describes an effective SHM as systems that are able to monitor the operational loads, identify reduction in performance, early damage detection, perform a prognosis analysis about the potential failure of the structure, and provide an execution plan of corrective maintenance [17]. This is sustained by Lammering et al. 2018 where the objectives of an effective SHM system are presented as being able to detect the: a) existence of a damage; b) location of the damage; c) size of the damage and d) the damage type [18]. Balageas et al. (2006) explain some of the most common types of SHM techniques such as, vibration-based, fiber-optic sensing and PZT transducers techniques [19]. State of the art of the different techniques have been documented by Montalvao et al. (2006) [20], López-Higuera et al. (2010) [21], Di Sante (2015) [22], Das et al. (2016) [23], Güemes et al. (2018) [24], etc.

3.3. Acousto-ultrasonics

Acousto-Ultrasonics is one of the methods that have been used to determine the internal damages in materials using non-destructive techniques [25]. AU is one of the most cost-effective in-situ method of SHM due to the capability of achieving the objectives, in practicality and costs [26]. Hence, this method has been frequently used for real time monitoring of the integrity of structures.

AU is an active sensing method, which means that an actuator and a sensor are required. Pitch-catch is one the most common active sensing techniques. The objective of the different AU techniques, explained by Vary (1988), relies on disturbing the material with benign stress waves produced by a controlled external source such as a PZT transducer [27]. Ultrasonic waves are acoustic waves operating in a frequency range from above the upper limit of the human hearing (20 kHz) to more than 20 MHz. Figure 4 [28] shows the complete sound spectrum.

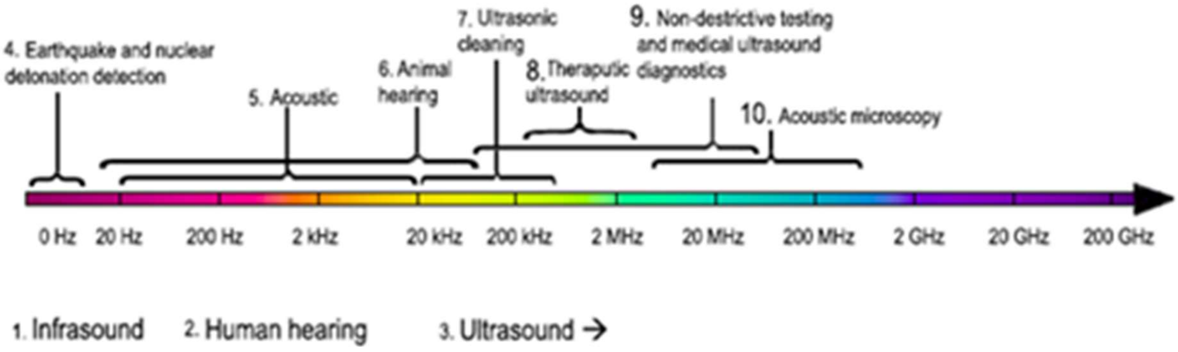

Figure 4. Sound spectrum [28]

The usage of ultrasonic waves allows damage detection in structures. A schematic representation of an active sensing method is presented in Figure 5 [29]. AU-based systems achieve local damage detection and localization by placing actuators to perform excitation, and sensors, to have a controlled diagnostic of the structure.

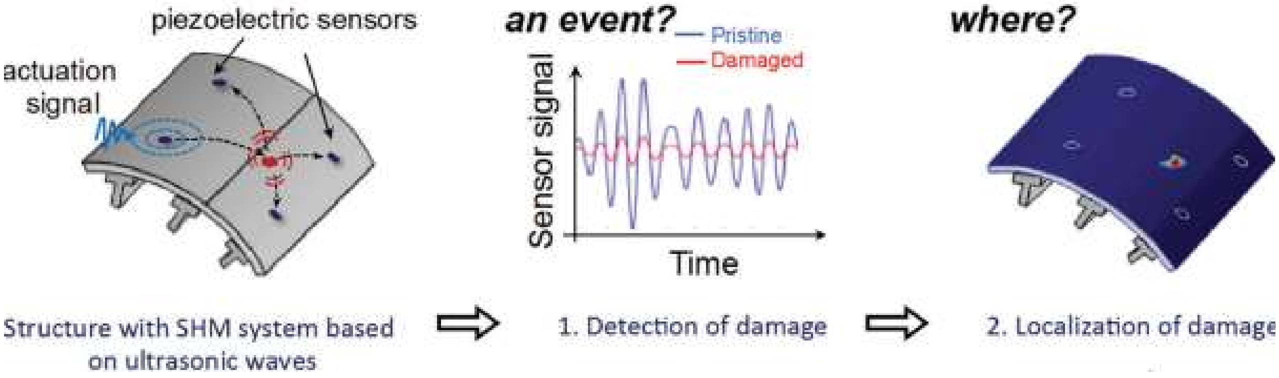

Figure 5. Schematic representation of active sensing [29]

Smaller or larger defects can be detected by employing a characteristic operating frequency. Therefore, while a higher frequency can be used to detect smaller damages, the signal may encounter problems in penetrating thick structures. Lower frequencies travel easier through material thickness but can detect larger defects. The literature review shows good results on damage detection while using active sensing methods on metal plate-like structures. The studies to date about SHM system using AU methods for damage detection in metal-to-metal bonded joints are limited to date.

3.4. Guided Lamb waves

Damage can be quantified by examining the unique wave scattering phenomena and mode conversion of a signal when transmitted on a structure [30].

3.4.1. Theory of elastic waves

Mechanical waves propagating in an elastic medium caused by forces along the surface and through the thickness of a structure are called elastic waves. Ostachowicz et al. (2008) presented them in their book as waves that propagate particles of a medium as they move away from the wave source [31]. The AU-based SHM systems are based on elastic wave propagation. Elastic waves generally travel through material surfaces without causing any permanent structural change.

This advantage of elastic waves allows to induce them into a structure to monitor if discontinuities or structural damages are present. This is achieved through examination of the induced signal after it has traveled through the structure.

Giurgiutiu (2014) shows the main types of waves that can exist in elastic solids. These are presented in Table 1 [13], which presence is dependent on the constraints and boundary conditions imposed on the elastic medium.

Table 1. Types of waves and their properties [13].

Wave type	Property
Pressure; P-waves; Longitudinal	Characterized by an alternated compression and rarefaction behavior in the particle motion. This motion is in the parallel direction of the propagated wave, thus in the longitudinal direction.
Shear; S-waves or transverse waves	The transverse movement of the particle is the main characteristic of these waves. The particle in the transverse movement can travel in a horizontal or vertical direction. Thus, receiving the name of SH and SV, horizontal shear, and vertical shear wave respectively.
Flexural or bending waves	The motion of the particle is elliptical. The plane sections remain plane.
Rayleigh; surface acoustic waves or SAW	The motion of the particle is elliptical. The amplitude decays quickly with depth.
Lamb waves; guided plates waves or GLWs	The motion of the particle is elliptical. Free-surface conditions on the upper and lower surfaces of plate surface.

In this work, the use of Lamb waves for a damage detection on a SHM system are being study. GLWs are generated by the reflections in the boundary's surfaces of longitudinal and shear waves in an elastic solid media. Where pressure waves and shear waves are shown in Figure 6 [32].

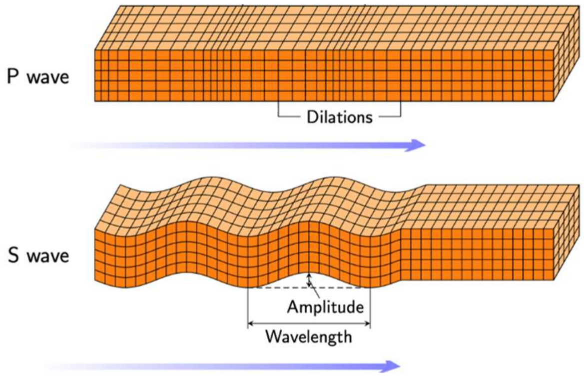

Figure 6. Longitudinal and Shear wave. [32]

Both waves, P-Waves and SV-Waves, can coexist at the same time in the media resulting in the mentioned GLWs. They consist of a stationary waves arrangement through the thickness, which creates the Lamb waves modes, with an itinerant behavior along the direction of the waves [31]. The calculation of the components for wave speeds of P-and SV-waves, respectively C_L and C_T, in isotropic materials are defined by Eqs. (1) and (2) where E represents the Young's modulus, ρ the density and ν the Poisson's ratio of the medium [30].

$$C_L = \sqrt{\frac{E(1-\nu)}{\rho(1+\nu)(1-2\nu)}} \tag{1}$$

$$C_T = \sqrt{\frac{E}{2\rho(1+2\nu)}} \tag{2}$$

3.4.2. Guided Lamb waves

Guided Lamb waves are one of the most used elastic waves for detection of cracks in thin-plate and tubular materials. Discovered by Horace Lamb in 1917 [33] for isotropic materials, but only employed as a new tool for damage detection by Worlton in 1961 [34]. These waves, possess the sensitivity to detect damage as a matter of interferences while propagating through a media. GLWs can travel long distances losing minimal energy, making them suitable for structural applications.

As stated before, the P-and SV-waves of the GLWs co-exist in the structure in superposition. This superposition is originated from the reflection of both waves on the upper and lower surfaces of the plates, creating an infinite number of modes at the same time. Using the wave speed equations (1) and (2), Su and Ye (2009) defined the general description of GLWs in Eq.(3) from the plain strain and boundaries conditions in an isotropic and homogeneous plates [30], [35]. Where *h* is the half thickness of the plate, *k* the wavenumber, *λ* the wavelength of the wave, *ω* is the frequency, while *p* and *q* are described in Eqs. (4) and (5) [30].

$$\frac{\tan(qh)}{\tan(ph)} = \frac{4k^2 qp\mu}{(\lambda k^2 + \lambda p^2 + 2\mu p^2)(k^2 - q^2)} \tag{3}$$

$$p^2 = \frac{\omega^2}{C_L^{\,2}} - k^2 \tag{4}$$

$$q^2 = \frac{\omega^2}{C_T^{\,2}} - k^2 \tag{5}$$

Substituting Eqs. (1) through (4) into Eq. (5) and determining the ratio of the tangent properties of the equations, it is possible to obtain two solutions to the equation, these solutions represent the anti-symmetric and symmetric behavior of GLWs. Eqs. (6) and (7) imply that GLWs embody in a thin-plate as antisymmetric A_i and symmetric S_i modes [30]. This is visualized on Figure 6, where the P-and SV-waves creates both modes, respectively. Where i = 0, 1…., meaning that the generated modes in a plate are infinite and subscript zero being the lowest order. This is because higher order modes are developed due to the number of solutions from Eq. (5).

$$\frac{\tan(qh)}{\tan(ph)} = -\frac{(k^2 - q^2)^2}{4k^2 qp} \tag{6}$$

$$\frac{\tan(qh)}{\tan(ph)} = -\frac{4k^2 qp}{(k^2 - q^2)^2} \tag{7}$$

These equations are commonly known as Rayleigh-Lamb equations [36]. It is important to note that A_0 and S_0 are considered the important ones in this study-case. Figure 6 shows the behavior of both modes in an isotropic and homogeneous plate. It also shows that symmetric modes can also be called longitudinal modes due to their radial in-plane displacement of particles, while the antisymmetric, due to their out-of-plane behavior are known as flexural.

Since Eq. (1) and (2) calculate the speed of the wave depending on the medium of propagation, it should also be noted the existence of a propagation speed of the waves, also known as phase velocity, C_p. Phase velocity represents the rate at which a point in the wave is propagating through the medium. This does not mean the velocity of the particles, if not the propagation velocity of the wave phase considering a single frequency from a wave signal range which is related to the wavelength, $\lambda_{wave.}$ The phase velocity C_p can be calculated using equation (8) where k is obtained from Eq.(9) [30].

$$C_P = \frac{\lambda}{T} = \lambda f = \frac{\omega}{k} \tag{8}$$

$$k = \frac{2\pi}{\lambda_{wave}} \tag{9}$$

In the case of experiments using GLWs, where the two waves are co-existing, a sum of both waves is needed to obtain only one wave that contains the two frequency components of each wave. This means that when two or more waves interact with one another, they possess a multi-frequency wave, and the phase velocity is no longer adequate, as such the group velocity, C_g, is considered.

The group velocity, Eq. (10) [37], known as a complete form of the amplitudes of the multi-waves, or as an envelope of the waves. This velocity is of special interest on experimentation applications because the propagation of the energy of the wave is predominantly carried by wave packets that propagate with this group velocity. The C_g depends on the thickness of the material and the frequencies used.

$$C_g = \left[\frac{dk}{d\omega} \right]^{-1} \tag{10}$$

3.4.2.1. Dispersion

The dispersion phenomenon of GLWs can be noticed from Eq (6) and (7), where the wave velocities have a relationship with the frequency-thickness (wave frequency-thickness of the studied plate) and is related to the anti-symmetric and symmetric modes. Eq (6) and (7) are also known as dispersion equations if they are re-arranged as in Eq (11) and (12) [30].

$$\frac{\tan(qh)}{q} + \frac{4k^2 p \tan(ph)}{(k^2 - q^2)^2} = 0 \tag{11}$$

$$q \tan(qh) + \frac{(k^2 - q^2)^2 \tan(ph)}{4k^2 p} = 0 \tag{12}$$

Figure 7 represents an example plot of the velocity dispersion equation of an isotropic plate [38]. The dispersion curves show the correlation between the phase or group velocity and the frequency-thickness. As mentioned before, the Lamb wave modes tend to an unlimited real solutions of wavenumbers at a certain frequency [30]. The possible existing modes on an isotropic material can be seen on the dispersion curves. From the unlimited anti-symmetric and symmetric modes, there are two that are of major interest. These modes are called fundamental modes and represented as A_0 and S_0 modes.

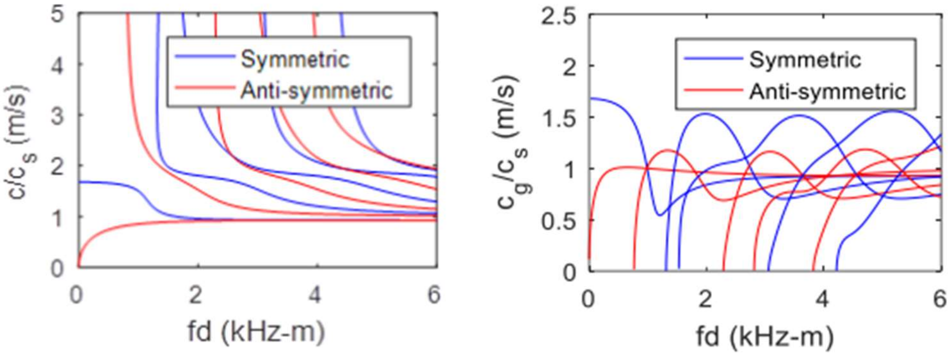

Figure 7. Example of phase and group velocity dispersion curves respectively [38]

3.4.2.2. Attenuation

When GLWs propagate, wave energy is what travels through the medium. The energy tends to dissipate as they advance along it. This phenomenon is known as attenuation. The dissipation occurs in the amplitude of the emitted signal, and this becomes more evident when they encounter a damage or non-homogeneity on the material. Attenuation behaves differently depending on the wave mode. The attenuation of anti-symmetric modes is considerably higher than symmetric modes due to the out of plane displacement, which lets the energy dissipate on the outer environment instead of just keeping it inside the medium [39]. Su and Ye (2009) observed, by measuring from two points in a plate, that the amplitude of GLWs decreases proportionally to the inverse of the square root of the propagation distance [30]. The previous statement describes Eq. (13) [30] and with-it the attenuation of GLWs can be compensated by multiplying the measured signal amplitude by the square root of the elapsed time, as seen below. Where $A(d_1)$ and $A(d_2)$ are the GLWs amplitudes at d_1 and d_2 respecting the emitter source location. Attenuation graphs of GLWs in the material are shown on Figure 8 [40].

$$\frac{A(d_1)}{A(d_2)} = \frac{\sqrt{d_2}}{\sqrt{d_1}} \tag{13}$$

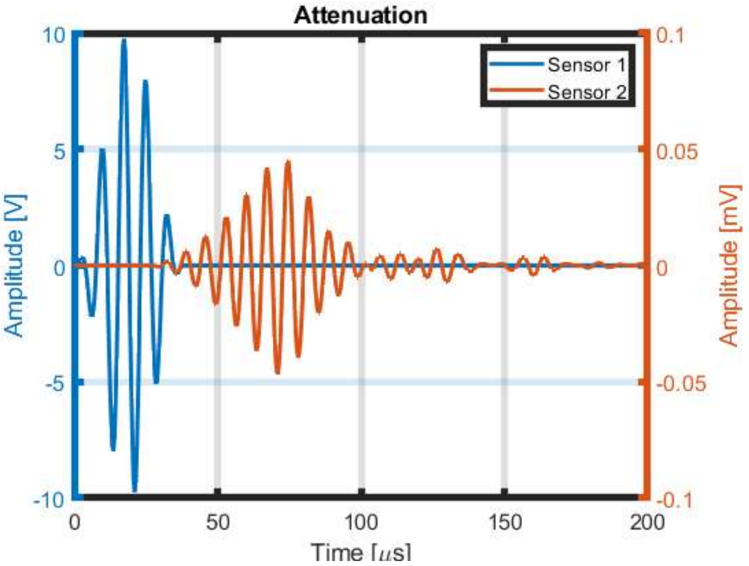

Figure 8. Attenuation of GLWs on AA5083 plate

The use of GLWs has been thoroughly studied by many researchers in the past decade due to their ability to propagate long distances in plates and shells structures while having a very low attenuation [41]. Quaegebeur et al. (2011) proposed a model using GLWs to identify induced disbond defects on dissimilar bonded joints made of carbon fiber reinforced polymer and titanium plate [42]. He et al. (2013) developed an experimental damage detection and quantification method employing GLWs on riveted lap joints with PZT sensors embedded [43]. Baid et al. (2015) used GLWs on an aluminum plate, a woven composite laminate and an aluminum honeycomb sandwich panel to successfully determine the dispersion curves using a pitch-catch ultrasound setup [44]. Mori and Biwa (2016) experimentally investigated the interaction of GLWs on several bonded butt joints made from aluminum using different joint properties [45]. Wang et al. (2018) developed a fatigue life prediction model using GLWs on an aluminum riveted lap joint taking into account a known crack size [46]. Philibert et al. (2018) and Dafydd and Sharif Khodaei (2020) studied the use of GLWs to detect induced barely visible impacts on carbon fibre reinforced structures [47], [48]. Wojtczak and Rucka (2019) studied the consequences of the frequency of GLWs for damage identification on steel single lap bonded joints [49].

Although, there is wide range of literature regarding the use of GLWs for damage detection on plate-like structures, the employment of GLWs on structural bonded joints has substantially fewer studies.

3.5. Time-reversal method

TRM was proposed by Fink (1992) and developed as a solution for inhomogeneous media problems [50]. After the studies presented by Fink et al. (1999), different fields started to use body waves (P- or S-waves) successfully [51], [52]. Their usage range are from ultrasonic brain surgery [53], active sonar and underwater communications [54] to Non-Destructive Evaluation (NDE).

Ing and Fink (1998) focused on the use of TRM with GLWs. The study showed that TRM was able to be employed with GLWs and account for the dispersive characteristic of the waves [55]. TRM is a process where a recorded signal is reversed in time and transmitted back from the receiver to the transmitter location. Figure 9 shows a TRM on a plate-like structure, where (a) is the input signal applied to a piezoelectric transducer at X, (b) is the response signal captured at Y, (c) represents the re-transmitted signal after time reversed from Y to X. Finally, (d) is the comparison of the original emitted signal and the reconstructed signal at X. Theoretically, in the case of no structural damage along the path between the actuator-sensor, the received signal at the original transmitter location will be identical as the input signal.

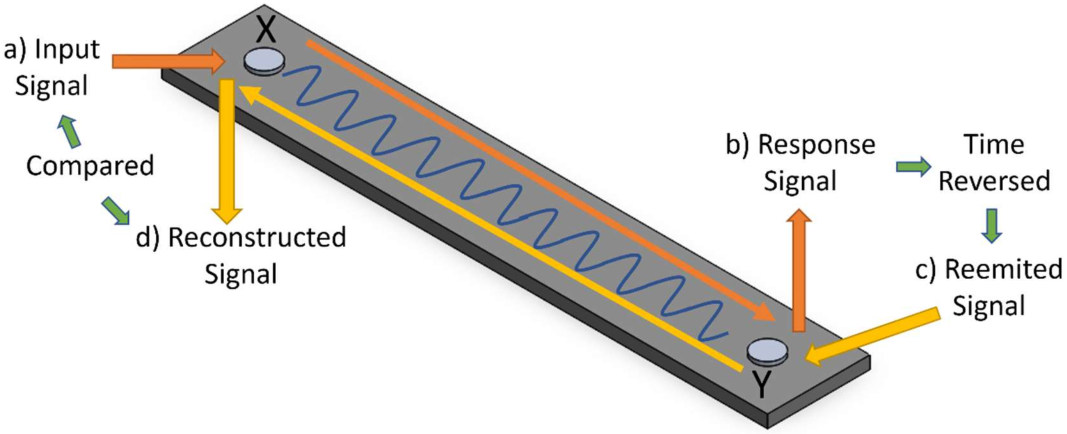

Figure 9. Time Reversal Method

As an active SHM system, several active techniques to excite Lamb waves in plate-like structures have been developed. The used signals can be either Narrow- Band (NwB) or as in nature, a Broad-Band (BdB). They are characterized by a single central frequency peak and multi-frequency peaks, respectively. One of the most common NwB signals used is the Hanning Window, better known as the Hann Window (HW), which was introduced by von Hann in 1903. Operational conditions are subjected to events where BdB signals are emitted into the structure instead of NwB.

The TRM for GLWs have the capability to avoid unwanted background noise while gathering and maintaining the waves' information. According to literature, defects in a structure can be detected by reconstructing an original signal without the necessity of being compared with an initial fingerprint. In other words, the TRM is carried through by taking advantage of the transmission-receiving capabilities of PZT transducers. These baseline-free damage detection techniques used on GLWs tend to account for the effects of the dispersion phenomenon.

3.6. Computational methods

3.6.1. Absorbing layer technique

The use of finite element models to simulate guided wave propagation and scattering has been rapidly increasing due to the impracticality of developing analytical solutions for these problems. One of the reasons why the implementation of finite element models has been a success is the low computational cost and the available ultrasonic finite element models that allow the users to confidently employ them. A fundamental drawback on the computational models is the presence of unwanted reflections from the model edges which will disturb the reception of the waves. A simple solution that is not so viable is to increase considerably the area of interest of the model in order to isolate those unwanted reflections [56]. This method not only increase the computational cost but also reduce the computational efficiency.

Innovative methods, such as absorbing layer techniques, have been developed in order to avoid unwanted edge reflections [57]–[60]. The absorbing layer techniques introduce a finite number of layers from specific size to the spatial domain of the model. These same sized layers are made of the same characteristic element size but with different properties which will allow to take in the incident waves. This is being implemented since a reduction in the stiffness and an increase on damping properties of the material will result in an absorption of the incident waves. Different absorbing layer techniques have been successfully executed on computational models [61]–[63].

Pettit et al. developed a performance optimization of a conventional absorbing layer technique, named the stiffness reduction method (SRM), in order to provide a better result due to reflective boundaries within a significant reduced spatial domain [56].

The SRM, as an absorbing layer technique, has as a principle to add material layers into the model, which will result in a decay of the incident waves. This means that the reflections will be absorbed by each layer added. The mentioned SRM sections are being altered between layers on the damping and stiffness properties of the original system where each layer has calculated variables that are functions of known constants of the original material. Falcetelli (2018) made a numerical comparison on the use of the SRM against other computational absorbing layer techniques and non-reflective boundary methods on aluminum plates. He obtained excellent performance results on the SRM model [64].

3.6.2. Damage and failure

Metal structures that are subjected to high loads undergo large plastic deformations. Plastic deformation cause metal particles and impurities to disengage from each other causing the formation of cracks and fracture in the material. Nowadays, special awareness has been made on the prediction of ductile fracture of metal materials [65].

Computational FE commercial software, can predict onset of failure, simulate the progression of damage and the failure of ductile materials. This is intended to mimic real initiation and propagation of damage and the failure of the material. The existing damage models for ductile metals are frequently used on structural engineering applications due to the high accuracy of results. Rice et al. concluded a theoretical correlation between void growth rate and material triaxiality [66]. Trattnig et al. performed different triaxial test applied to austenitic steel and derive an index correlation based on the developed experimental results [67].

To introduce a ductile damage model on ABAQUS CAE^{TM}, three failure mechanism must be considered. i) an undamaged elastic-plastic response of the material, ii) damage initiation criterion, and iii) a damage evolution response, which causes the deletion of the affected elements in the model.

The undamaged elastic-plastic response of the material is the deformation of the materials under mechanical loads which is characterized by an initial elastic deformation. If a critical level of stress or strain (yield stress or strain) is exceeded, a nonlinear behavior follows the elastic phase of the material. This nonlinearity is commonly known as plasticity. Where Figure 10 shows the undamaged elastic-plastic response from the slope (elastic) and going through the behavior after the yield strength until the ultimate strength (plastic). Linear and non-linear material properties such as the Young's modulus, Poisson's ratio, plastic stress and strain have to be introduced to the material model in ABAQUS CAE^{TM} to complete the undamaged elastic-plastic response of the material.

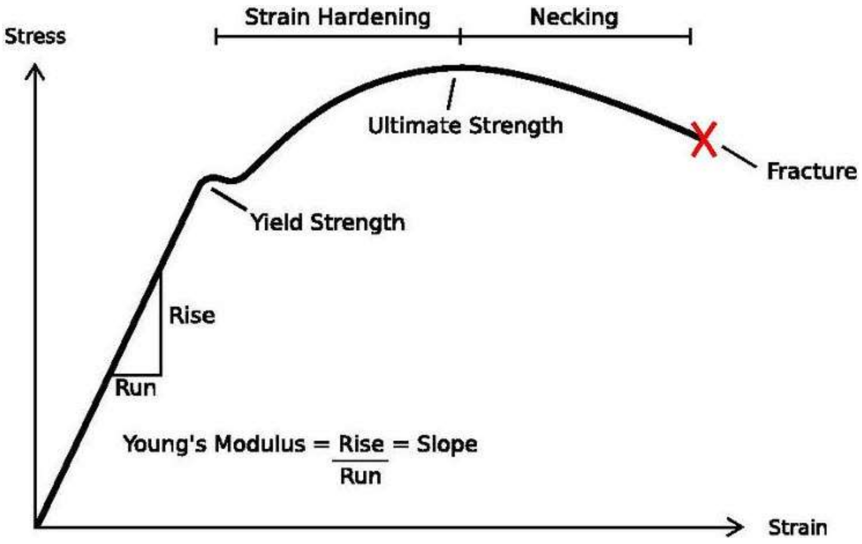

Figure 10. Generic stress-strain curve [68]

In the case of the damage initiation ABAQUS CAE^{TM} offer different criterions for metals with distinct types of material failure for example, damage initiation for fracture of metals (ductile and shear criteria) and for necking instability of sheet metal. The damage initiation for ductile metals is intended to simulate the initiation of damage caused by nucleation, growth, and aggregation of voids. This criterion assumes that equivalent plastic strain at the initiation of the damage, $\varepsilon^{pl}_{0,}$ is a function of the stress triaxiality and the strain rate.

For a damage evolution response, this criterion theorize that damage is subjected to a gradual degradation of material hardness which leads to a failure of the material. In this case, Figure 11 shows a stress-strain curve with a progressive damage degradation to implement the damage evolution response. Where, σ_{y0} and $\overline{\varepsilon}^{pl}{}_{0}$ are the UTS and equivalent plastic strain at the initiation of damage with an overall damage index (DI) equal to 0. Respectively, $\overline{\varepsilon}^{pl}{}_{f}$ is the equivalent plastic strain at failure with a damage index equal to 1.

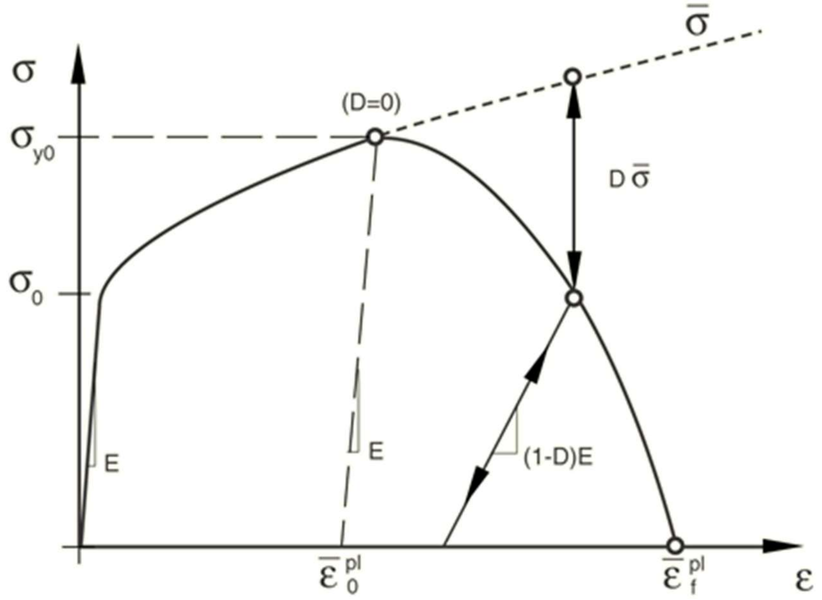

Figure 11. Stress-strain curve with progressive damage degradation [69]

This can be introduced by identifying the slope of the material to find the fracture strain or equivalent plastic strain value and consequently, the damage indexes by using Eq. (14) [69]. Where DI, σ, and $\overline{\sigma}$ are the damage index, the stress at each damage index and the stress reference, which is selected to be where DI = 0 or the UTS.

$$\sigma = (1 - DI)\overline{\sigma} \qquad (14)$$

Once the three specific criterions are met, the material’s stiffness degrades according to the specific damage evolution rule of the criteria. Without the damage evolution rule, the material hardness will not decrease.

3.7. Signal processing

3.7.1. Convolution

The convolution is a mathematical concept with use in many applications, such as acoustics, signal and image processing, engineering, physics, computer vision and even statistics. In signal and image processing, the convolution function is one of the most important concepts but is commonly confused with the mathematical concept of addition. In simple terms, in signal processing field, the convolution takes two signals and construct a third one, while the addition only takes two numbers to generates a third one. In other words, with the use of the convolution function, the output of a system can be constructed by knowing the input signal and the impulse response of the system, as shown in Figure 12.

Convolution function is stated in Eq. (15), where *h* is the output, *f* the input and *g* the response of the system. The *t* value does not actually represent the time domain. In this case, the convolution function is described as the area under the function *f(t)* weighted by a function *g(-τ)* shifted by a value of *t*. This means that as *t* value changes, the weighted function increase the sections of the input signal.

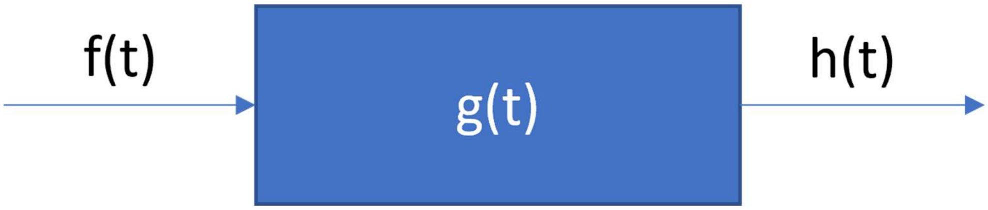

Figure 12. Convolution function

$$h(t) = (f * g)(t) = \int_{-\infty}^{\infty} f(\tau)g(t-\tau)d \qquad (15)$$

A system’s output can be calculated for any input signal that is studied, if a system's impulse response is known.

3.7.2. Correlation

Correlation is another important mathematical function in the signal processing field. The correlation function is commonly confused with the previously explained signal convolution function. The correlation function contains a different physical definition, it can be either done with itself (autocorrelation) or between two dissimilar signals (cross-correlation). Characteristic applications of the correlation are in the signal processing and statistics fields. Signal processing explores areas such as satellite, radar, wireless communications systems and sonar [70].

In the case of the signal autocorrelation, the function is used to measure the power of the signal by distributing it along the signal. An example of this function is the signal correlators equipment, which measure the signal power, uses signal correlation. The cross-correlation function can be used in applications to graphically identify if an analyzed data contains hidden signals. This means that if a signal is being disturbed by undesirable noise, an estimation of the noise can be performed on the signal. Moreover, it can also be considered as a measure of resemblance between two signals as function of the displacement of one relative to the other. Eq. (16) presents the mathematical equation for the cross-correlation function.

$$(f \otimes g)(\tau) = \int_{-\infty}^{\infty} \overline{f(t)} g(t+\tau)dt \tag{16}$$

This concept can also be used as a statistical parameter, where an R value quantify the correlation of two random signals or sequences. This concept is used as an advanced analysis technique This technique is based on Eq.(17) , where two stationary random sequences, X_n and Y_n, are evaluated.

$$R_{xy}(m) = E\left\{X_{n+m} Y_n^*\right\} \tag{17}$$

Where n, Y_n*, and E are values from minus infinite to infinite, complex conjugation and expected value operator [71].

4. State of the art

Over the last ten years, the aerospace industry has introduced stronger and lighter materials to their structures. The introduction of these materials added to the use of bonded technology has directly impacted on cost savings due to the reduction of weight. Although many advantages have been proven using adhesive joints, an on-time monitoring of the joints is required in order to assess its life cycle and to reduce the probability of structural failures by an early intervention on the maintenance of the structure.

In 2018 Rucka et al. conducted an experimental investigation using GLWs to identify damage on nine metal-to-metal SLJS with different debonding-like defects. Their experimental configuration was based on a signal emitted by a piezoelectric PZT transducer and measure the wave with a laser vibrometer. The results presented by Rucka et al. showed that the use of a weighted root mean square values for damage imaging could successfully identify the presence of defects in the adhesive, as well as interpret the geometry of the defect.

The use of TRM has been successfully studied on NwB applications for plate-like structures [52], [72]–[75]. Jayakody et al. (2018) used a modified TRM process and a transverse velocity as a measurement quantity in bonded joints. In their study, the experimental and computational results showed that the obtained TRM signal is like the emitted signal in both time and frequency domains for a disbond scenario on the bond line. The disbonds diameter on the joint were varied from 10 to 25 mm using a 150 kHz [76]. Du et al. [77] used a virtual time reversal (VTR) to monitor experimentally the preload of bolted L-shaped lap joints using as a reference a reemitted signal from a fully tightened condition. The results presented showed an improvement in the detection sensitivity of bolt loosening compared to a TRM. Wang and Shen (2019) used a modified GLWs VTR algorithm with the use of a compensation transfer function to eliminate the transducer influence for dispersive HW signal in a thin plate-like structure [78]. The analytical solution presented on their work shows a perfect reconstruction of the emitted signal for both GLWs modes. This was validated by a finite element model and experimental works in order to verify the proposed virtual time reversal algorithm [78]. Xu et al. [79] extracted the phase shift and the signal amplitude of the wave packet as indices using modified TRM for bolt loosening on lap joints. The modification of the TRM consist of the use of the same reemitted signal for all the studied cases.

Xu et al. performed experimental and numerical methods to quantitative validate the bolt preload on the lap joints. Their modified TRM presented better accuracy results than a standard TRM. Gauthier et al. (2020) [80] studied debonding on metal-to-metal bonded joints using GLWs. Their results evaluate and qualify the adhesion in the joint by using Lamb dispersion modes associated to the Jones rheological model. The results were achieved with a frequency cut-off which is used as an indicator of debonding of the joint [80]. Falcetelli et al. (2021) [81] applied a Frequencies Compensation Transfer Function (FCTF) with virtual TRM for a successful reconstruction of known BdB signals at their origin site and characterization of the unknown BdB signals, such as the Pencil-Lead Break signals. Kannusamy et al. (2022) [82] proposed a virtual refined time-reversal method for damage detection on an aluminum plate using broadband Gaussian excitation and sensed with surface-bonded piezoelectric PZT transducers. Their results showed the accuracy of the VRTRM for signal reconstruction and localizing block mass damage on the aluminum plate [82]. Pineda Allen and Tai Ng [83] studied the debonding on adhesive joints by using the non-linearity of Lamb waves. The presented method is because the appearance of combined harmonics is an indication of material nonlinearity which is caused by defects on the joint. FE models and experimental set-ups were used to validate the effectiveness of the debonding indication using a combined frequency wave. The results only provided insights of the intended use of nonlinear Lamb waves for detecting debonding on joints.

Up to date, regardless of the potential characteristics to detect damage using an AU-based SHM system, there is no record of a complete system/methodology that could solve the SHM intended questions. The previous literature review shows the successfully application of the use of GLWs to identify defects such as debonding and the use of TRM mostly on thin plate-like structures or bolted joints.

The state-of-the-art performed in this section, signals the lack of research in the application of the Time Reversal Method for damage detection related to the initiation of crack and the development of the crack on single lap shear bonded joints. By investigating this scenario, the thesis contributes to reduce the research gap on the possibility of using time reversibility of Lamb waves to monitor the integrity and determine when an adhesive in a single lap shear bonded joint starts failing.

5. Methodology

In this chapter, the reader will be able to find a detailed description of the methodology used for the implementation of the AU-based structural health monitoring system on a metal-to-metal single lap shear bonded joint. The methodology, as shown in Figure 13, chapter describes the propagation medium, the development and validation of the computational models, required for the wave propagation and as for the introduction and development of damage on the adhesive. At the end, the application of the TRM on after obtaining a wave propagation convergence on a pristine and damaged condition of the SLSJ.

All the work presented in this chapter has been carried out at the HolSIP Laboratory at Clarkson University and it is part of an ongoing research project of special interest to the Office of Naval Research (ONR), which is an organization within the United States Department of the Navy.

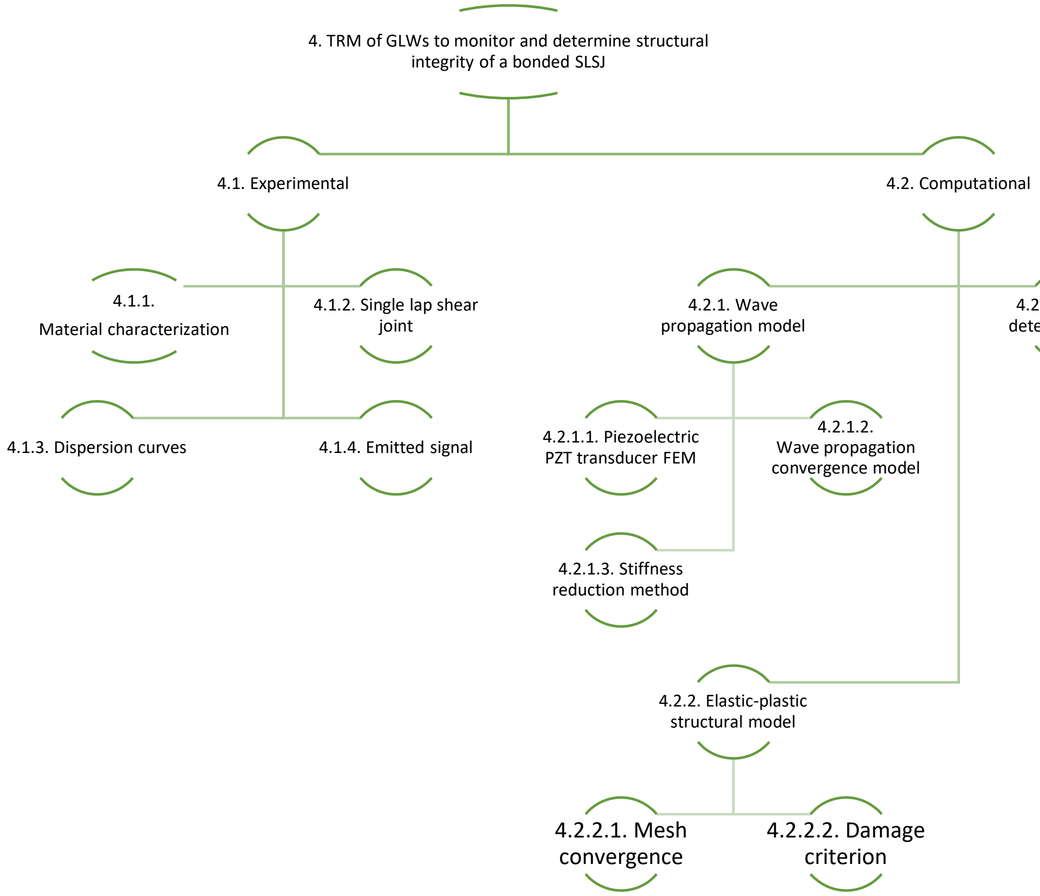

Figure 13. Methodology approach

5.1. Experimental

5.1.1. Material characterization

The object of study is a metal-to-metal single lap shear bonded joint. The selected materials for the SLSJ were an AA5083 and the adhesive ADV176/276 from Pro-Set® [1]. Both materials properties, such as ultimate tensile stress, yield stress, elongation, Young's modulus, shear modulus and Poisson's ratio, were obtained experimentally by a material characterization study based on the standard from ASTM E8 [84] and ASTM D638 [85] for the AA5083 and adhesive ADV176/276 from Pro-Set®, respectively. Figure 14a shows the electromechanical universal TestResources® frame rated for 50,000 Newton force capacity that was used for the material characterization studies and the Newton controller TestResources® on Figure 14b.

Figure 14. TestResources® equipment

An Epsilon axial extensometer 3542 with a 2" gauge length shown on Figure 15a was used. A temperature and voltage DAQ system (Compact DAQ) showed on Figure 15b used for data acquisition of the images taken by two FLIR Grasshoper® 3 cameras 2.3 MP 163 FPS.

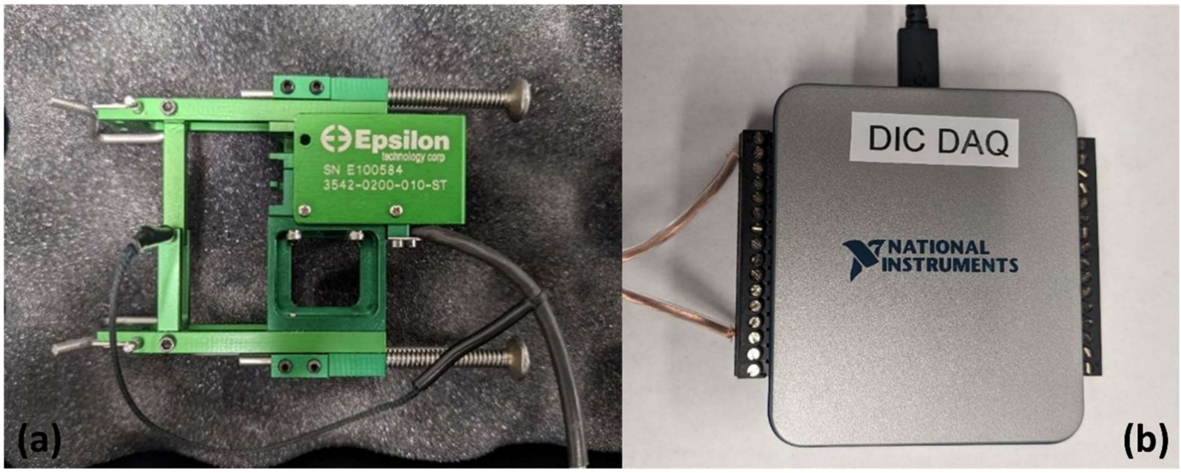

Figure 15. Measurement equipment

FLIR Grasshoper® 3 cameras (Figure 16a) with a Fujinon CF25HA-1 lens adapted (Figure 16b) were used in order to do Digital Image Correlation (DIC) to make quantitative measurements of stress, strain and displacement on the studied specimens. The VIC-9 software was used for the post-processing of the images taken by the FLIR Grasshoper® 3 cameras [86], [87].

Figure 16. High speed cameras

Figure 17 shows the experimental set-up of the extensometer attached to the specimen and mounted on the electromechanical universal TestResources® test frame. The FLIR Grasshoper® 3 cameras with the Fujinon lens are also present on the set-up.

Figure 17. Experimental set-up for material characterization

5.1.2. Single lap shear joint

The manufacture of the SLSJ was following the ASTM standard D1002-10 (2019) [88]. The standard provided the dimensions and manufacture recommendations to follow. Figure 18 shown the SLSJ computational model. Both the lower and upper AA5083 coupon were 161.1 mm long while, the adhesive bond line was set to 72.2 mm. These values give an overall length of 250 mm of the SLSJ.

The dimensions were obtained by using Eq. (18) and (20) where AA_L is the AA5083 coupon length, ADH_{OL} the overlap length of the SLSJ, τ is 50 percent of the estimated average shear strength in adhesive bond, $F_{ty,}$ the yield point of the adherend and t the thickness of aluminum. The estimated average shear strength was taken from the Pro-Set® technical data sheet [1].

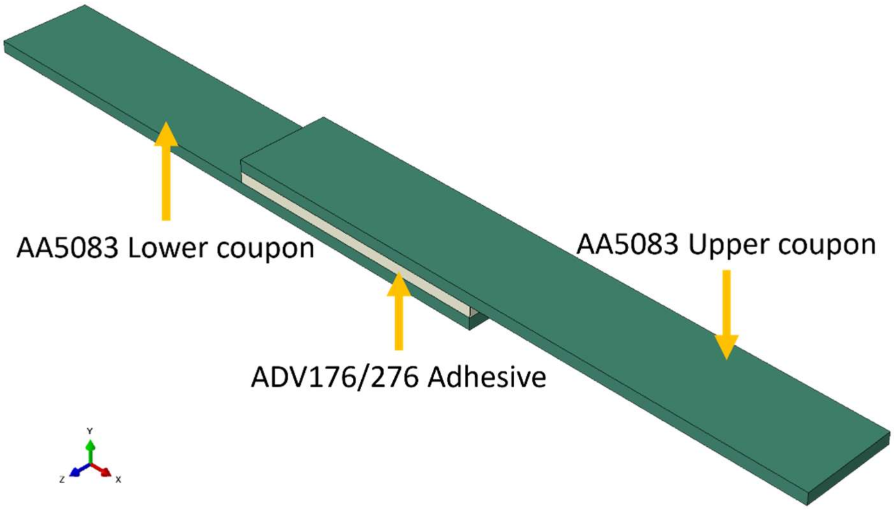

Figure 18. SLSJ according to the ASTM D1002 standard [88]

$$AA_L = 88.9 + ADH_{OL} \tag{18}$$

$$ADH_{OL} = \frac{Ft_y \cdot t}{\tau} \tag{19}$$

5.1.3. Dispersion curves

Both materials are isotropic which gives a homogeneous propagation of GLWs through the joint, avoiding the complexities related to anisotropic behavior. Considering the waves speed and the material properties of the propagation medium, the Rayleigh-Lamb equations, (6) and (7), can be solved to plot the dispersion curves of the materials. These will allow to identify the range of frequencies where the GLWs lower-order modes, A_0 and S_0, are being propagated across the bonded joint.

To obtain the dispersion curves it was necessary to calculate the longitudinal and transverse wave speed of each material. The values for wave speeds of the P-and S-waves, C_L and C_T, for the AA5083 and ADV176/276 are calculated by using Eq. (1) and (2), respectively.

Once the wave speed values were calculated, the dispersion curves were computationally obtained using the Vallen AE-Suite software developed by *Vallen Systeme* GmbH, which is a company that develop Acoustic-Emission (AE) test equipment. Figure 19a shows the chosen module on the Vallen AE-Suite software to solve for the Rayleigh-Lamb equations and obtain the dispersion curves of both materials [89]. Figure 19b the detailed inputs that are need for the calculation of the dispersion curves.

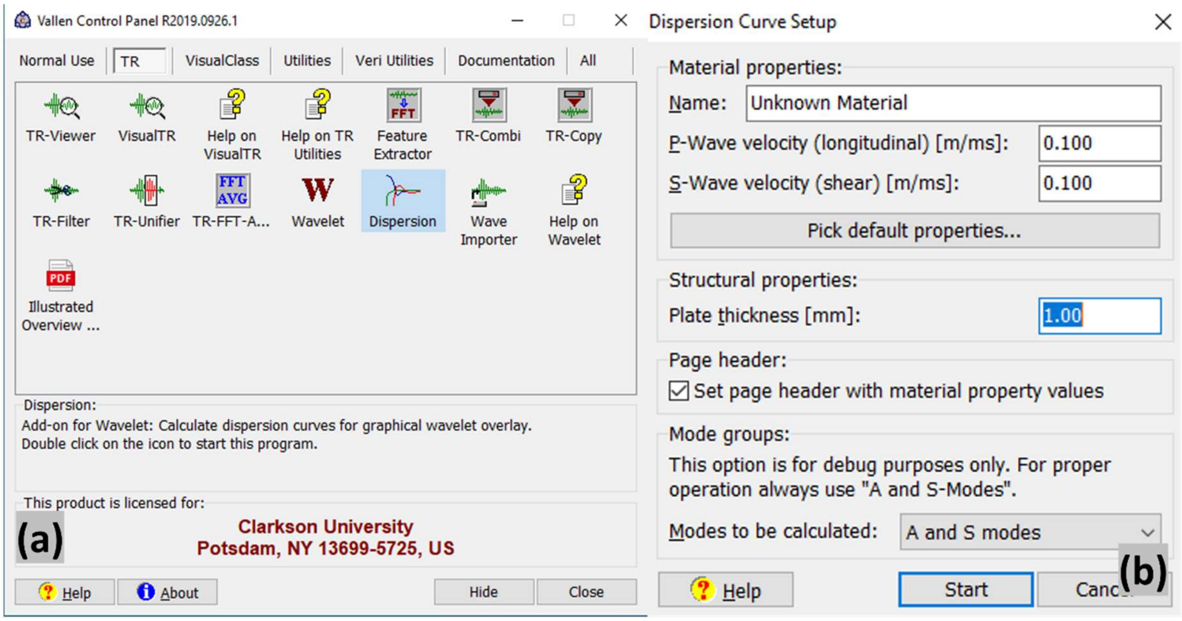

Dispersion:
Add-on for Wavelet: Calculate dispersion curves for graphical wavelet overlay.
Double click on the icon to start this program.

This product is licensed for:
Clarkson University
Potsdam, NY 13699-5725, US

Material properties:
Name: Unknown Material
P-Wave velocity (longitudinal) [m/ms]: 0.100
S-Wave velocity (shear) [m/ms]: 0.100

Structural properties:
Plate thickness [mm]: 1.00

Page header:
☑ Set page header with material property values

Mode groups:
This option is for debug purposes only. For proper operation always use "A and S-Modes".
Modes to be calculated: A and S modes

Figure 19. Vallen AE-Suite software window

5.1.4. Emitted signal

A 5 cycle Hanning window was the selected signal to be emitted by the piezoelectric PZT transducer. In this study, this signal was identified by a single central frequency peak of a 135 kHz on the frequency spectrum after the application of the FFT. *Figure 20*a shows the chosen signal on the time and 17b on the frequency domain. The chosen frequency for the emitted signal was selected due to the results of the dispersion curves that allowed to identify the frequency range below the fundamental Lamb modes.

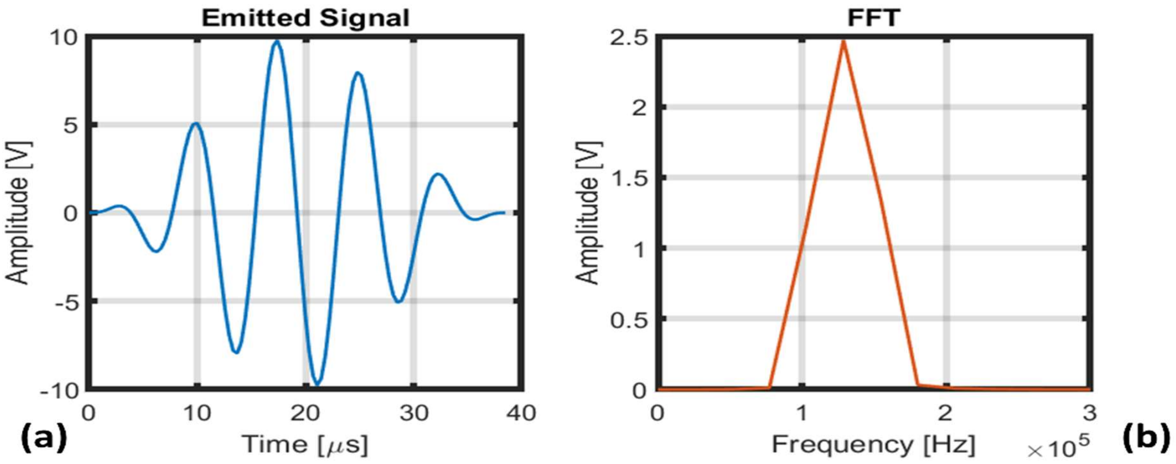

Figure 20. Hanning window

5.2. Computational model

The presented 3D models were developed using different computer-aided design (CAD) software, such as ABAQUS CAE^{TM}, SolidWorks$^{®}$ and PTC Creo$^{®}$. The numerical analysis was performed in a Window 10 workstation with 2 Intel® Xeon® CPU E5-2630 v4 (20 cores and 40 logical) running at 2.20 GHz.

The finite element single lap shear bonded joint model was developed in ABAQUS CAE^{TM}. The AA5083 coupons were bonded to the ADV176/276 adhesive using tie constrains. Figure 18 shows the FE model of the SLSJ developed on ABAQUS CAE^{TM}.

The FE considered in this study were a linear-elastic, and a linear-elastic-plastic model. The first one mentioned was employed for the wave propagation and damage detection models. The second one was used for simulating the tensile test to failure of the SLSJ. This allowed the author to obtain the initiation and evolution of damage on the bondline.

A Dynamic/Implicit solver in ABAQUS CAE^{TM} was chosen to perform the wave propagation numerical simulations because it allowed to model the physical piezoelectric elements. A Dynamic/Explicit solver on ABAQUS CAE^{TM} was chosen for the development of the damage evolution model and the tension test simulation of the SLSJ.

5.2.1. Wave propagation model

5.2.1.1. Piezoelectric transducer finite element model

The SHM field require implementation of small and lightweight sensors on the structures. Piezo ceramics transducers, such as the PZT, satisfy the requirement and can carry out active ultrasonic techniques converting electrical energy directly into mechanical motion and vice versa.

The use of piezoelectric PZT transducers as signal emission technique for GLWs has been employed in this thesis work. Piezo Kinetics, Inc. transducers were chosen for modelling the computational signal emission and reception due to their availability at the HolSIP laboratory. The overall dimensions of the piezoelectric PZT transducer were 0.253" diameter and 0.032" thick. Figure 21a and Figure 21b shows respectively, the physical and the computational model of the chosen piezoelectric PZT transducer. Their range of work frequencies goes from 120 kHz and above.

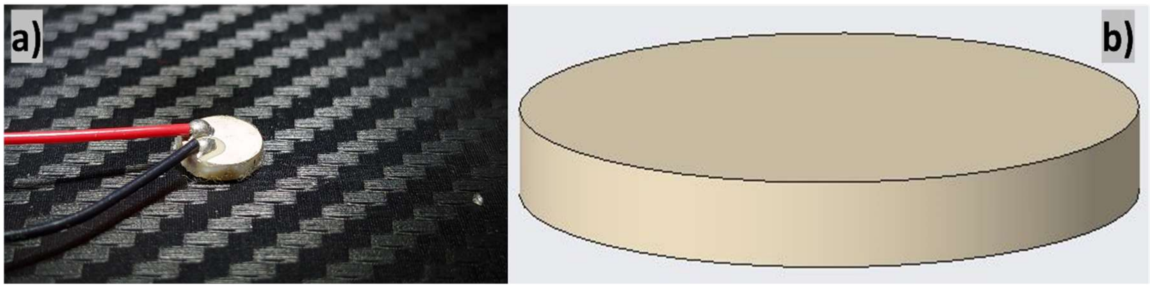

Figure 21. Piezo Kinetics transducers

An analytical model, taken from Piefort [90], was followed to validate the FEM results of the piezoelectric PZT transducer. Figure 22 present the stacked model of transducers. This model was applied as an individual transducer in this study. Eq. (20) is an approximate relationship that calculates the change of length on the piezoelectric transducer caused by an applied voltage. Where Δ is the change of length, d_{33} the piezoelectric constant, ϕ the applied voltage and n the number of stacked piezoelectric discs. This approximation is applied when no external load is present.

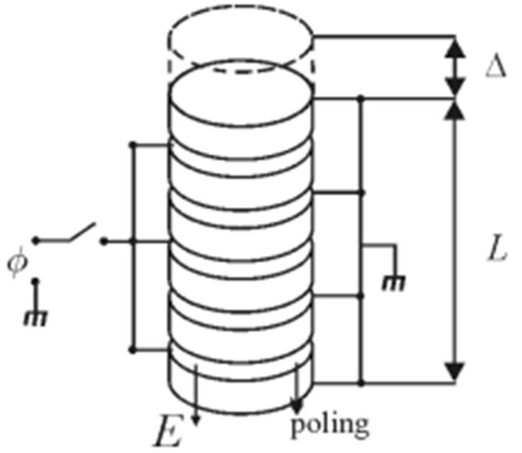

$$\Delta = d_{33}\phi n \qquad (20)$$

Figure 22. Piezoelectric PZT transducer analytical model [90]

The material properties of a piezoelectric PZT-5A were taken from Martinez [91] and used as input for the material model of the transducer on ABAQUS CAE^{TM}. Abaqus/Standard was employed for the solution of the finite element model. The mechanical boundary conditions are represented on Figure 23 as the yellow arrow, which means that the lower surface of the piezoelectric PZT transducer is unable to move in the y-direction but moves freely on the x-and z-axis. Electrical boundary conditions are represented as the green arrows. Vin was set as a voltage of 10V whereas 0V for Vout.

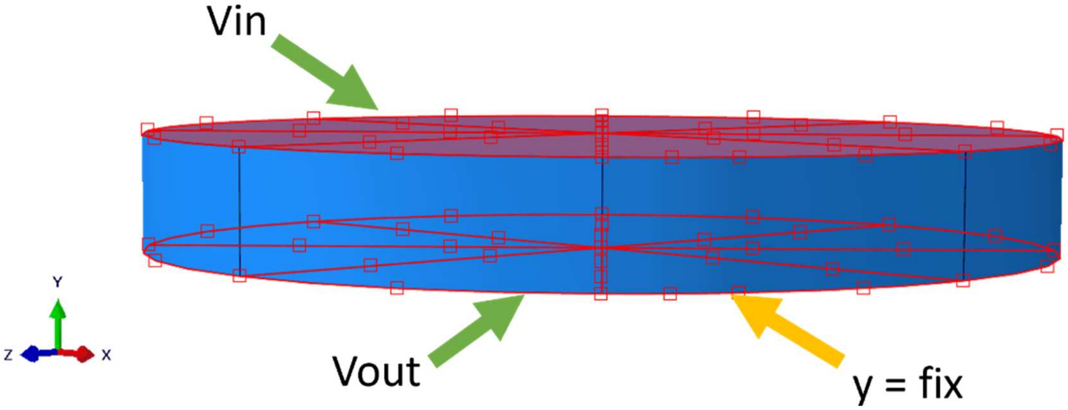

Figure 23. Piezoelectric PZT transducer boundary conditions

5.2.1.2. Wave propagation convergence model

For a proper transmission of the Lamb waves a convergence model is needed. This is mainly a concern about the spatial and temporal resolution in the computational solution.

The first criterion was to define a time step, Δt, for the simulation. This allowed the wave to be properly captured at each time step. The accuracy of the simulation can be increased with a smaller integration time steps, costing a higher computational time. Frequency components would not be correctly solved if a long-time step was chosen. Eq. (21) shows a compromise of 20 points per cycle of the frequency, giving an efficient solution within a reasonable time [92]. Where $f_{\max}$ is the highest frequency in the simulation.

$$\Delta t = \frac{1}{20 f_{\max}} \tag{21}$$

The second criterion for the convergence model of the wave propagation was the characteristic length of the elements placed on the computational model. The mesh element size of the computational model must be set for a spatial efficient wave propagation. To achieve the spatial convergence, the characteristic length of the elements was defined by Eq. (22), where l_e is the characteristic element length, $\lambda_{\min}$ the smallest wavelength presents on the simulation and n is the number of nodes. Moser [92] recommended to use 10 to 20 nodes per wavelength. In this study, a value of 10 nodes per wavelength is being consider.

$$l_e = \frac{\lambda_{\min}}{n} \tag{22}$$

5.2.1.3. Stiffness reduction method

Wave reflections from the edges must be considered on the finite element method. These reflections interfere with the emitted signal which results on a compromised received signal. Therefore, it complicates the analysis of the received results on the second piezoelectric PZT transducer. The simplest technique to avoid boundary reflections is to have a considerable increase in the geometry to set a longer time of wave reflection or to avoid them if it is largely increased. Furthermore, if an expansion of the area of interest is implemented, the number of elements will inevitable increase which results on a rise of computational time. The use of an absorbing layer method technique, called the stiffness reduction method (SRM) was implemented in this work to avoid the reflections created by the boundaries.

For the development of the SRM, the first step was to create controlled expansion of the area of interest. This expansion or SRM thickness was defined as $1.5\lambda_{inc}$, where λ_{inc} is the incident wave in the system and divided into the element mesh size, calculated on Eq. (22). Where C_M is defined as the mass proportional damping and variates according to Eq. (23) [56]. The next step was to assign $C_{M\max}$, which is equal to the angular frequency, w, of the incident wave and where x is the corresponding layer (from 0 on the first layer to the $C_{M\max}$ value positioned on the last layer of the SRM thickness, $x = n$). P is a polynomial order for B(0) = 0 and B(n) = 1. For this study, a value of 3 for p was suggested [56].

$$C_M(x) = C_{M\max} B(x)^p \tag{23}$$

For this study, a value of 57 was obtained as the number of layers within the SRM thickness. In the case of Lamb waves, the generation of the S_0 and A_0 gives a different wavelength on the system. A conservative approach was considered by using the larger wavelength calculated.

C_M value grows exponentially from layer 0 to 57 as shown in Figure 24 to absorb more energy at the boundaries. MATLAB® codes were developed to calculate the mass proportional damping.

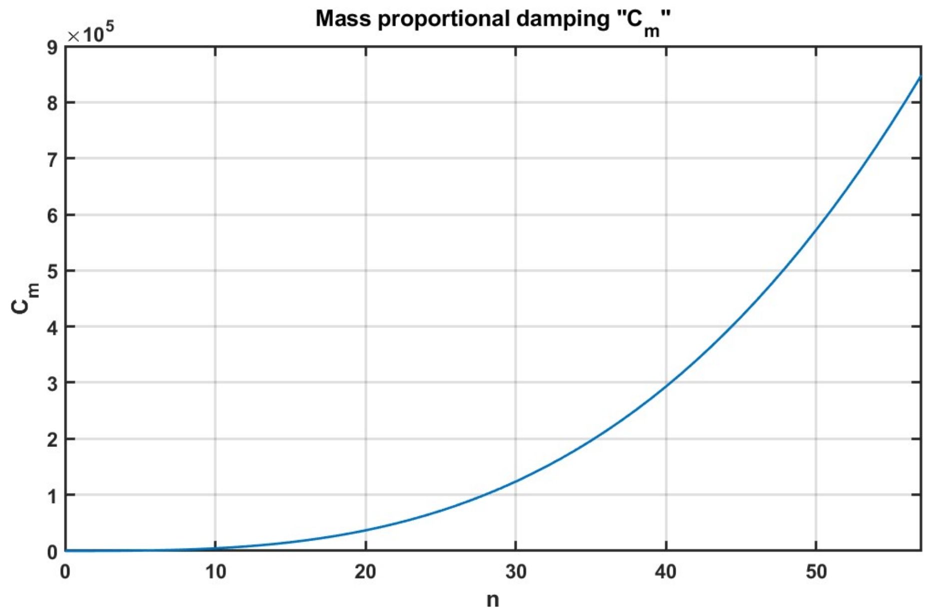

Figure 24. SRM mass proportional damping

The variation of the second value needed for the development of the SRM, which is the Young's Modulus, was calculated as expressed in Eq. (24) [56]. Where E is the calculated Young's Modulus, E_0 is the original value of the material Young's Modulus, k_{inc} the incident wave number and α the attenuation factor to avoid impedance mismatches between adjacent layers.

$$E(x) = E_0 e^{-\alpha(x) K_{inc} x} \qquad (24)$$

The attenuation factor, α, was calculated by Eq. (25) [56]. The maximum attenuation factor, α_{max}, was defined by a ratio of $E/E_0 = 0.01$. Thus, at the last layer of the SRM thickness the value of the Young's Modulus will be 1% of the original E.

$$\alpha(x) = \alpha_{\max} X(x)^p \qquad (25)$$

Young's Modulus values for both materials on each layer, AA5083 and ADV176/276, are shown in Figure 25.

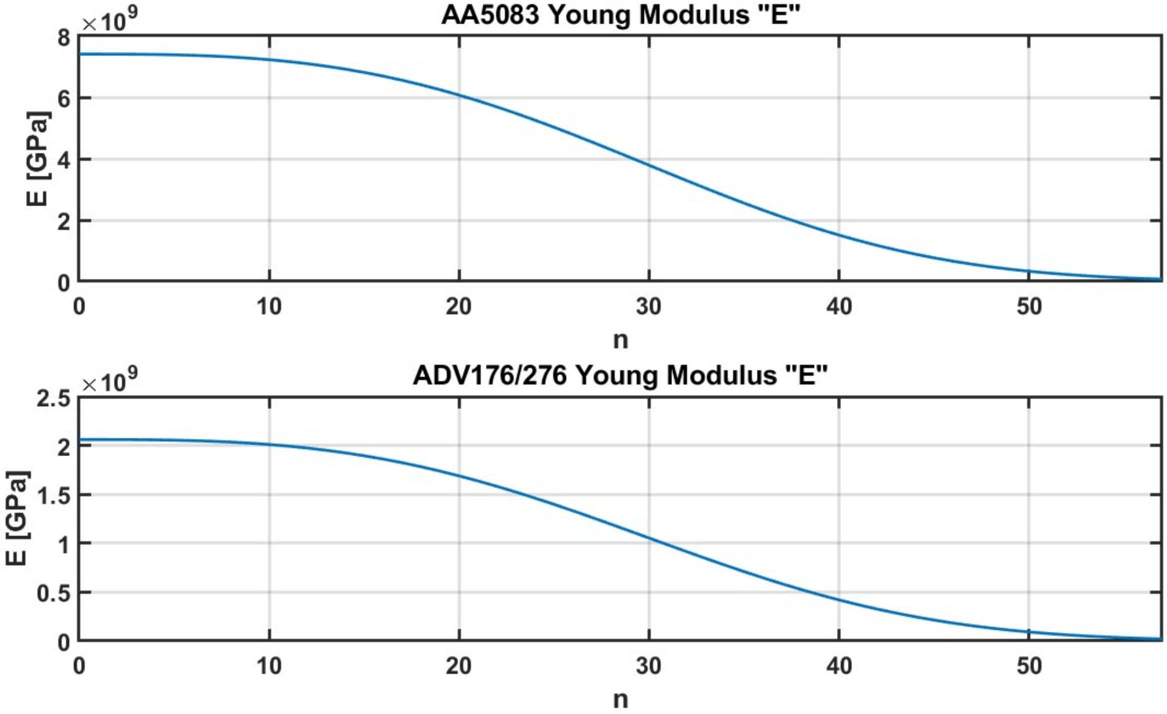

Figure 25. SRM Young's Modulus

As shown in Figure 26, the considerations to ensure a good propagation of the wave were then applied to generate the SLSJ model.

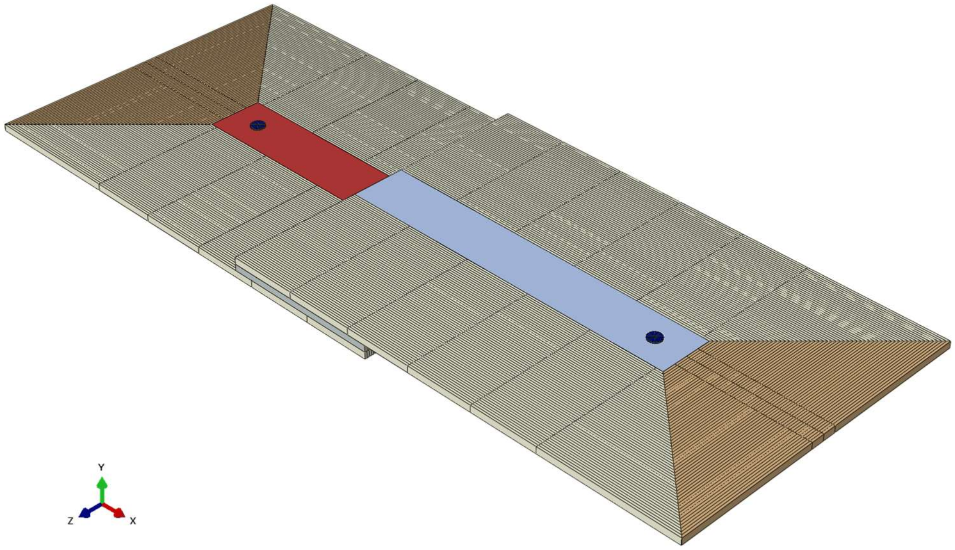

Figure 26. SLSJ model for damage detection

5.2.2. Elastic-plastic structural model

5.2.2.1. Mesh convergence study

Same as the wave propagation model, the elastic-plastic structural model on the SLSJ must achieve a spatial convergence which will determine the ordered discretization error in the simulation. To achieve this spatial convergence, a mesh convergence study was implemented. This refers to the smallest element required in a model to ensure that the results of an analysis are not affected by the element size.

The methodology to establish a mesh convergence was with the use of a stress-strain curve. This curve presented the initiation of damage on the adhesive with respect to the element size. The stress-strain curve was taken from a path line along the middle of the adhesive. Figure 27 shows a red-dotted line in the center of the adhesive. The implementation of this path line made possible to retrieve the stress-strain curve of the adhesive when a tension load was applied.

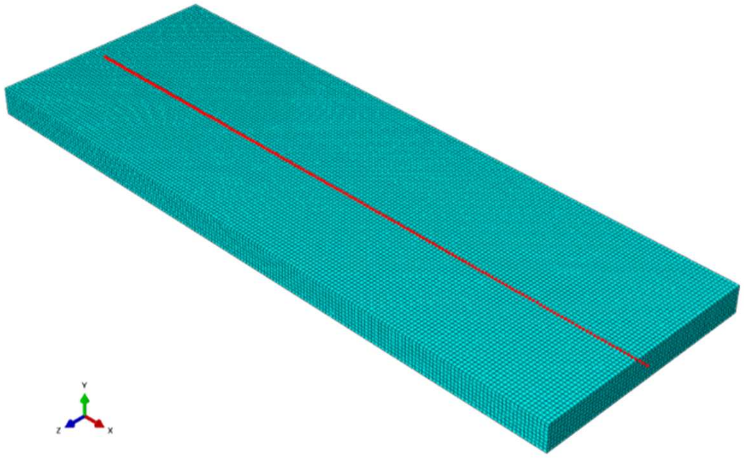

Figure 27. Path line in the middle of the adhesive (400 µm mesh size)

To reduce computational costs on the study, a spatial convergence method called the Richardson extrapolation was implemented.

The Richardson extrapolation is a numerical analysis technique where an estimation of error in the solution is being calculated. The Richardson extrapolation requires at least three different element mesh size models for a mesh convergence study. The estimation of error provides a statistical result for a case value where the element mesh size would go down to zero from a series of lower-order discrete values [93].

Usually, the Richardson extrapolation has been employed using a mesh refinement ratio of r = 2. In this study, use of the Richardson extrapolation provided the estimation of error on stresses values for 800, 400 and 200 µm mesh sizes. This information was used to select an adequate mesh size for the SLSJ FE model considering the computational time needed for each simulation and which percentage of error from a full convergence was obtained.

5.2.2.2. Damage criterion

A damage evolution model was necessary for the finite element model to simulate the initiation and evolution of damage on the adhesive when it is subjected to a shear load. In this study, a dynamic failure behavior on the adhesive ADV176/276 was performed. The numerical simulation of the dynamic failure was complete on ABAQUS CAE^{TM} using a Dynamic/Explicit solver.

For the solver to replicate the initiation and evolution of damage in the bondline, it was needed to introduce a ductile damage criterion for both materials models. The ductile damage suits the AA5083 perfectly because it is a metal, but in the case of the ADV176/276, which is a polymer, the concept of it does not match. Due to date, ABAQUS CAE^{TM} does not count with an available damage criterion for polymers. Therefore, the damaged behavior of the ADV176/276 had to be introduced as a ductile damage for this study. The parameters of the damage evolution models were calibrated by using a reverse engineering approach where the experimental results from the material characterization were used as parameters for the finite element model. This approach was selected to achieve a material behavior on the computational model similar as in the material behavior from the performed experimental tensile tests in the material characterization section.

An element size model, as shown in Figure 28, was executed to ensure that the material model introduced into ABAQUS CAE^{TM} was correctly implemented. The introduction of this element size model intends to successfully validate the material model without accounting for structural effects. The dimensions of the single element are 1 mm x 1 mm x 1 mm. Mechanical boundary conditions were applied on the bottom and side faces of the single element as shown in Figure 28, allowing the single element to elongate in y-axis and restrict the movement as if it was fixed on the bottom and to one side of the element. A velocity of 3.3 x 10^{-5} m/s was defined as a boundary condition on the top of the single element.

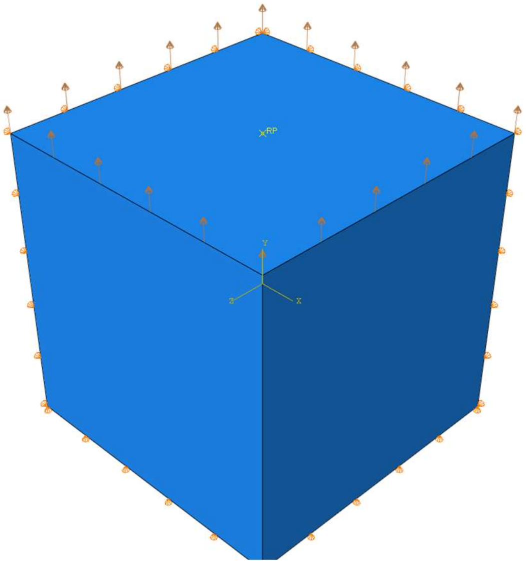

Figure 28. Element size model

In this case, the single element was elongated by the tension force applied. This elongation would cause a reduction of the cross-sectional area of the element leading to a material failure. The required inputs for the ductile damage on ABAQUS CAE^{TM} are the fracture strain, stress triaxiality, a strain rate and the damage evolution criterion, which consist of stress values at different damage indexes (DI).

Taking Figure 11 as reference, the fracture strain value or equivalent plastic strain was obtained by the modulus of elasticity slope when intersected with the ultimate tensile stress (UTS) or yield stress at the initiation of damage. In the case of the stress triaxiality, a value of -0.33 was considered. This value was obtained by the pressure component of the stress tensor and the von Mises equivalent stress of the material. A value of 0 was used for the strain rate. MATLAB scripts were developed to obtain the true stress-strain curve for the materials. Also, the fracture strain value and the damage evolution criteria values (DI and stress values at DI) according to Eq. (14) were obtained using MATLAB scripts.

Once the ductile damage criterion was validated for the use on the material model, it was introduced to the SLSJ. Figure 29 shows a computational replica of the experimental SLSJ for the elastic-plastic structural model. A “Load Tab” and “Extensometer Tab” were added into the model shown in Figure 29 following the ASTM D1002 standard [88]. The extensometer tab was employed to fit the extensometer shown in Figure 15a. The material model used on the Load and Extensometer Tab was an elastic-model of AA5083. Mechanical boundary conditions were implemented as shown in the ends of Figure 29. The green surface is where the SLSJ has a fixed boundary condition, the red surface has a boundary condition restricting the movement on the y- and z-axis. Moreover, a velocity of 1.3 mm/min is applied on the red surface to simulate the applied displacement done by the universal test machine.

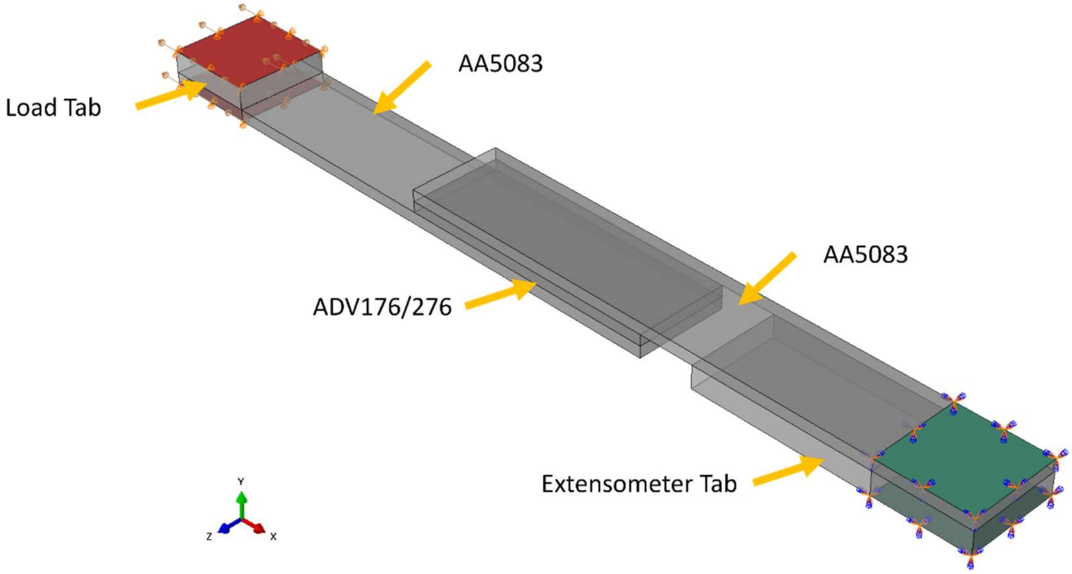

Figure 29. SLSJ damage evolution model

5.2.3. Damage detection model

This section contains the explanation of the TRM applied to different SLSJ models to monitor and detect when the structural integrity of the SLSJ bondline it is starting to being compromised.

Figure 30 shows the TRM, which is the proposed methodology for the damage detection process and eventually solve the scientific question. Where (a) is the input signal applied to a piezoelectric transducer at X, which in this case it is the 5 cycle HW of 135 kHz, (b) is the response of the HW captured at Y, (c) represents the re-transmitted HW after time reversed from Y to X and (d) is the reconstructed HW at X. As part of the post-processing, the input signal and the reconstructed signal at the transducer X were subjected to a convolution process. The result of the convolution process was a maximum value of energy that allowed to identify the section in time where the received signal at the transducer X was most like the initial emitted signal. A visual cross-correlation and an R-value were obtained for the comparison of the two signals. This allowed to quantify the similarity of them. A high R-value was interpreted as no damage on the adhesive, while a damage present on the bondline was identified with a lower R-value.

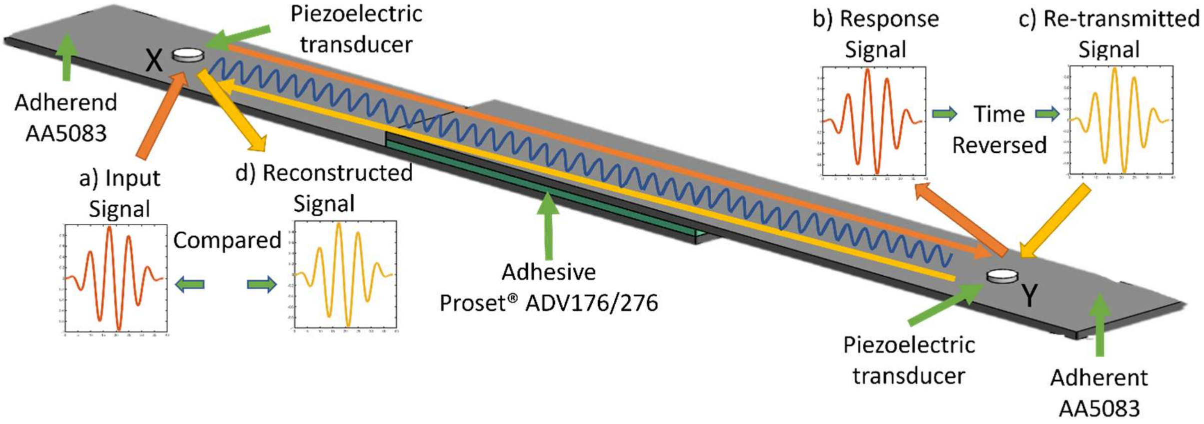

Figure 30. Time Reversal Method on SLSJ model

First, the damage detection model was applied to a healthy SLSJ to assess the structural integrity. Second, a damage on the adhesive ADV176/276 was manually introduced in the SLSJ model. The dimensions of the introduced damaged on the adhesive of the SLSJ are shown in Figure 31. A simple circle on the geometry is commonly used to represent damages on structures.

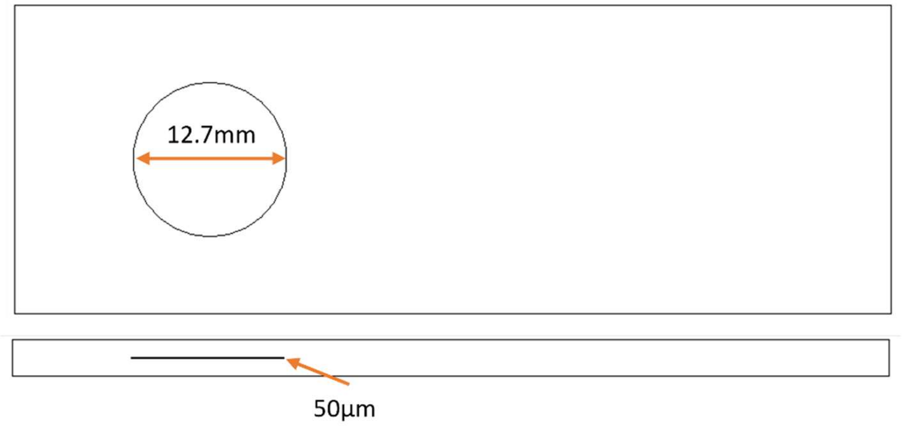

Figure 31. Dimension of introduced damage

Next, the elastic-plastic-structural model with the damage evolution was introduced. Specific moments in time, such as before and after the initiation of damage and before failure, were retrieved from the simulation of the tension test on the SLSJ. This means that the geometry of the SLSJ on those specific moments in time were taken and used as input on the damage detection model. The use of the TRM was implemented for monitoring the structural integrity of the SLSJ.

6. Results

This section summarizes the results obtained from the methodology described on Section 5. The section is divided into the following:

- Experimental
- Computational model

Experimental section includes the results of the material characterization, single lap shear joint, dispersion curves and the emitted signal used in this study.

The computational model section encompasses the results of the wave propagation model, elastic-plastic structural model, and the damage detection model.

6.1. Experimental

6.1.1. Material Characterization

Figure 32 and Figure 33 present the engineering stress-strain curve obtained by the experimental tests carried out on an electromechanical universal TestResources® test frame of 50,000 Newton force capacity. The engineering curve is converted into the true stress-strain curve and the UTS value was identified.

Figure 32 also shows the material properties obtained experimentally from the 10 specimens of AA5083 under the specifications from the ASTM E8 [84]. The material properties of the adhesive Proset® ADV176/276 obtained experimentally under the specifications of the ASTM D638 [85] are shown in Figure 33

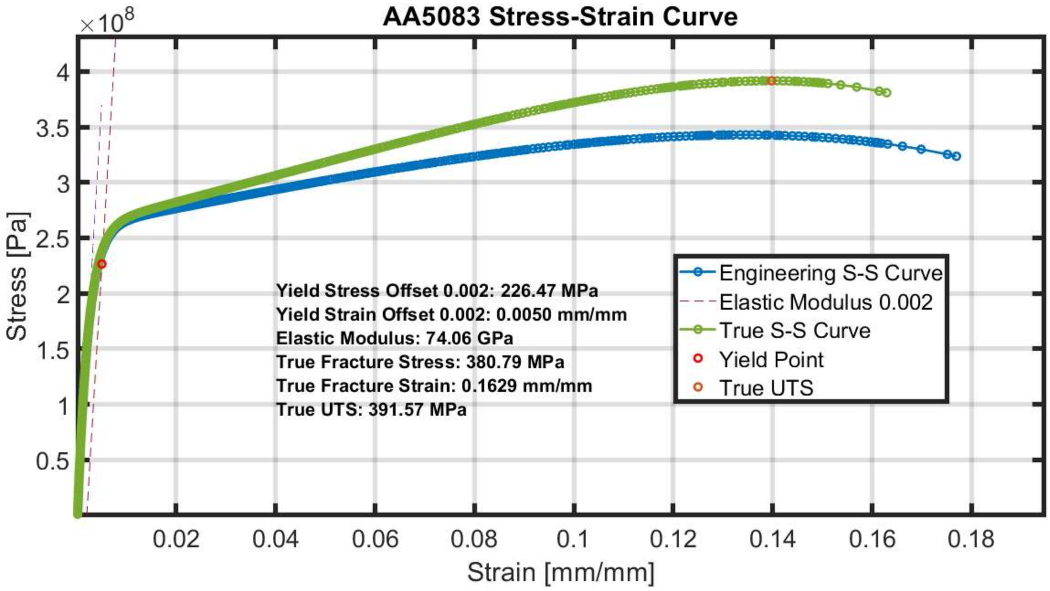

Figure 32. AA5083 Material Properties

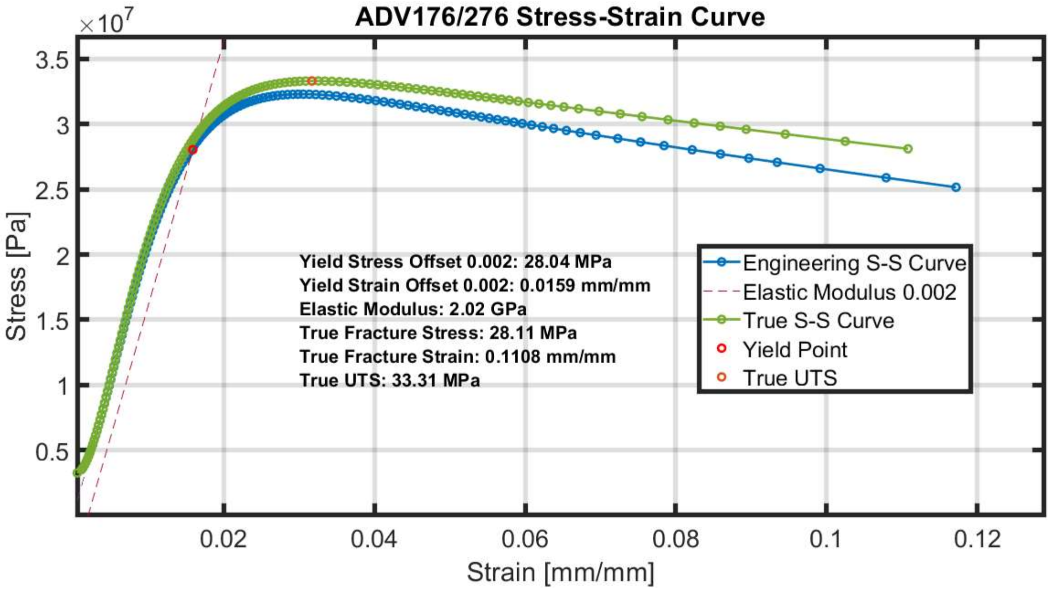

Figure 33. ADV176/276 Material Properties

6.1.2. Single lap shear joint

Table 2 shows the values needed for the design of SLSJ using the Eq. (18) and Eq. (19).

Table 2. Material properties

Property	AA5083	ADV 176/276
Ft_y	226 MPa	–
t	3.175 mm	3 mm
τ	–	10 MPa
E	74.06 GPa	2.02 GPa
ρ	2700 kg/m	1050 kg/m
ν	0.31	0.4

6.1.3. Dispersion curves

To obtain the dispersion curves was necessary to calculate the longitudinal and transverse wave speed of each material. The obtained values of the C_L and C_T, for each material are shown below in Table 3.

Table 3. Longitudinal and transversal wave speed

AA5083	ADV176/276
C_L = 6166 m/s	C_L = 2030 m/s
C_T = 3235 m/s	C_T = 828 m/s

To retrieve the dispersion curves from the Vallen AE-Suite Software it was needed to add as an input the material thickness from Table 2 and the C_L and C_T speeds from Table 3. This had as a result a frequency dependent graph for that specific thickness. Figure 34 shows the group velocity C_g for each material.

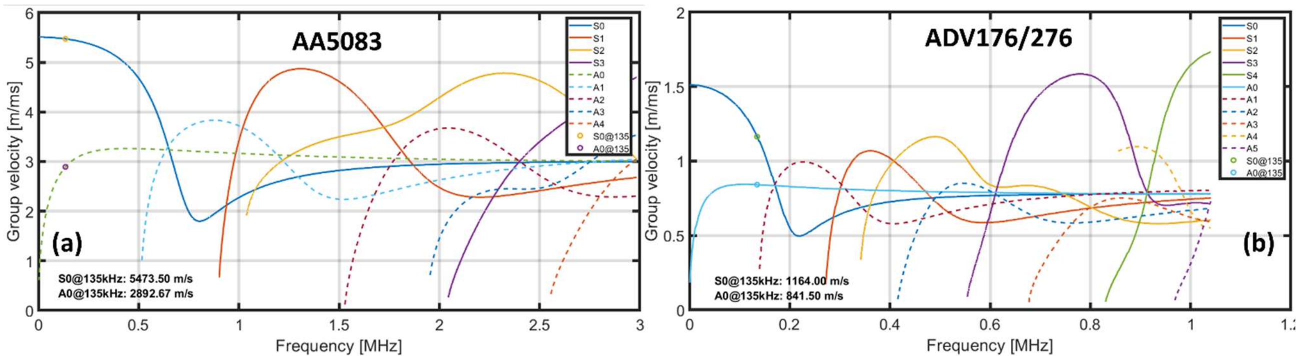

Figure 34. Dispersion curves

6.1.4. Emitted signal

Looking at the group velocities of both materials on Figure 34, it can be observed that the higher modes start appearing in a lower frequency on the ADV 176/276. This means that only frequencies between 0.05 and 0.14 MHz are free from high order modes. Subsequently, a frequency of 135 kHz was chosen for the 5 cycle Hanning window to avoid the creation of higher Lamb wave modes.

6.2. Computational model

6.2.1. Wave propagation model

6.2.1.1. Piezoelectric PZT transducer

Figure 35 shows the plotted contour of the displacement on the y-axis of the finite element model of the piezoelectric PZT transducer which was introduced on section 5.2.1. Table 4 contains a comparison of both methods to validate the computational model.

Table 4. PZT analytical and computational model comparison

Displacement due to a 10V		
Analytical	FEM	Percentage Difference
3.78 x 10^{-8} m	3.739 x 10^{-8} m	1.01

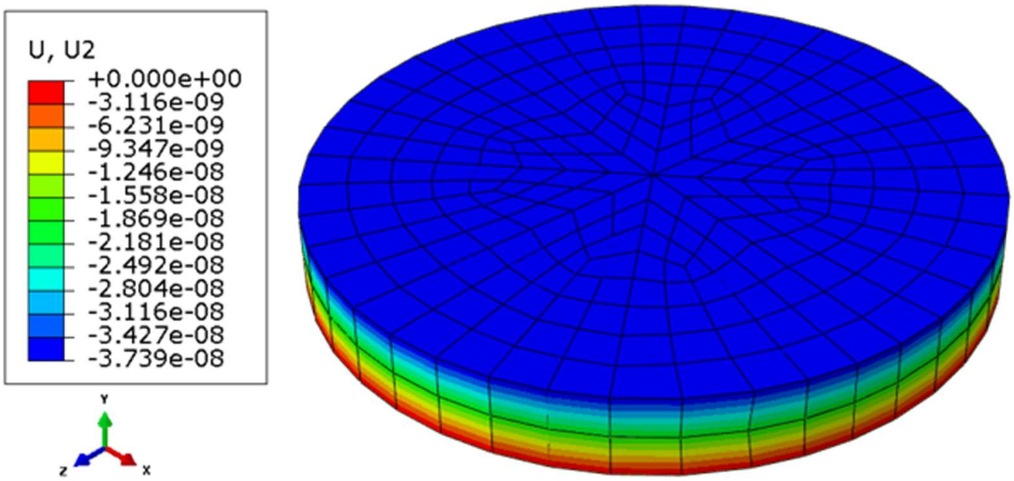

Figure 35. PZT transducer finite element model

6.2.1.2. Wave propagation convergence model

To achieve the temporal and spatial resolution on the wave propagation model, Eq. (21) and (22) were solved. For the temporal resolution Eq. (21) was considered. In this case, f_{max} was the frequency of the 5 cycle HW, 135 kHz. The result of the increment size obtained for the wave propagation model was equal to 0.37 microseconds. In the case of the spatial resolution, Eq. (22) was considered. The minimum wavelength, λ_{min}, present on the simulation was taken from the values of the dispersion curves on Figure 34. In this case, the adhesive presents the slowest wave speed at 135 kHz which is the anti-symmetric A_0 with a wavelength of 6.32×10^{-3} m. Using Eq. (22) and considering 10 nodes per wavelength, the obtained value for the spatial resolution was around 600 microns for a characteristic element size or size for the mesh element. Table 5 presents the results from the temporal and spatial resolution used for the wave propagation model.

Table 5. Mesh convergence study

Temporal	Spatial
0.37μs	620 μm

6.2.1.3. Stiffness reduction method

The performance of the developed SRM was compared on a single coupon model with and without SRM, as shown in Figure 36, to validate the efficiency of the chosen technique.

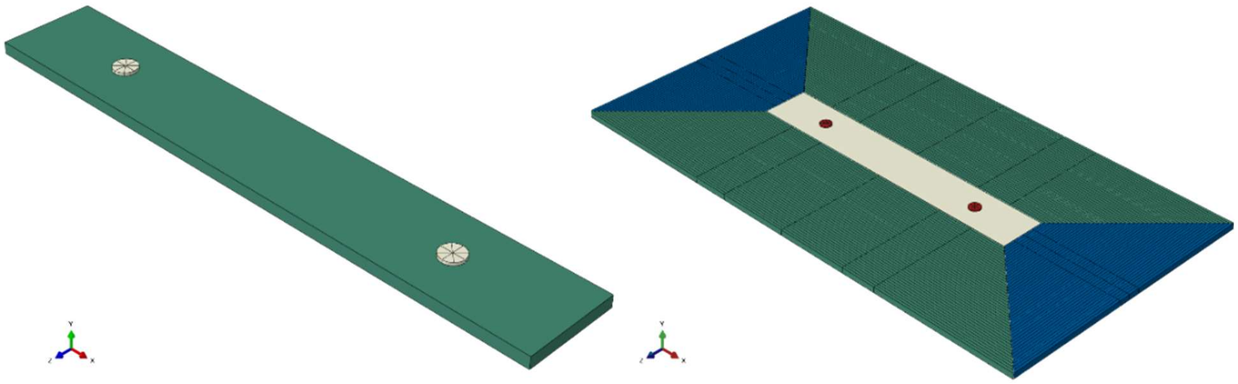

Figure 36. Simple coupon model and SRM coupon model

Figure 37 shows the results of the validation of the performance of the SRM on the mentioned scenario. Boundary reflections are being absorbed by the added layers.

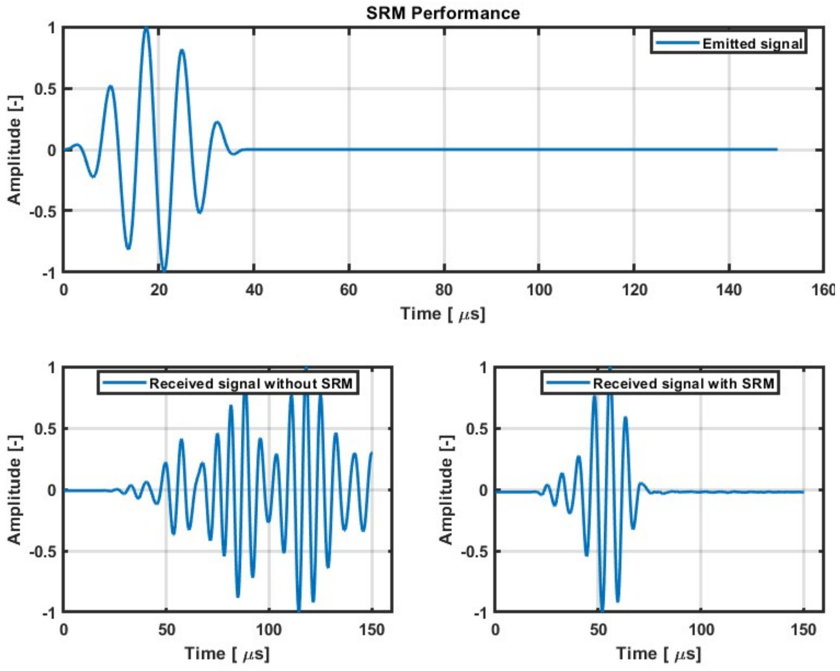

Figure 37. SRM Performance

This method was implemented after on the SLSJ where it was computational justified as having a larger coupon on the study, but without an excessive area to avoid the reflections. Time of simulation was reduced with the usage of this method while increasing the accuracy of the obtained results.

6.2.2. Elastic-plastic structural model

6.2.2.1. Mesh convergence

Figure 38 shows three stress-strain curves taken from the path line along the middle of the adhesive showed on Figure 27 for an element mesh size of 800, 400 and 200 µm. The result shows the difference stress values at the same location of the adhesive and graphed for a coarse, medium and fine mesh.

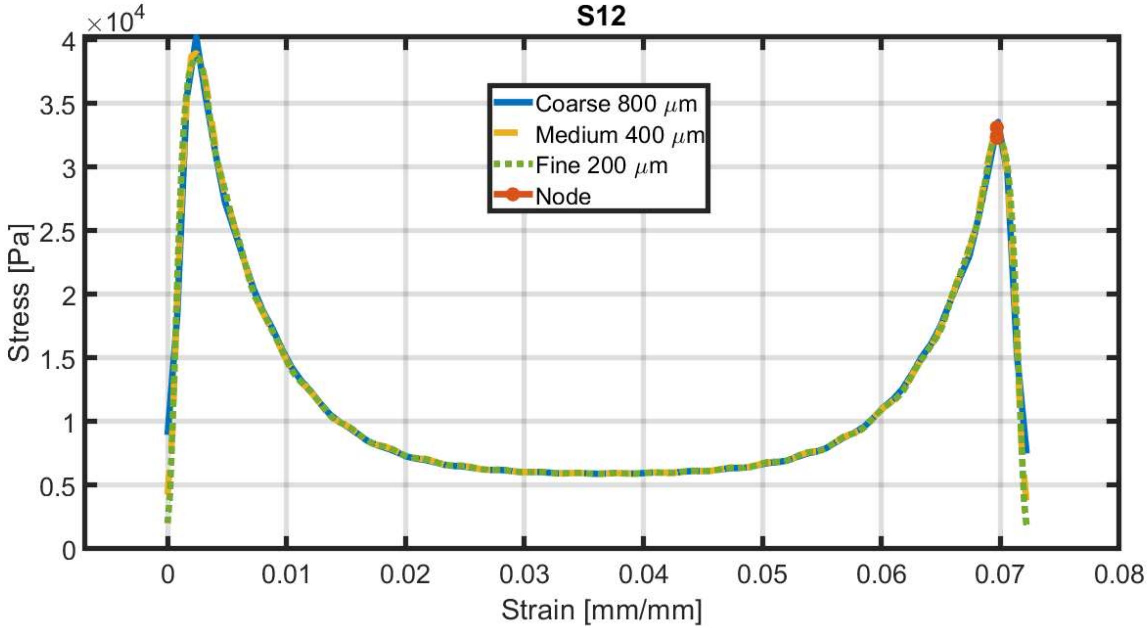

Figure 38. Shear stress-strain curve on the bond line

The results of the mesh convergence study on Figure 39a shows the stresses values and the computational solving time plotted against the element mesh size for each of the cases. The Richardson extrapolation methodology was used to select a proper mesh size avoiding excessive computational time.

To select the correct element mesh size, a percentage of error from Figure 39a was calculated. Figure 39b shows the percentage of error from each simulation compared to the value obtained from the Richardson extrapolation methodology, where the percentage of error would be equal to zero.

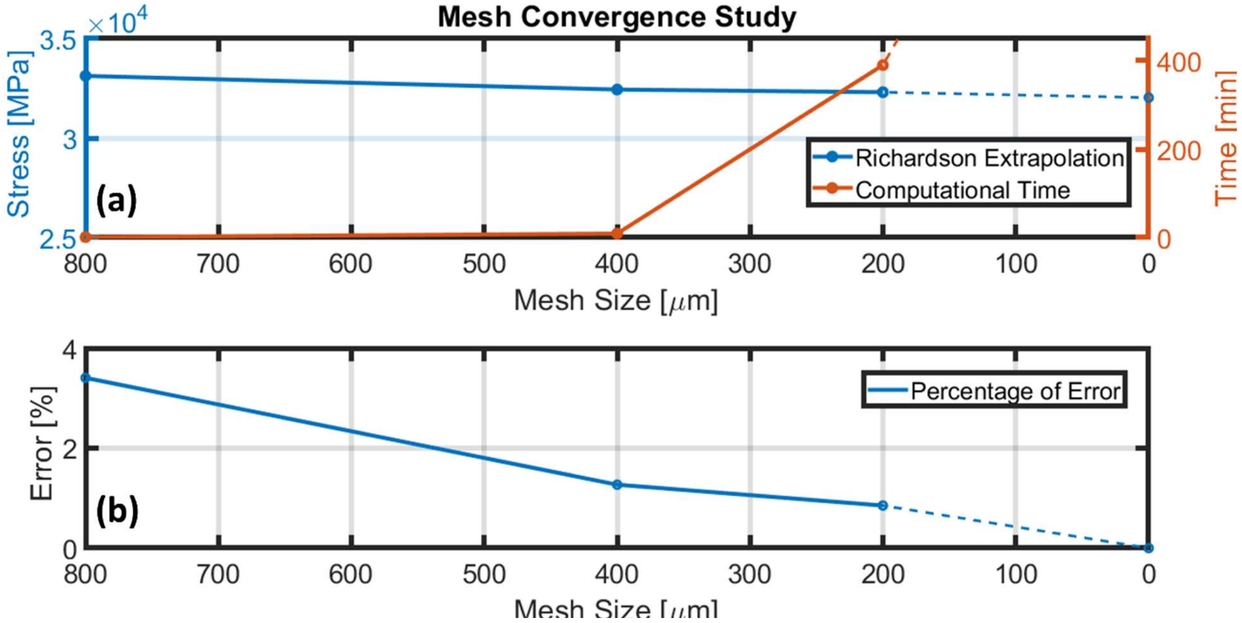

Figure 39. Mesh convergence study

The chosen element mesh size for the finite element model was 400 µm. This was due to the low percentage of error obtained with a mesh of 400 µm compared to extrapolated value of zero µm mesh size of the Richardson extrapolation. Besides the percentage of error, the computational time is considerably lower than the one obtained for 200 µm.

6.2.2.2. Damage criteria

The development of the computational ductile damage criterion was made based on the stress-strain curves obtained from the experimental material characterization showed Figure 32 and Figure 33, for AA5083 and ADV176/276, respectively.

Figure 40 and Figure 41 shown the results of the MATLAB® script developed to obtain the input values for the ductile damage and damage evolution of the AA5083 and ADV176/276 required on ABAQUS CAE™.

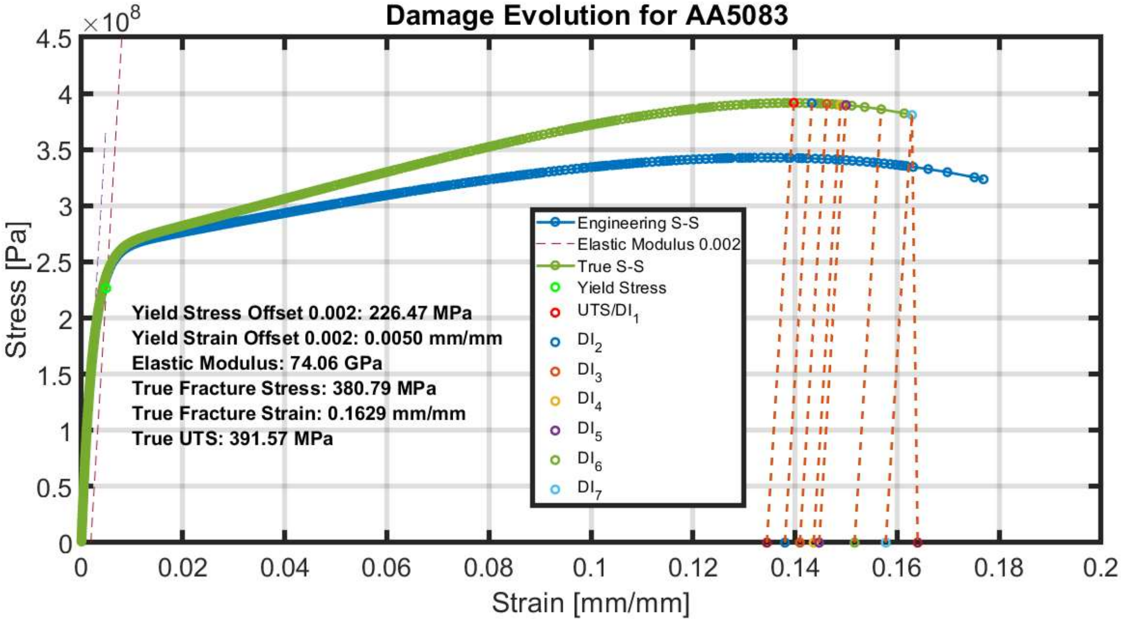

Figure 40. Damage evolution for AA5083

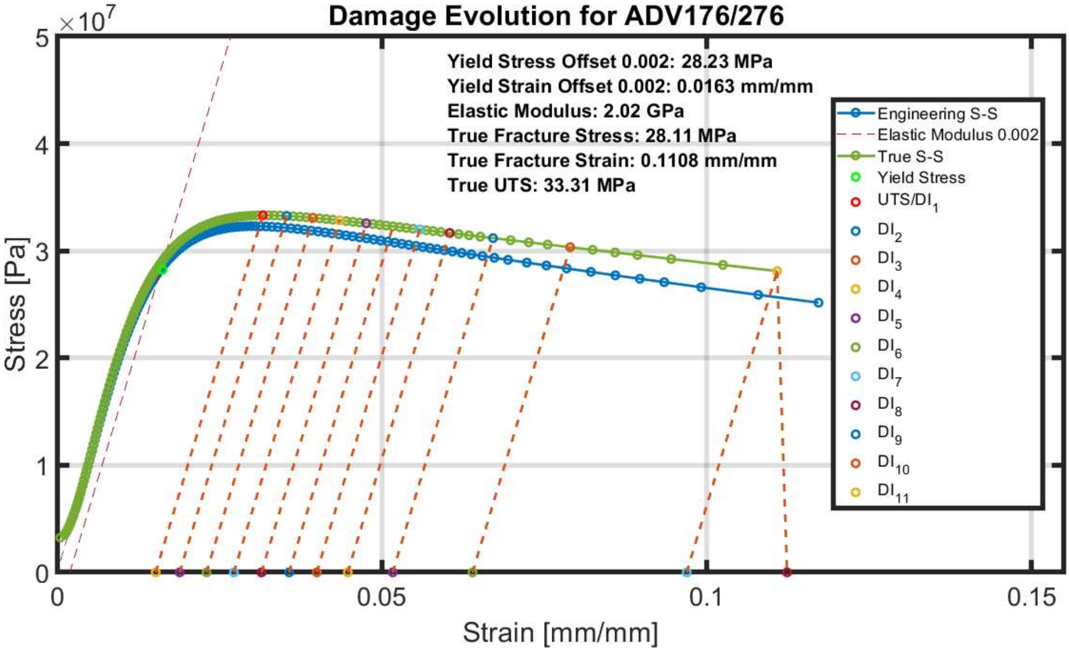

Figure 41. Stress-strain curve for ductile damage ADV176/276

As shown on the legend of the figures, the damage index (DI) is represented as bullets positioned on the true stress-strain curve, while the strain was shown at the bottom end of each plotted slope. Table 6 presents a summary of the input values for the ductile damage for each material.

Table 6. Ductile damage

	AA5083	ADV176/276
Fracture Strain	0.134476	0.0146443
Stress Triaxiality	-0.33	-0.33
Strain rate	0	0

For the damage evolution, ABAQUS CAE^{TM} requires a displacement value at each DI. Displacement values are calculated considering the strain at each DI times the characteristic length, meaning the size of the used element. This process was employed in both materials [69]. Table 7 and Table 8 shown the input values obtained from the MATLAB$^{®}$ script

Table 7. AA5083 damage evolution

DI	Displacement
0	0
3.242E-04	3.536E-06
1.028E-03	6.488E-06
2.034E-03	9.182E-06
2.538E-03	1.026E-05
7.275E-03	1.722E-05
1.376E-02	2.335E-05
1	3.171E-05

Table 8. ADV176/276 damage evolution

DI	Displacement
0	0
1.670E-04	3.694E-06
6.950E-04	7.828E-06
1.416E-03	1.204E-05
2.231E-03	1.628E-05
3.089E-03	2.054E-05
3.967E-03	2.480E-05
4.957E-03	2.957E-05
6.394E-03	3.649E-05
8.935E-03	4.879E-05
1.562E-02	8.176E-05
1	1

The calculated parameters on Table 7 and Table 8 were then introduced into the single element model shown in Figure 28. The deformation of the single element can be seen in Figure 42 for both cases, where (a) AA5083 and (b) ADV176/276. The single element reaches the maximum material deformation before being deleted. With this, ABAQUS CAE^{TM} intended to mimic the failure of the material. The result matches the expected behavior since it was only one element, therefore no necking should be present in the simulation.

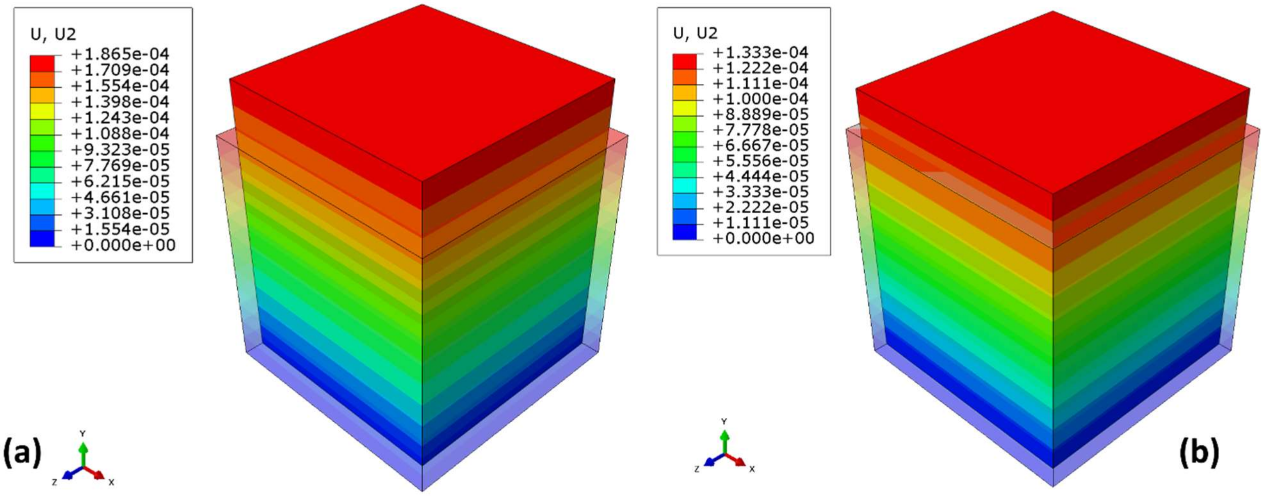

Figure 42. Displacement of the single element size model

The stress-strain curves were taken from the results of the single finite element model and then validated with the experimental data for each material. The obtained results and comparison are showed on Figure 43 for the AA5083 and Figure 44 for the ADV176/276.

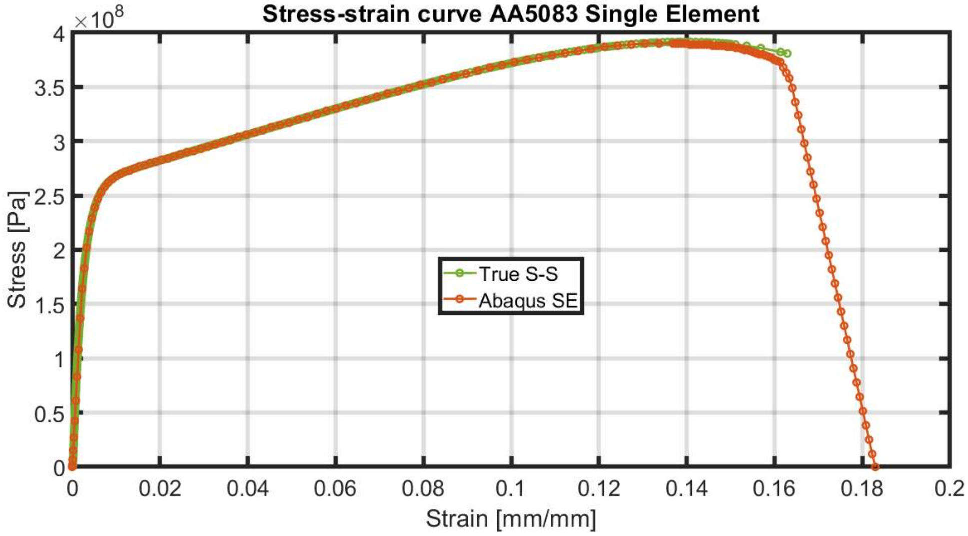

Figure 43. Ductile damage behavior on AA5083

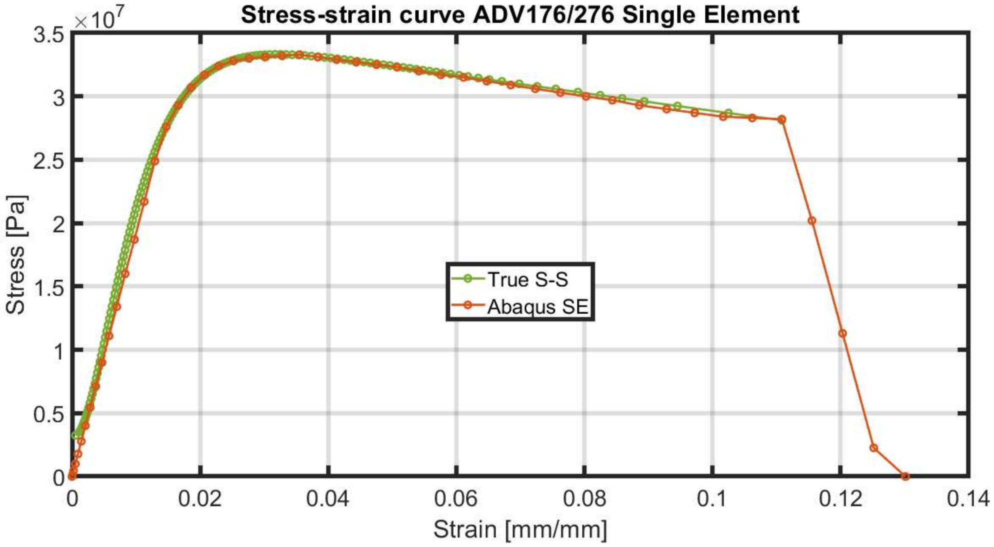

Figure 44. Ductile damage behavior on ADV176/276

6.2.3. Damage detection model

In this section, the results of the TRM applied to the SLSJ on a pristine condition and induced damage scenario are presented. Also, the results of the TRM used on the before and after damage initiation and before failure are presented.

The first set of results presented are on the pristine SLSJ, where a no-damaged condition was present on the adhesive nor the adherends are shown in Figure 45.

Figure 45a shows the emitted 5 cycle HW signal at the piezoelectric PZT transducer X, (b) the response signal of the structure received on piezoelectric PZT transducer Y, (c) the time reverse of (b) which was re-emitted to transducer X. Figure 45d presents the received signal at transducer X.

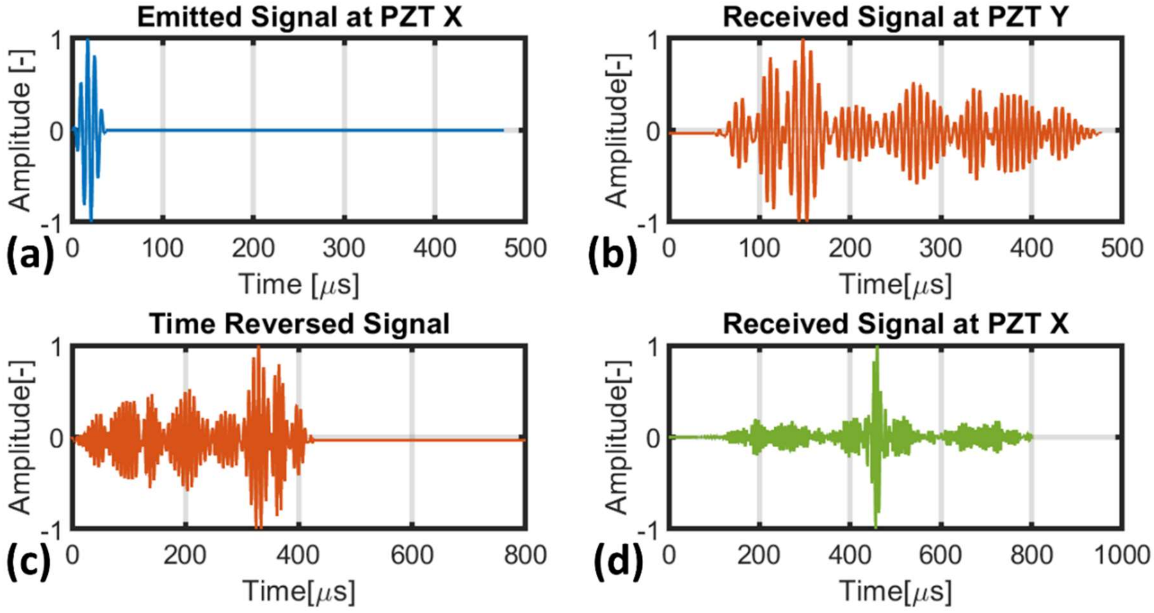

Figure 45. TRM on pristine condition

The received signal on Figure 45d was post-processed using the convolution function of signals. This means the generation of a third signal that provide a moment in time where the convolution of the two signals reached a maximum energy value. The post-processing of the signal using the convolution function is shown in Figure 46.

On Figure 46, (a) and (b) represent the initial 5 cycle HW emitted and the received signal at X transducer. These signals were subjected to a convolution process, whereas stated in Eq.(15), one signal was time reversed and convoluted at every step time with the other one. This process is showed on (c) where the received signal was time reversed and convolute with (a). In this study, the highest peak of (a) was taken as the section of reference to be convoluted with the TR of (b). This peak happens at 17.39 µs. A window of 7.7 µs was selected as reference, where the highest peak was at 4.7 µs. On the convolution process in (c), the highest peak was shown as a static signal while the TR of (b) moved along the time and convolute to create a new signal.

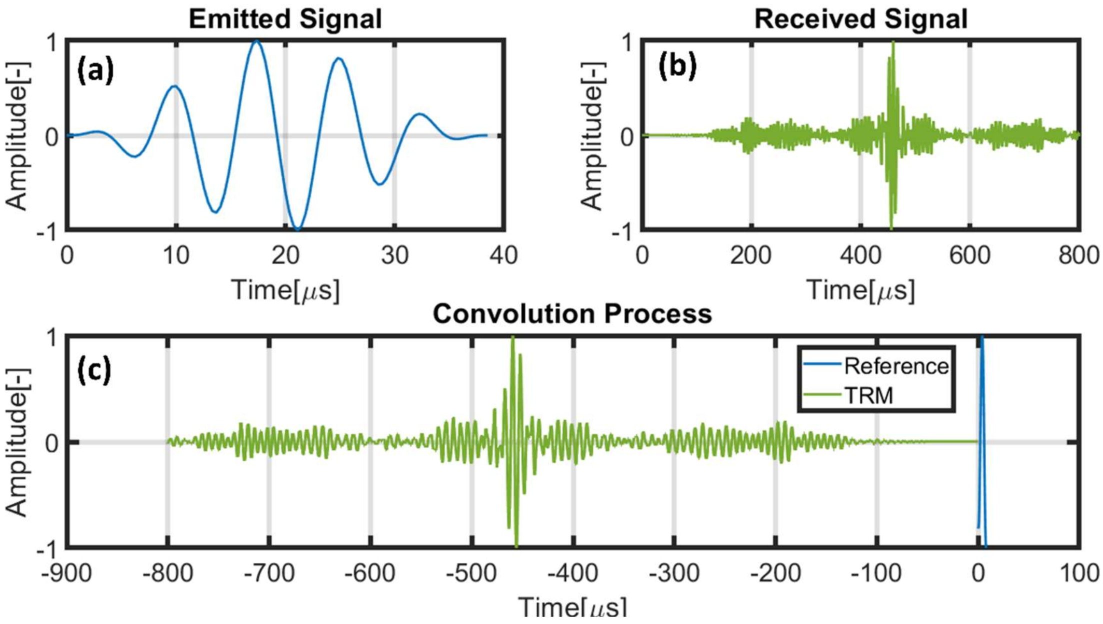

Figure 46. Pristine condition convolution process

The result of the convolution process shown in Figure 47, allowed to identify the amount of energy produced from the convolution. In other words, the highest peak or highest amount of energy translates to where in time the received signal at the transducer X was like the reference peak of the initial emitted signal.

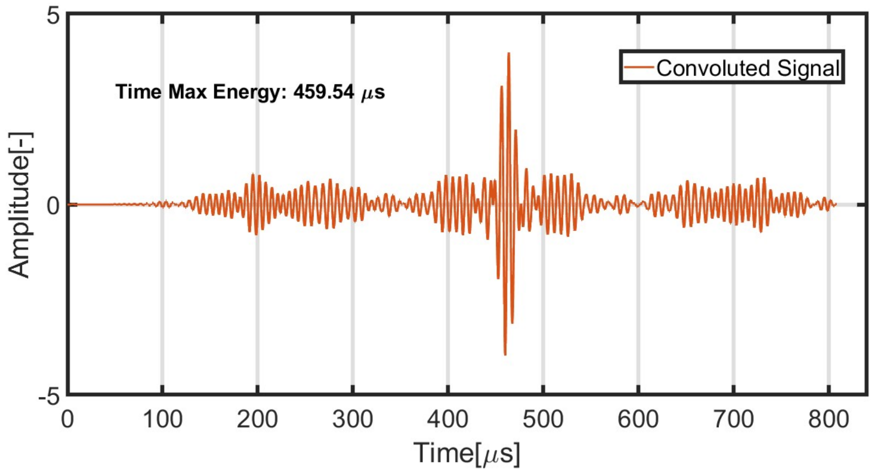

Figure 47. Pristine convoluted signal

At 459.54 microsecond was recorded to be the highest amount of energy on the convoluted signal. Figure 48a indicates the time and section of the convoluted signal that contains the highest amount of energy. Figure 48b shows a time reversed of the convoluted signal. This indicates the position in time of the highest amount of energy of the received signal on Figure 45d.

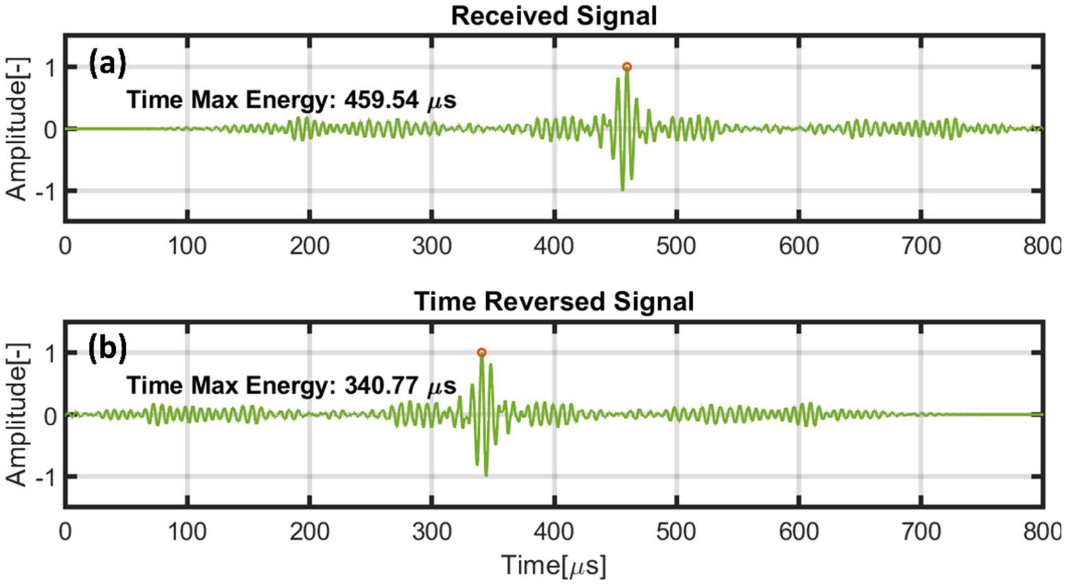

Figure 48. Maximum energy peak pristine condition

After identifying the time of maximum energy on the time reversed signal, a window of time was selected to compare with the original signal. The window selected has a 38.48 µs length, which is the length of the original signal. For the selection of this period on the time reversed signal, the highest peak was taken as reference. The window selected to obtain a reconstructed signal on the time reversed signal was 17.39 µs before and 21.09 µs after the highest peak to obtain the 38.48 µs window.

A cross-correlation function was employed as a statistical parameter to obtain an R^2 value, which quantified the correlation of the two signals. Figure 49 shows the comparison between the original emitted and the reconstruction of signal. The similarity of the signals was easily detected by visual methods and the obtained R-value of 97.52% re-affirm as a statistical method the similarity between the two signals on a pristine condition SLSJ.

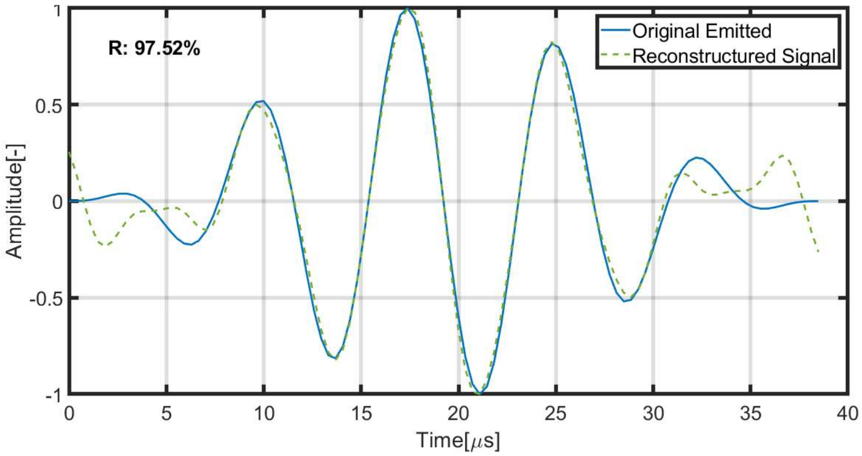

Figure 49. Original and reconstructed signal comparison – pristine condition

Figure 50 presents the result of the TRM on the introduced damaged condition showed on Figure 31. Where in Figure 50, (a) shows the emitted 5 cycle HW signal at the piezoelectric PZT transducer X, (b) the response signal of the structure received on piezoelectric PZT transducer Y. At this point, the process was the same as the one shown on Figure 45, this means that the first steps of the process are done in a healthy condition of the SLSJ. Then (c) is the time reversed signal of (b) which was re-emitted to transducer X. For this step, the damage was introduced on the adhesive of the SLSJ. Figure 50d shows the received signal at transducer X for an introduced damage scenario on the adhesive.

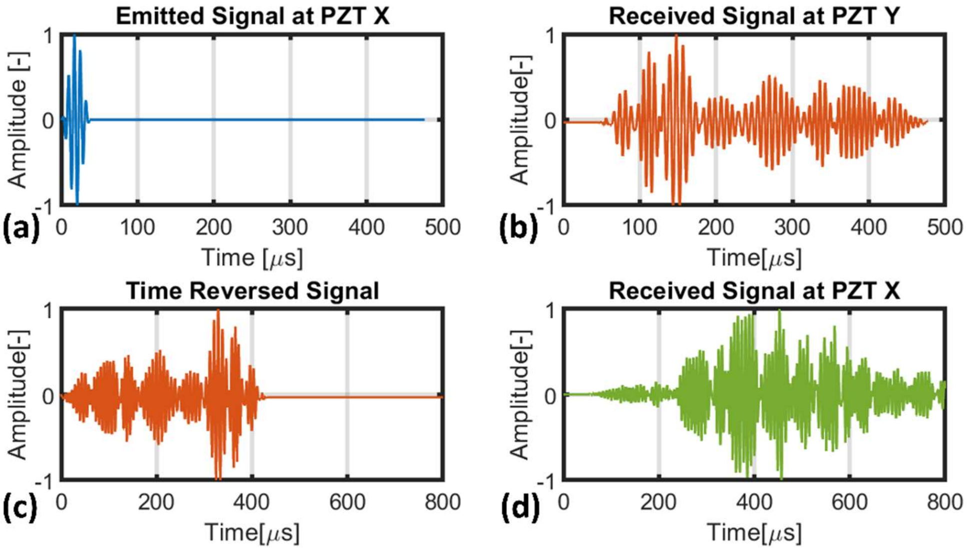

Figure 50. TRM on introduced damage condition

The received signal, on Figure 50d, was post-processed using the convolution function of signals and shown in Figure 51.

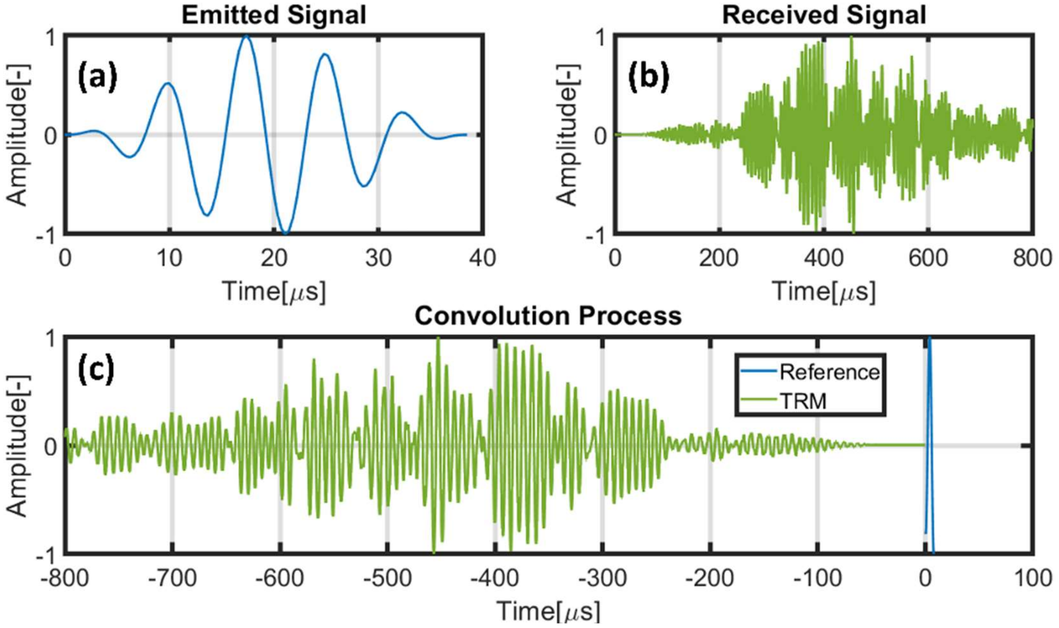

Figure 51. Introduced damage condition convolution process

Figure 52 shows the result of the convolution process for the introduced damage condition.

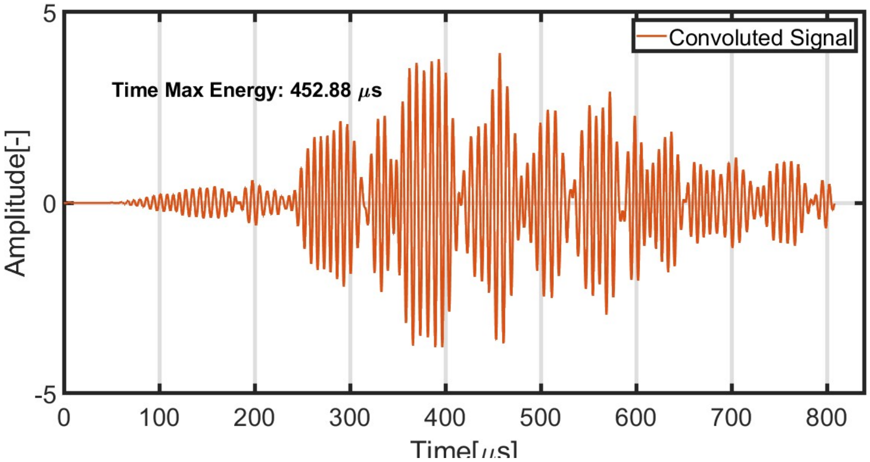

Figure 52. Introduced damage condition convolution signal

At 452.88 microsecond was recorded to be the highest amount of energy on the convoluted signal. Figure 53a indicates the time and section of the convoluted signal that contains the highest amount of energy. Figure 53b shows a time reversal of the convoluted signal. This indicates the position in time of the highest amount of energy of the received signal on Figure 50d.

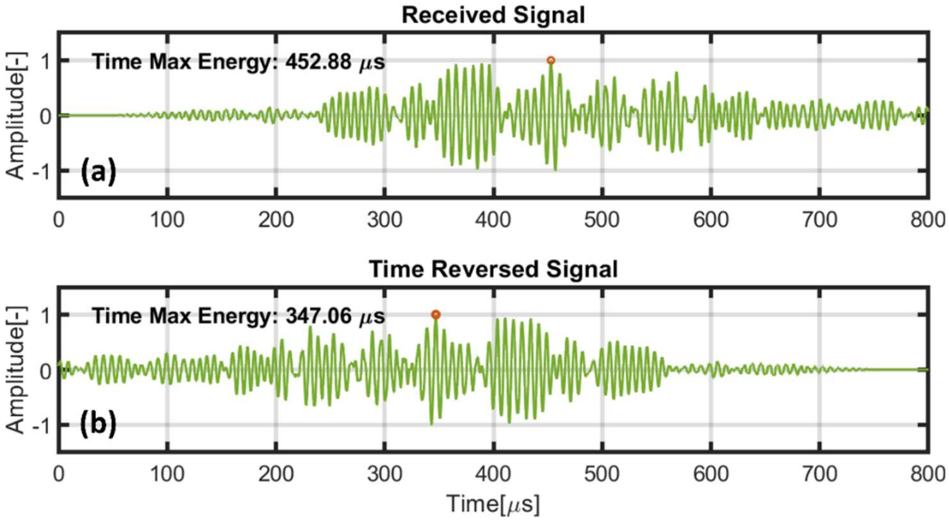

Figure 53. Maximum energy peak introduced damage condition

The window for comparison was selected from the time of the maximum energy on the time reversed signal. Same considerations as the pristine condition were taken for the introduced damage case. The cross-correlation function was employed as a statistical parameter to obtain an R^2 value of the similarity of the signals. Figure 54 shows the comparison between the original emitted and the reconstructed signal. The similarity of the signals was easily detected by visual inspection and the obtained R^2-value of 90.92 % re-affirm as a statistical method the similarity of the two signals on an embedded damage condition on a SLSJ.

The accuracy of the methodology used for the damage detection was validated with the pristine and introduced damaged condition models. The presence of damage using the time reversal method can be appreciated and verified through statistical means.

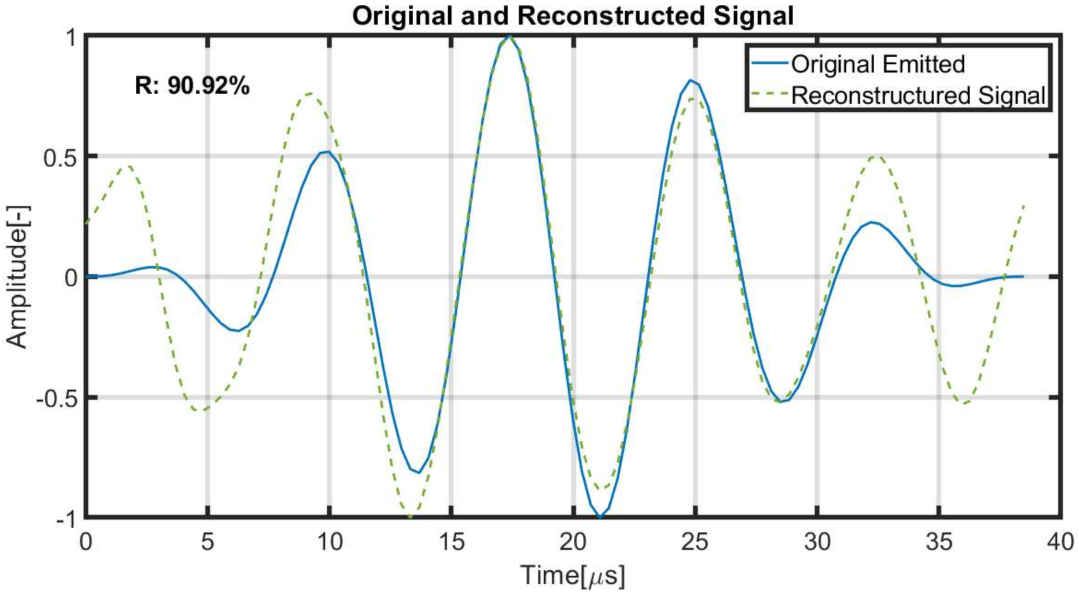

Figure 54. Original and reconstructed signal comparison – introduced damage condition

The results of the damage criteria section were introduced on the SLSJ model to recreate a realistic initiation and development of damage on the adhesive when the SLSJ was subjected to a tensile test as specified in the ASTM D1002. Figure 55 shows the SLSJ model used for the next iterations of damage nucleation on the SLSJ. This model does not contain SRM on the adhesive part since elements were removed from the SRM by the ductile damage, and it did not fulfill the purpose of signal dissipation.

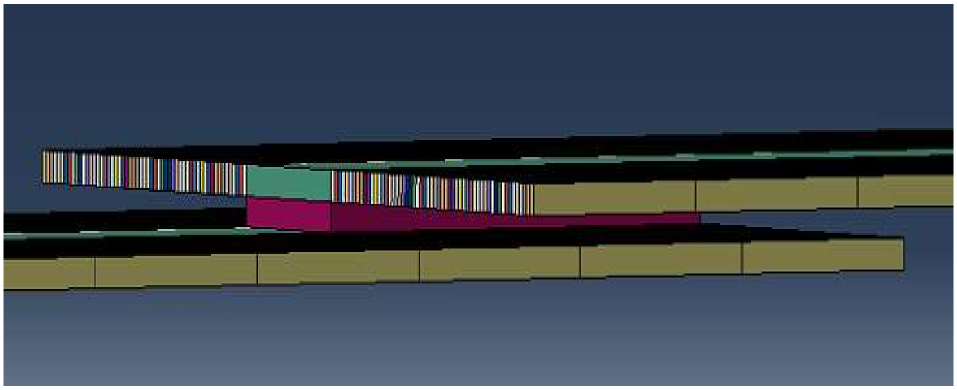

Figure 55. Ductile damage on SLSJ model

Three different iterations were proposed for the study for damage detection using a damage propagation model on the SLSJ. The first iteration was set prior to a damage condition, shown in

Figure 56, where the adhesive was at a moment in time right before the nucleation of a crack. The adhesive was still in a pristine condition, but the propagation media was deformed.

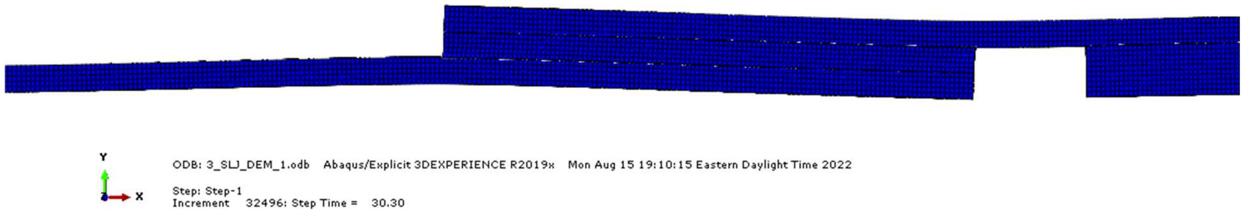

Figure 56. Prior to damage nucleation

Figure 57 presents the result of the TRM on the before damage condition of the SLSJ shown on Figure 56. Where in Figure 57, (a) shows the emitted 5 cycle HW signal at the piezoelectric PZT transducer X, (b) the response signal of the structure received on piezoelectric PZT transducer Y. At this point of the process, it is the same as the one shown on Figure 45, this means that the first steps of the process were done on a healthy condition of the SLSJ. Then (c) is the time reversal of (b) which was re-emitted to transducer X. In this step, the wave propagates through the SLSJ as shown in Figure 56. The SLSJ was at a deformed condition where the adhesive was with no damage. Figure 57d presents the received signal at transducer X a moment before the damage nucleated.

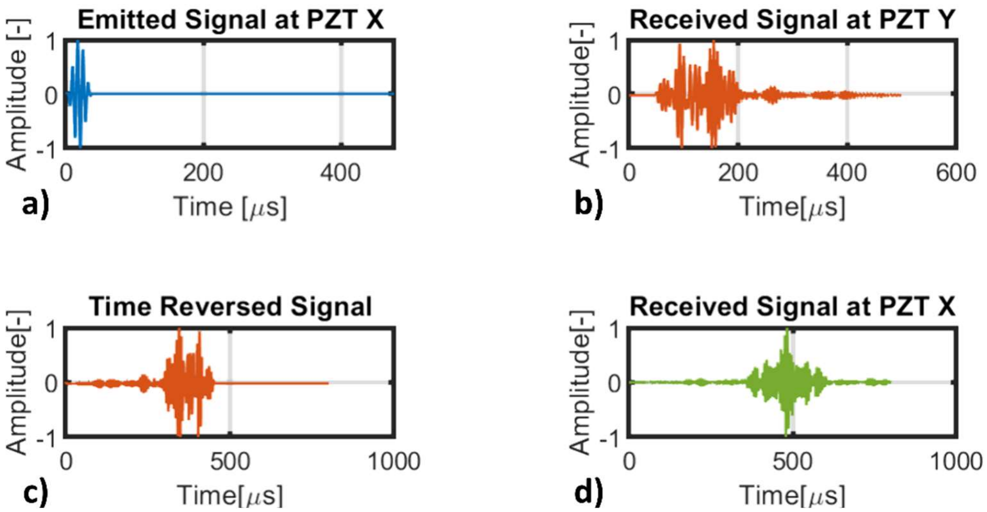

Figure 57. TRM on before damage condition

The received signal, on Figure 57d, was post-processed using the convolution function of signals and shown in Figure 58.

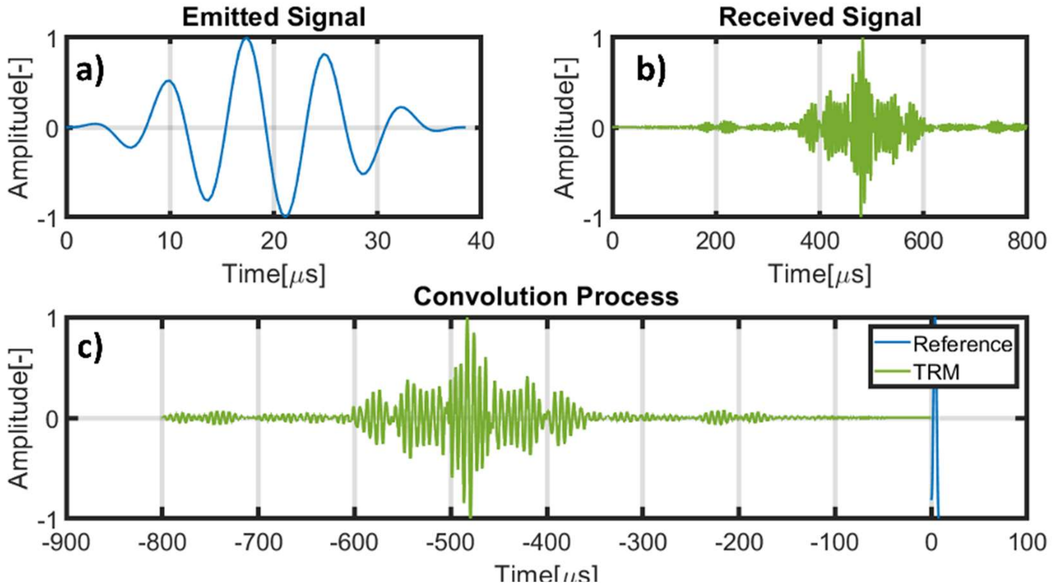

Figure 58. Before damage condition convolution process

Figure 59 shows the result of the signal convolution process for the before damage condition.

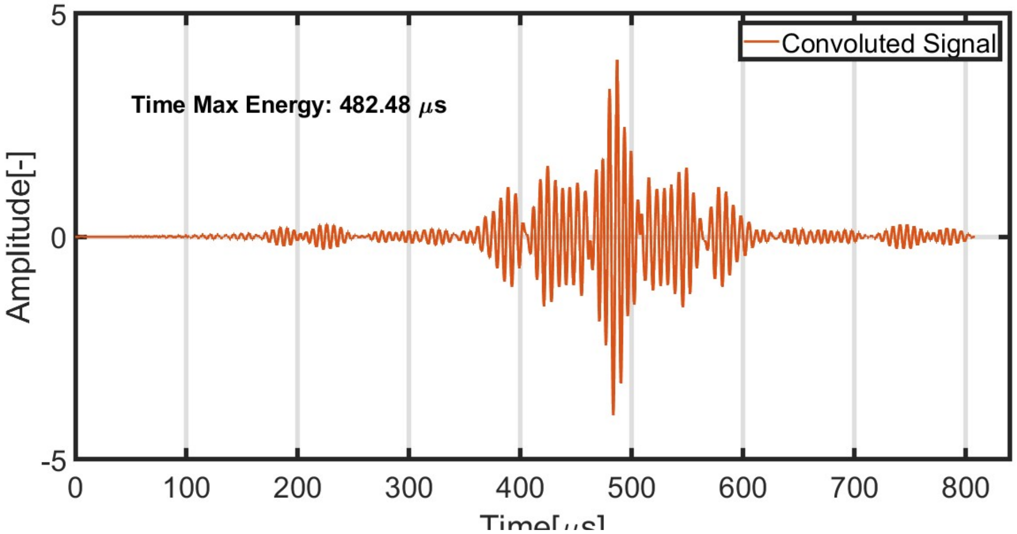

Figure 59. Before damage condition convolution signal

At 482.48 µs was recorded to be the highest amount of energy on the convoluted signal of the before damage condition on the adhesive. Figure 60a indicates the time and section of the convoluted signal that contains the highest amount of energy. Figure 60b shows a time reversed of the convoluted signal. This indicates the position in time of the highest amount of energy of the received signal on Figure 57d.

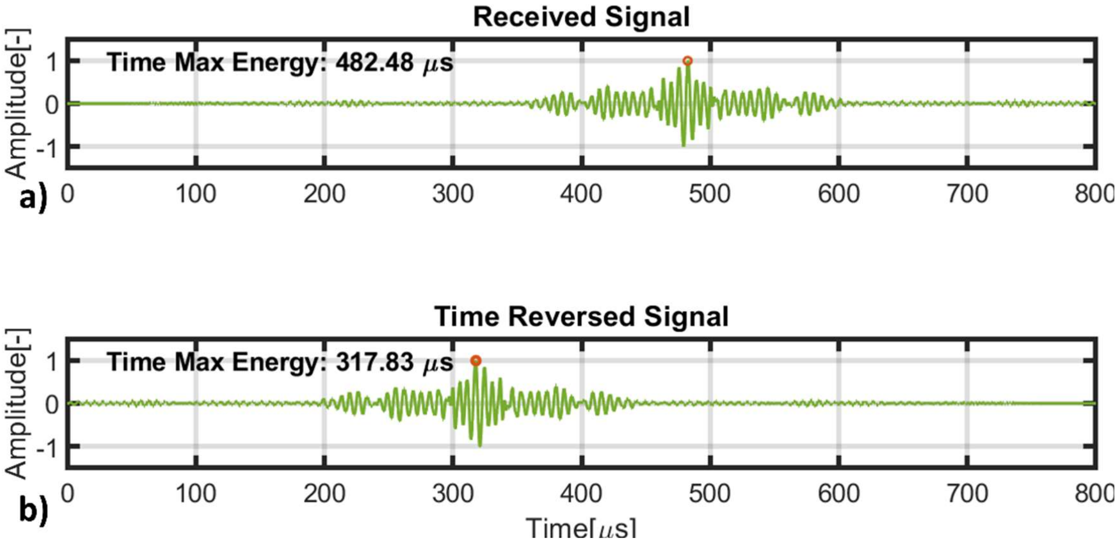

Figure 60. Maximum energy on a before damage condition

As stated in the previous analysis made, the window for comparison was selected from the time of the maximum energy on the time reversed signal. Figure 61 shows the comparison between the original emitted and the reconstruction of signal. The non-similarity of the signals was easily detected by visual inspection and the R^2-value of 70.66 % was obtained. Even though there was no damage present, a lower value compared to the previous analysis was expected due to the missing SRM on the adhesive in this model.

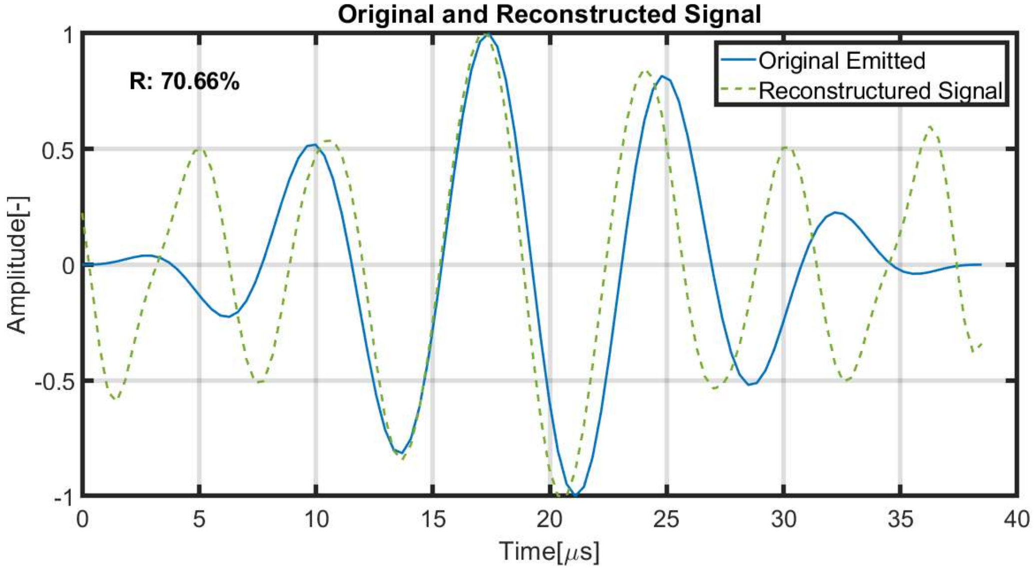

Figure 61. Original and reconstructed signal comparison – before damage condition

The second iteration case was set a moment right after the adhesive shows the nucleation of the crack. Figure 62 shows the moment in time taken for this iteration and it can be appreciated how the elements are being removed from the adhesive. Figure 38 proves the highest stresses presented on the adhesive where at the edges according to the element deletion function of the damage evolution material model.

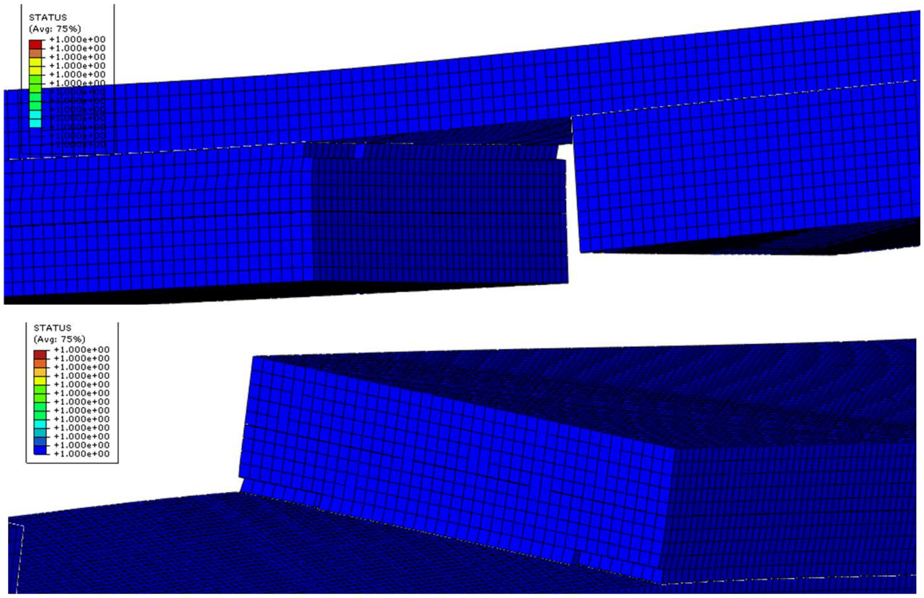

Figure 62. After damage condition

Figure 63 presents the result of the TRM on the after-damage condition of the SLSJ showed on Figure 62. Where in Figure 63, (a) shows the emitted 5 cycle HW signal at the piezoelectric PZT transducer X, (b) the response signal of the structure received on piezoelectric PZT transducer Y. At this point, the process was the same as the one shown on Figure 45, this means that the step a) and b) were taken from a healthy condition of the SLSJ. Then (c) is the time reversal of (b) which was re-emitted to transducer X. In this step, the damage nucleation was visible due to the removal of elements on the adhesive of the SLSJ. Figure 63d presents the received signal at transducer X when the adhesive presents damage initiation.

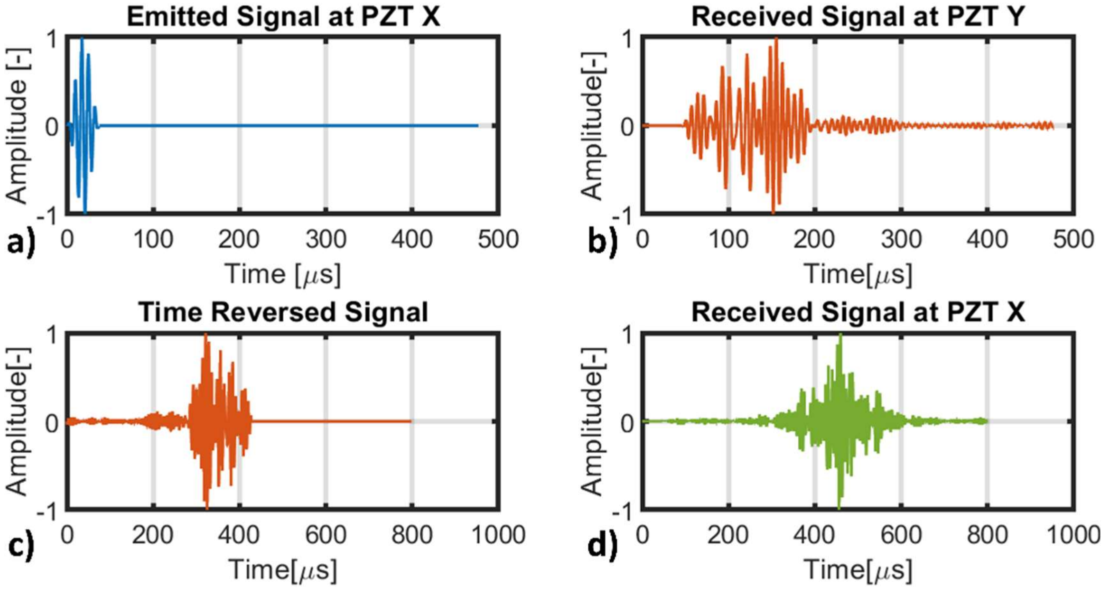

Figure 63. TRM on after damage condition

The received signal, on Figure 63d, was post-processed using the convolution function of signals and shown in Figure 64.

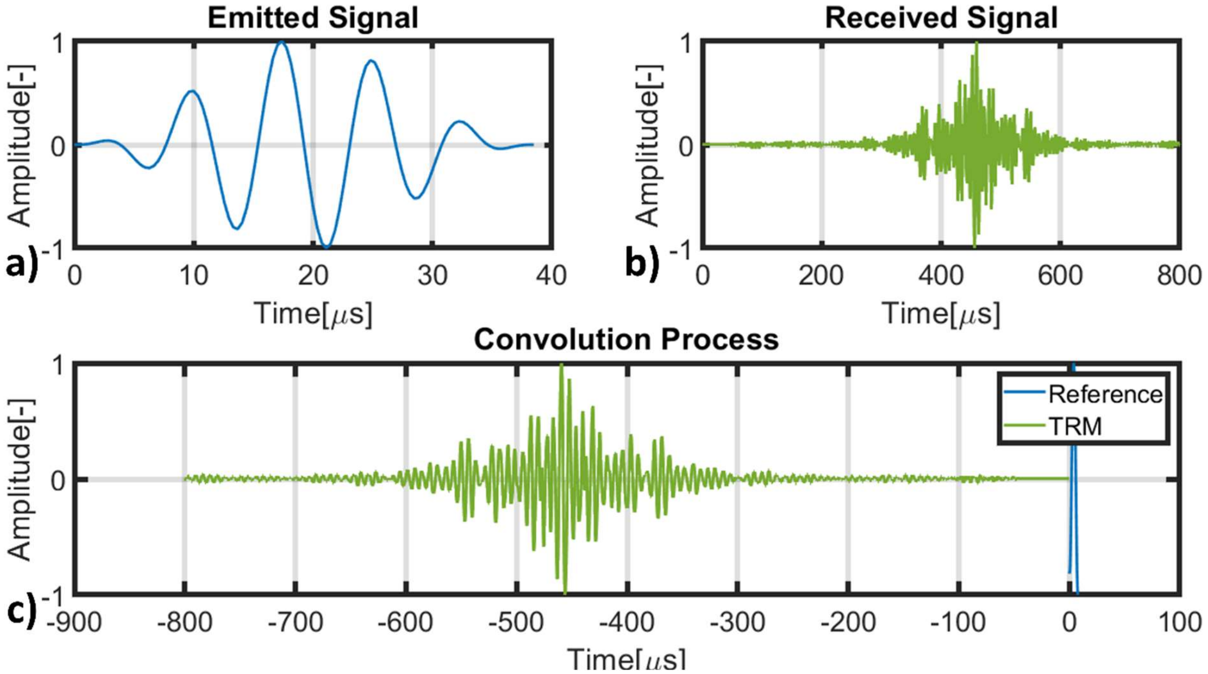

Figure 64. After damage condition convolution process

The result of the convolution process for the after-damage condition is shown in Figure 65.

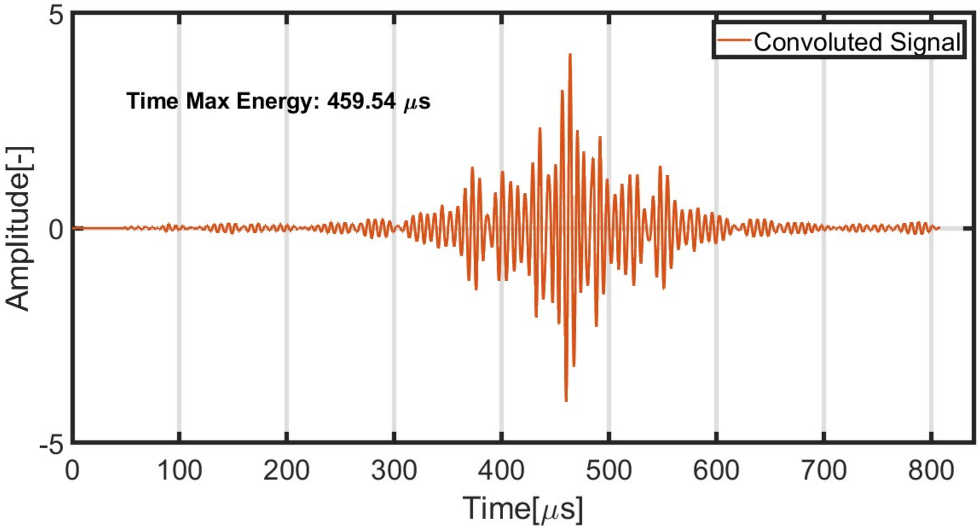

Figure 65. After damage condition convolution signal

At 459.54 μs was recorded to be the highest amount of energy on the convoluted signal of the after-damage condition on the adhesive. Figure 66a indicates the time and section of the convoluted signal that contains the highest amount of energy. Figure 66b shows a time reversed of the convoluted signal. This indicates the position in time of the highest amount of energy of the received signal on Figure 63d.

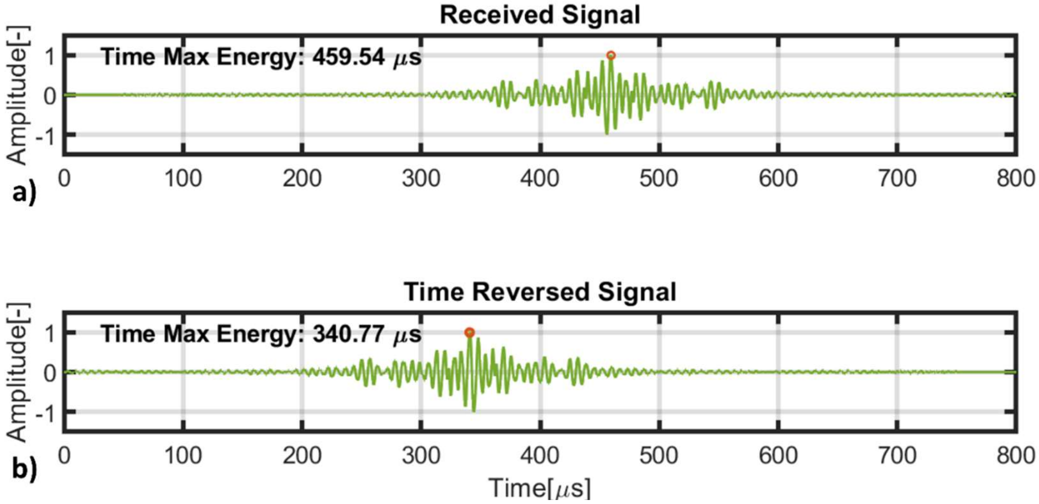

Figure 66. Maximum energy peak after damage condition

As stated in the previous analysis made, the window for comparison was selected from the time of the maximum energy on the time reversed signal. The comparison between the original emitted and the reconstruction of signal of the after-damage condition is shown in Figure 67. An R^2-value of 81.95 % was obtained.

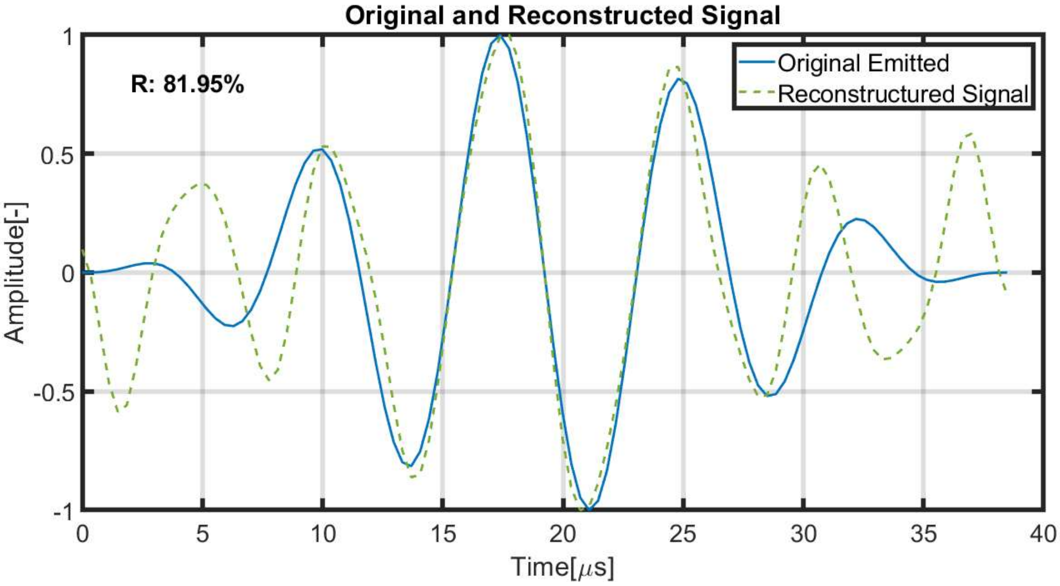

Figure 67. Original and reconstructed signal comparison – after-damage condition.

Figure 68 shows the last case where the adhesive was at a moment before complete failure of the SLSJ. The adhesive does not contain most of the elements which indicate the propagation of the fracture from the edges to the middle of the adhesive.

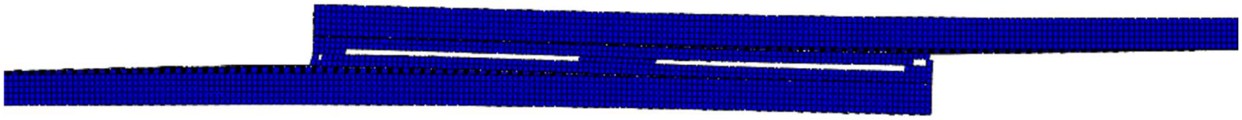

Figure 68. Before failure condition

Figure 69 presents the result of the TRM on the before failure condition of the SLSJ shown on Figure 68. Where in Figure 69, (a) shows the emitted 5 cycle HW signal at the piezoelectric PZT transducer X, (b) the response signal of the structure received on piezoelectric PZT transducer Y. At this point of the process, it is the same as the one showed on previous analysis, this means that the first steps of the process were done in a healthy condition of the SLSJ. Then (c) is the time reverse of (b) which was re-emitted to transducer X. Figure 69d presents the received signal at transducer X when the adhesive of the SLSJ was at a moment in time before failure.

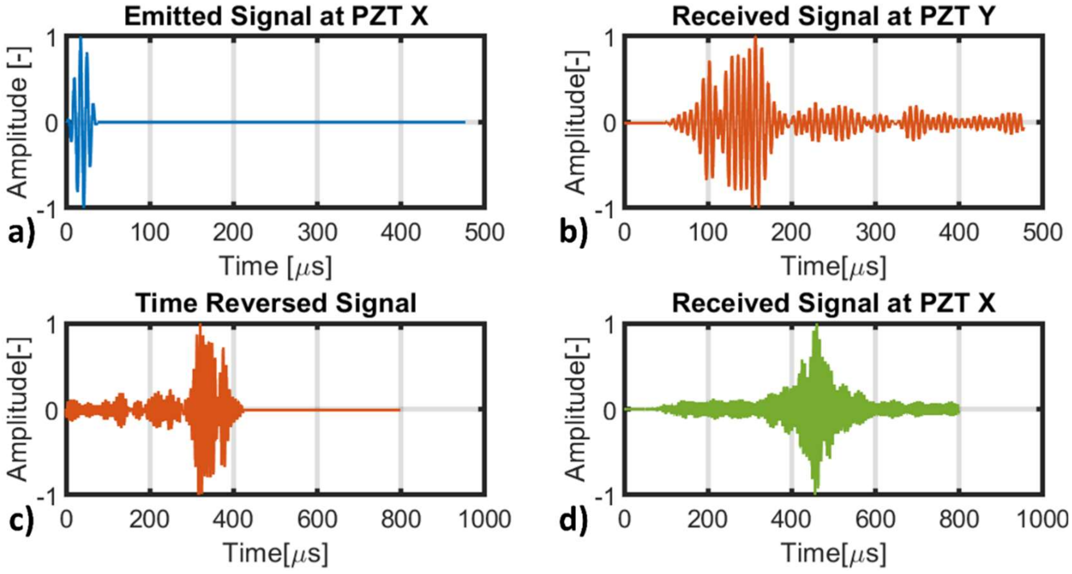

Figure 69. TRM on before failure condition

The received signal, on Figure 69d, was post-processed using the convolution function of signals. The post-processing of the signal using the convolution function is shown in Figure 70.

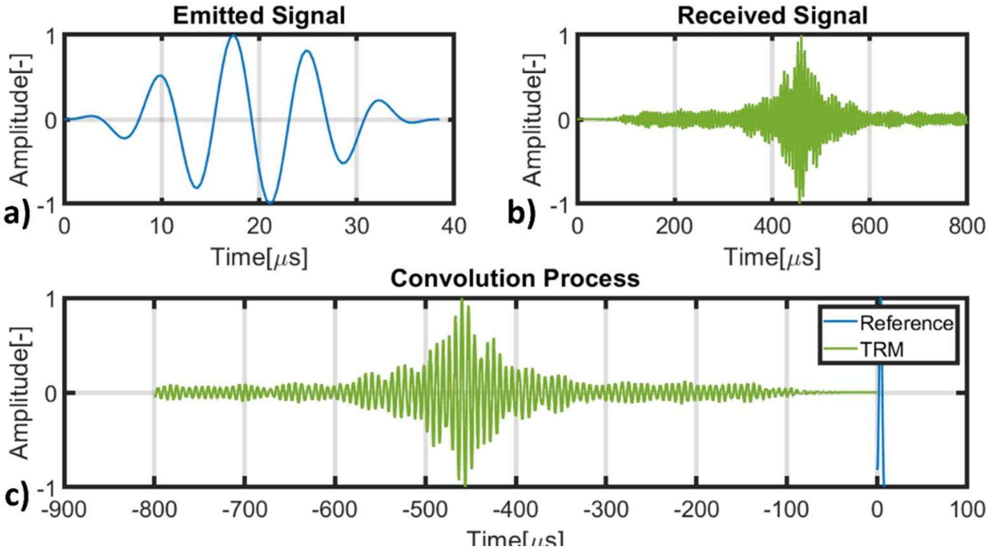

Figure 70. Before failure condition convolution process

Figure 71 shows the result of the signal convolution process for the after-damage condition.

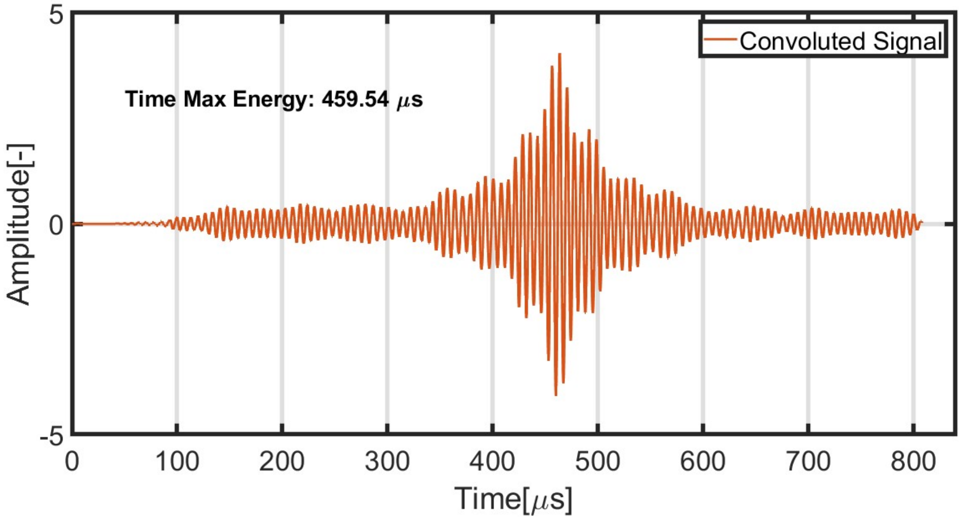

Figure 71. Before failure condition convolution signal

At 459.54 µs was recorded to be the highest amount of energy on the convoluted signal of the before failure condition on the adhesive. Figure 72a indicates the time and section of the convoluted signal that contains the highest amount of energy. Figure 72b shows a time reversed of the convoluted signal. This indicates the position in time of the highest amount of energy of the received signal on Figure 59d.

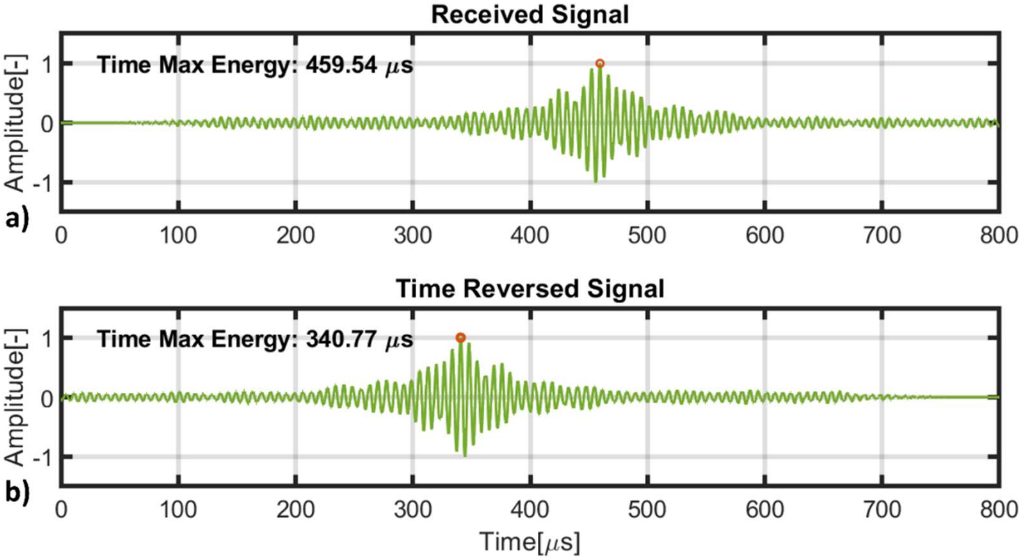

Figure 72. Maximum energy peak before failure condition

As stated in previous analysis, the window for comparison was selected from the time of the maximum energy on the time reversed signal. Figure 73 shows the comparison between the original emitted and the reconstruction of signal of the before failure condition. An R^2-value of 85.13 % was obtained.

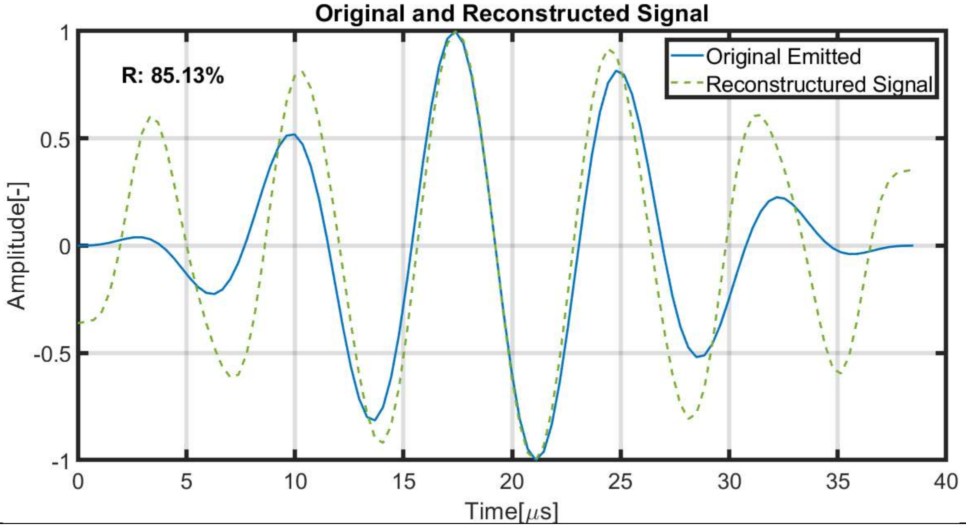

Figure 73. Original and reconstructed signal comparison – before failure condition.

7. Discussion and Conclusion

In this study, an innovative computational TRM has been used for the damage detection on an aluminum-to-aluminum single lap shear bonded joint. The input signal consisted of a 5-cycle Hanning window developed on Matlab^{TM}. This method successfully demonstrated and proves with good cross-correlation coefficient the identification of bonded joints when a pristine condition (97%) is being analyzed and compared to when it contains an introduced damage (90%). This introduced damage is modelled as a circle on the adhesive of the joint, this method of modelling being the common one when introducing a damage of FEA model.

The results obtained of the material characterization, from both the aluminum and the ADV 176/276, allowed to successfully approximate the stress-strain curve of the material to simulate the plastic and failure behavior on the FEA at an element size level. This approximation confirmed that the introduced material information used on the single lap shear bonded joint will behave as in a real tensile test going from linear to plastic behavior until failure. The development of this material model allowed an effective simulation of damage initiation and damage development across the bondline of the joint. This introduced an innovative method to simulate damage in order to detect real-like damage types on structures.

The damage detection process on the single lap shear bonded joint using the innovative method to approximate damage initiation and development on the bondline shown discrepancies across the results. The discrepancy of the results goes from 70% when the SLSJ was at a pristine condition before damage compared to 80% after nucleation of damage and 85% prior failure of the bondline. It is belief that this discrepancy on the results come from an error on the meshing process. More studies and simulations are needed to confirm or reject the viability of this damage detection method.

Although the limitations of the damage size detection, which is a result the frequency of GLWs employed in order to avoid the development of higher Lamb modes and the introduction of a non-linear analysis on the single lap shear bonded joints, the overall result of this study confirms that the TRM can be employed as a damage detection method on single lap shear joints when a damage is artificially induced. The development of a ductile damage evolution model successfully simulates the theoretical behavior of the nucleation of the crack in the SLJS. Further work is needed if a damage detection model using the TRM with the introduction of a real-like damage is intended. Experimental validation of the TRM on SLJS is set to be as future work for the computational results provided in this study.

References

[1] Proset (last) and G. Brothers Inc, “Technical Data ADV - 176 / 276.” Proset, 2015. [Online]. Available: https://www.prosetepoxy.com/wp-content/uploads/ADV-176_ADV-276.pdf

[2] Federal Aviation Administration, “20-107B - Composite Aircraft Structure.” Federal Aviation Administration, 2010. [Online]. Available: https://www.faa.gov/regulations_policies/advisory_circulars/index.cfm/go/document.information/documentID/99693

[3] US government Printing Office, “Federal Aviation Regulations. Title 14-aeronautics and space.” US government Printing Office, 2017. [Online]. Available: https://www.ecfr.gov/current/title-14

[4] N. G. C. Barbosa, R. D. S. G. Campilho, F. J. G. Silva, and R. D. F. Moreira, “Comparison of different adhesively-bonded joint types for mechanical structures,” *Appl. Adhes. Sci.*, vol. 6, no. 1, p. 15, Dec. 2018, doi: 10.1186/s40563-018-0116-1.

[5] G. Scarselli, C. Corcione, F. Nicassio, and A. Maffezzoli, “Adhesive joints with improved mechanical properties for aerospace applications,” *Int. J. Adhes. Adhes.*, vol. 75, pp. 174–180, Jun. 2017, doi: 10.1016/j.ijadhadh.2017.03.012.

[6] T. G. Graciano, “Dynamic Mechanical Analysis of Kissing Bonds in Bonded Joints,” p. 72.

[7] Society of Automotive Engineers and National Institute for Aviation Research (U.S.), Eds., *Composite materials handbook*. Warrendale, Pa.: SAE International on behalf of CMH-17, a division of Wichita State University, 2012.

[8] A. Sengab and R. Talreja, “A numerical study of failure of an adhesive joint influenced by a void in the adhesive,” *Compos. Struct.*, vol. 156, pp. 165–170, Nov. 2016, doi: 10.1016/j.compstruct.2015.12.052.

[9] A. P. Pisharody, B. Blandford, D. E. Smith, and D. A. Jack, “An experimental investigation on the effect of adhesive distribution on strength of bonded joints,” *Appl. Adhes. Sci.*, vol. 7, no. 1, p. 6, Dec. 2019, doi: 10.1186/s40563-019-0122-y.

[10] J. N. Rossettos, P. Lin, and H. Nayeb-Hashemi, “Comparison of the Effects of Debonds and Voids in Adhesive Joints,” *J. Eng. Mater. Technol.*, vol. 116, no. 4, pp. 533–538, Oct. 1994, doi: 10.1115/1.2904324.

[11] M. N. Hashmi, “Revisiting Aloha Airline Flight 243: Corrosion Engineer’s Stand point,” p. 45.

[12] W. M. Ostachowicz, “Damage detection of structures using spectral finite element method,” *Comput. Struct.*, vol. 86, no. 3–5, pp. 454–462, Feb. 2008, doi: 10.1016/j.compstruc.2007.02.004.

[13] V. Giurgiutiu, *Structural Health Monitoring with Piezoelectric Wafer Active Sensors*. Elsevier, 2014. doi: 10.1016/C2013-0-00155-7.

[14] A. Raghavan, “Guided-wave structural health monitoring,” Doctoral Thesis, The University of Michigan, Michigan, 2007. [Online]. Available:

https://deepblue.lib.umich.edu/bitstream/handle/2027.42/77498/Raghavan_PhD_thesis_GWSHM.pdf

[15] US Department of Transportation, “Establishing and Implementing Limit of Validity to Prevent Widespread Fatigue Damage.” US Department of Transportation, 2011. [Online]. Available: https://www.faa.gov/documentLibrary/media/Advisory_Circular/120-104.pdf

[16] C. R. Farrar and K. Worden, “An introduction to structural health monitoring,” *Philos. Trans. R. Soc. Math. Phys. Eng. Sci.*, vol. 365, no. 1851, pp. 303–315, Feb. 2007, doi: 10.1098/rsta.2006.1928.

[17] R. A. Sielski, “Ship Structural Health Monitoring Research at the Office of Naval Research,” *JOM*, vol. 64, no. 7, pp. 823–827, Jul. 2012, doi: 10.1007/s11837-012-0361-x.

[18] R. Lammering, U. Gabbert, M. Sinapius, T. Schuster, and P. Wierach, Eds., *Lamb-Wave Based Structural Health Monitoring in Polymer Composites*. Cham: Springer International Publishing, 2018. doi: 10.1007/978-3-319-49715-0.

[19] D. Balageas, C.-P. Fritzen, and A. Güemes, Eds., *Structural health monitoring*. London ; Newport Beach, CA: ISTE, 2006.

[20] N. M. M. Maia, “A REVIEW ON VIBRATION-BASED STRUCTURAL HEALTH MONITORING WITH SPECIAL EMPHASIS ON COMPOSITE MATERIALS,” p. 49.

[21] J. M. López-Higuera *et al.*, “Fiber optics in structural health monitoring,” Beijing, China, Nov. 2010, p. 78530D. doi: 10.1117/12.876192.

[22] R. Di Sante, “Fibre Optic Sensors for Structural Health Monitoring of Aircraft Composite Structures: Recent Advances and Applications,” *Sensors*, vol. 15, no. 8, pp. 18666–18713, Jul. 2015, doi: 10.3390/s150818666.

[23] S. Das, P. Saha, and S. K. Patro, “Vibration-based damage detection techniques used for health monitoring of structures: a review,” *J. Civ. Struct. Health Monit.*, vol. 6, no. 3, pp. 477–507, Jul. 2016, doi: 10.1007/s13349-016-0168-5.

[24] A. Güemes, A. Fernández-López, P. Díaz-Maroto, A. Lozano, and J. Sierra-Perez, “Structural Health Monitoring in Composite Structures by Fiber-Optic Sensors,” *Sensors*, vol. 18, no. 4, p. 1094, Apr. 2018, doi: 10.3390/s18041094.

[25] S. Gholizadeh, “A review of non-destructive testing methods of composite materials,” *Procedia Struct. Integr.*, vol. 1, pp. 50–57, 2016, doi: 10.1016/j.prostr.2016.02.008.

[26] L. Yaozhong, “A NANOCOMPOSITE-INSPIRED BROADBAND SENSING NETWORK COATING FOR ACOUSTO-ULTRASONICSBASED IN SITU STRUCTURAL HEALTH MONITORING,” Doctoral Thesis, The Honk Kong Polytechnic University, Hong Kong, 2020. [Online]. Available: https://theses.lib.polyu.edu.hk/bitstream/200/11047/3/5512.pdf

[27] A. Vary, “The Acousto-Ultrasonic Approach,” in *Acousto-Ultrasonics*, Boston, MA: Springer, 1988.

[28] A. Zolotkov, “Sound Frequency and Wavelength Calculator,” *TranslatorsCafe*, 2021. https://www.translatorscafe.com/unit-converter/en-US/calculator/sound-frequency-wavelength/ (accessed Nov. 29, 2021).

[29] V. Janapati, F. Kopsaftopoulos, F. Li, S. J. Lee, and F.-K. Chang, “Damage detection sensitivity characterization of acousto-ultrasound-based structural health monitoring techniques,” *Struct. Health Monit.*, vol. 15, no. 2, pp. 143–161, Mar. 2016, doi: 10.1177/1475921715627490.

[30] Z. Su and L. Ye, *Identification of damage using Lamb waves: from fundamentals to applications*. Berlin: Springer-Verlag, 2009.

[31] W. Ostachowicz, P. Kudela, M. Krawczuk, and A. Zak, *Guided Waves in Structures for SHM: The Time-Domain Spectral Element Method*. Chichester, UK: John Wiley & Sons, Ltd, 2012. doi: 10.1002/9781119965855.

[32] E. Onajite, *Seismic Data Analysis Techniques in Hydrocarbon Exploration,*. Elsevier, 2014.

[33] H. Lamb, “On waves in an elastic plate,” *Proc. R. Soc. Lond. A*, vol. 93, no. 1917, pp. 114–128, 1916, doi: doi.org/10.1098/rspa.1917.0008.

[34] D. C. Worlton, “Experimental Confirmation of Lamb Waves at Megacycle Frequencies,” *J. Appl. Phys.*, vol. 32, no. 6, pp. 967–971, Jun. 1961, doi: 10.1063/1.1736196.

[35] J. L. Rose, *Ultrasonic Guided Waves in Solid Media*. New York: Cambridge University Press, 2014. doi: 10.1017/CBO9781107273610.

[36] M. Šofer, P. Ferfecki, and P. Šofer, “Numerical solution of Rayleigh-Lamb frequency equation for real, imaginary and complex wavenumbers,” *MATEC Web Conf.*, vol. 157, p. 08011, 2018, doi: 10.1051/matecconf/201815708011.

[37] E. L. Bolda, R. Y. Chiao, and J. C. Garrison, “Two theorems for the group velocity in dispersive media,” *Phys. Rev. A*, vol. 48, no. 5, pp. 3890–3894, Nov. 1993, doi: 10.1103/PhysRevA.48.3890.

[38] M. Faisal Haider, “Structural Health Monitoring using Ultrasonic Guided Waves and Piezoelectric Wafer Active Sensors,” Doctor of Philosophy, University of South Carolina, 2018.

[39] S. Mahadev Prasad, K. Balasubramaniam, and C. V. Krishnamurthyu, “Structural Health Monitoring of Composite Structures using Lamb wave tomography,” *Smart Mater. Struct.*, vol. 13, no. 2004, pp. 73–79, 2004.

[40] N. Venturini, “Experimental Broadband Signal Reconstruction for Plate-like Structures,” University of Bologna, Bologna, 2019.

[41] W. J. Staszewski, “Ultrasonic/Guided Waves for Structural Health Monitoring,” *Key Eng. Mater.*, vol. 293–294, pp. 49–62, Sep. 2005, doi: 10.4028/www.scientific.net/KEM.293-294.49.

[42] N. Quaegebeur, P. Micheau, P. Masson, and H. Belanger, “STRUCTURAL HEALTH MONITORING OF BONDED COMPOSITE JOINTS USING PIEZOCERAMICS,” p. 11, 2011.

[43] J. He *et al.*, “A multi-feature integration method for fatigue crack detection and crack length estimation in riveted lap joints using Lamb waves,” *Smart Mater. Struct.*, vol. 22, no. 10, p. 105007, Oct. 2013, doi: 10.1088/0964-1726/22/10/105007.

[44] H. Baid, C. Schaal, H. Samajder, and A. Mal, “Dispersion of Lamb waves in a honeycomb composite sandwich panel,” *Ultrasonics*, vol. 56, pp. 409–416, Feb. 2015, doi: 10.1016/j.ultras.2014.09.007.

[45] N. Mori and S. Biwa, “Transmission of Lamb waves and resonance at an adhesive butt joint of plates,” *Ultrasonics*, vol. 72, pp. 80–88, Dec. 2016, doi: 10.1016/j.ultras.2016.07.013.

[46] D. Wang, J. He, X. Guan, J. Yang, and W. Zhang, “A model assessment method for predicting structural fatigue life using Lamb waves,” *Ultrasonics*, vol. 84, pp. 319–328, Mar. 2018, doi: 10.1016/j.ultras.2017.11.017.

[47] M. Philibert, C. Soutis, M. Gresil, and K. Yao, “Damage Detection in a Composite T-Joint Using Guided Lamb Waves,” *Aerospace*, vol. 5, no. 2, p. 40, Apr. 2018, doi: 10.3390/aerospace5020040.

[48] I. Dafydd and Z. Sharif Khodaei, “Analysis of barely visible impact damage severity with ultrasonic guided Lamb waves,” *Struct. Health Monit.*, vol. 19, no. 4, pp. 1104–1122, Jul. 2020, doi: 10.1177/1475921719878850.

[49] E. Wojtczak and M. Rucka, “Wave Frequency Effects on Damage Imaging in Adhesive Joints Using Lamb Waves and RMS,” *Materials*, vol. 12, no. 11, p. 1842, Jun. 2019, doi: 10.3390/ma12111842.

[50] M. Fink, “Time Reversal of Ultrasonic Fields-Part I: Basic Principles,” p. 12, 1993.

[51] M. Fink, D. Cassereau, A. Derode, C. Prada, P. Roux, and M. Tanter, “Time-reversed acoustics,” *Rep. Prog. Phys.*, p. 63, 1999.

[52] H. W. Park, S. B. Kim, and H. Sohn, “Understanding a time reversal process in Lamb wave propagation,” *Wave Motion*, vol. 46, no. 7, pp. 451–467, Nov. 2009, doi: 10.1016/j.wavemoti.2009.04.004.

[53] M. Fink, G. Montaldo, and M. Tanter, “Time-Reversal Acoustics in Biomedical Engineering,” *Annu. Rev. Biomed. Eng.*, vol. 5, no. 1, pp. 465–497, Aug. 2003, doi: 10.1146/annurev.bioeng.5.040202.121630.

[54] G. F. Edelmann, W. S. Hodgkiss, S. Kim, W. A. Kuperman, H. C. Song, and T. Akal, “Underwater acoustic communication using time reversal,” in *MTS/IEEE Oceans 2001. An Ocean Odyssey. Conference Proceedings (IEEE Cat. No.01CH37295)*, Honolulu, HI, USA, 2001, vol. 4, pp. 2231–2235. doi: 10.1109/OCEANS.2001.968345.

[55] R. K. Ing and M. Fink, “Time-reversed Lamb waves,” *IEEE Trans. Ultrason. Ferroelectr. Freq. Control*, vol. 45, no. 4, pp. 1032–1043, Jul. 1998, doi: 10.1109/58.710586.

[56] J. R. Pettit, A. Walker, P. Cawley, and M. J. S. Lowe, “A Stiffness Reduction Method for efficient absorption of waves at boundaries for use in commercial Finite Element codes,” *Ultrasonics*, vol. 54, no. 7, pp. 1868–1879, Sep. 2014, doi: 10.1016/j.ultras.2013.11.013.

[57] J.-P. Berenger, “A perfectly matched layer for the absorption of electromagnetic waves,” *J. Comput. Phys.*, vol. 114, no. 2, pp. 185–200, Oct. 1994, doi: 10.1006/jcph.1994.1159.

[58] E. A. Skelton, S. D. M. Adams, and R. V. Craster, “Guided elastic waves and perfectly matched layers,” *Wave Motion*, vol. 44, no. 7, pp. 573–592, Aug. 2007, doi: 10.1016/j.wavemoti.2007.03.001.

[59] F. D. Hastings, J. B. Schneider, and S. L. Broschat, “Application of the perfectly matched layer (PML) absorbing boundary condition to elastic wave propagation,” *J. Acoust. Soc. Am.*, vol. 100, no. 5, pp. 3061–3069, Nov. 1996, doi: 10.1121/1.417118.

[60] M. Israeli and S. A. Orszag, “Approximation of radiation boundary conditions,” *J. Comput. Phys.*, vol. 41, no. 1, pp. 115–135, May 1981, doi: 10.1016/0021-9991(81)90082-6.

[61] M. Castaings and C. Bacon, “Finite element modeling of torsional wave modes along pipes with absorbing materials,” *J. Acoust. Soc. Am.*, vol. 119, no. 6, pp. 3741–3751, Jun. 2006, doi: 10.1121/1.2197807.

[62] M. Castaings, C. Bacon, B. Hosten, and M. V. Predoi, “Finite element predictions for the dynamic response of thermo-viscoelastic material structures,” *J. Acoust. Soc. Am.*, vol. 115, no. 3, pp. 1125–1133, Mar. 2004, doi: 10.1121/1.1639332.

[63] W. Ke, M. Castaings, and C. Bacon, “3D finite element simulations of an air-coupled ultrasonic NDT system,” *NDT E Int.*, vol. 42, no. 6, pp. 524–533, Sep. 2009, doi: 10.1016/j.ndteint.2009.03.002.

[64] F. Falcetelli, “Modelling of Pencil-Lead Break Acoustic Emission Sources using the Time Reversal Technique,” University of Bologna, Bologna, 2018.

[65] F. Li, H. Yuan, and H. Liu, “Implementation of metal ductile damage criteria in Abaqus FEA,” *J. Phys. Conf. Ser.*, vol. 1906, no. 1, p. 012058, May 2021, doi: 10.1088/1742-6596/1906/1/012058.

[66] J. R. Rice and D. M. Tracey, “PII: 0022-5096(69)90033-7 | Elsevier Enhanced Reader.” https://reader.elsevier.com/reader/sd/pii/0022509669900337?token=60492F3F877170F0066069F4F62A103C351BFA276A678712377A597A74C0B1022F6BF301D48FFB7297B15FCD00CAB777&originRegion=us-east-1&originCreation=20220615194729 (accessed Jun. 15, 2022).

[67] G. Trattnig, T. Antretter, and R. Pippan, “Fracture of austenitic steel subject to a wide range of stress triaxiality ratios and crack deformation modes,” *Eng. Fract. Mech.*, vol. 75, no. 2, pp. 223–235, Jan. 2008, doi: 10.1016/j.engfracmech.2007.03.021.

[68] “Elasto-plastic Materials | Materials | SimScale.” https://www.simscale.com/docs/simulation-setup/materials/plastic-materials/ (accessed Jun. 15, 2022).

[69] ABAQUS DOCS, “Damage evolution and element removal for ductile metals,” Documentation.

[70] T. Derrick, “Time Series Analysis: The Cross-Correlation Function | Request PDF.” https://www.researchgate.net/publication/331998942_Time_Series_Analysis_The_Cross-Correlation_Function (accessed Jun. 22, 2022).

[71] MATLAB, “Cross-correlation - MATLAB xcorr.” https://www.mathworks.com/help/matlab/ref/xcorr.html#mw_01b546db-b642-4f02-8625-16078810d80f (accessed Jun. 22, 2022).

[72] B. Xu and V. Giurgiutiu, “Single Mode Tuning Effects on Lamb Wave Time Reversal with Piezoelectric Wafer Active Sensors for Structural Health Monitoring,” *J. Nondestruct. Eval.*, vol. 26, no. 2–4, pp. 123–134, Nov. 2007, doi: 10.1007/s10921-007-0027-8.

[73] H. Sohn, H. W. Park, K. H. Law, and C. R. Farrar, “Damage Detection in Composite Plates by Using an Enhanced Time Reversal Method,” *J. Aerosp. Eng.*, vol. 20, no. 3, pp. 141–151, Jul. 2007, doi: 10.1061/(ASCE)0893-1321(2007)20:3(141).

[74] B. Poddar, C. R. Bijudas, M. Mitra, and P. M. Mujumdar, “Damage detection in a woven-fabric composite laminate using time-reversed Lamb wave,” *Struct. Health Monit.*, vol. 11, no. 5, pp. 602–612, Sep. 2012, doi: 10.1177/1475921712449510.

[75] H. Sohn, Hyun Woo Park, K. H. Law, and C. R. Farrar, “Combination of a Time Reversal Process and a Consecutiv Outlier Analysis for Baseline-free Damage Diagnosis,” *J. Intell. Mater. Syst. Struct.*, vol. 18, no. 4, pp. 335–346, Apr. 2007, doi: 10.1177/1045389X0606629.

[76] N. Jayakody, A. Khalili, and R. Jha, “Structural Health Monitoring of Bonded Joints using Modified Time Reversal Method,” in *2018 AIAA/AHS Adaptive Structures Conference*, Kissimmee, Florida, Jan. 2018. doi: 10.2514/6.2018-0563.

[77] F. Du, C. Xu, G. Wu, and J. Zhang, “Preload Monitoring of Bolted L-Shaped Lap Joints Using Virtual Time Reversal Method,” *Sensors*, vol. 18, no. 6, Art. no. 6, Jun. 2018, doi: 10.3390/s18061928.

[78] J. Wang and Y. Shen, “An enhanced Lamb wave virtual time reversal technique for damage detection with transducer transfer function compensation,” *Smart Mater. Struct.*, vol. 28, no. 8, p. 085017, Aug. 2019, doi: 10.1088/1361-665X/ab1fc8.

[79] C. Xu, G. Wu, F. Du, W. Zhu, and S. H. Mahdavi, “A Modified Time Reversal Method for Guided Wave Based Bolt Loosening Monitoring in a Lap Joint,” *J. Nondestruct. Eval.*, vol. 38, no. 4, p. 85, Dec. 2019, doi: 10.1007/s10921-019-0626-1.

[80] C. Gauthier, M. Ech-Cherif El-Kettani, J. Galy, M. Predoi, and D. Leduc, “Structural adhesive bonding characterization using guided Lamb waves and the vertical modes,” *Int. J. Adhes. Adhes.*, vol. 98, p. 102467, Apr. 2020, doi: 10.1016/j.ijadhadh.2019.102467.

[81] F. Falcetelli, N. Venturini, M. B. Romero, M. J. Martinez, S. Pant, and E. Troiani, “Broadband signal reconstruction for SHM: An experimental and numerical time reversal methodology,” *J. Intell. Mater. Syst. Struct.*, vol. 32, no. 10, pp. 1043–1058, Jun. 2021, doi: 10.1177/1045389X20972474.

[82] M. Kannusamy, S. Kapuria, and S. Sasmal, “An efficient Lamb wave-based virtual refined time-reversal method for damage localization in plates using broadband measurements,” *Ultrasonics*, vol. 124, p. 106767, Aug. 2022, doi: 10.1016/j.ultras.2022.106767.

[83] J. C. Pineda Allen and C. T. Ng, “Debonding detection at adhesive joints using nonlinear Lamb waves mixing,” *NDT E Int.*, vol. 125, p. 102552, Jan. 2022, doi: 10.1016/j.ndteint.2021.102552.

[84] E28 Committee, “E8 - Test Methods for Tension Testing of Metallic Materials,” ASTM International. doi: 10.1520/E0008_E0008M-21.

[85] D20 Committee, “D638 - Test Method for Tensile Properties of Plastics,” ASTM International. doi: 10.1520/D0638-14.

[86] “Grasshopper3 USB3 | Teledyne FLIR.” https://www.flir.com/products/grasshopper3-usb3?vertical=optical+gas&segment=solutions (accessed Jun. 15, 2022).

[87] "Fujinon CF25HA-1 1" 25mm F1.4 Manual Iris C-Mount Lens, 1.5 Megapixel Rated," *RMA Electronics, Inc.* https://www.rmaelectronics.com/fujinon-cf25ha-1/ (accessed Jun. 15, 2022).

[88] D14 Committee, "D1002 - Test Method for Apparent Shear Strength of Single-Lap-Joint Adhesively Bonded Metal Specimens by Tension Loading (Metal-to-Metal)," ASTM International. doi: 10.1520/D1002-10R19.

[89] "Vallen AE-Suite Software." Vallen Systéme. [Online]. Available: https://www.vallen.de/

[90] V. Piefort, "Finite Element Modelling of Piezoelectric Active Structures," p. 154.

[91] M. Martinez, "Finite element model of structures with piezoelectric elements," Doctor of Philosophy, Carleton University, Ottawa, Ontario, 2006. doi: 10.22215/etd/2006-06428.

[92] F. Moser, L. J. Jacobs, and J. Qu, "Modeling elastic wave propagation in waveguides with the finite element method," *NDT E Int.*, vol. 32, no. 4, pp. 225–234, Jun. 1999, doi: 10.1016/S0963-8695(98)00045-0.

[93] "Examining Spatial (Grid) Convergence." https://www.grc.nasa.gov/www/wind/valid/tutorial/spatconv.html (accessed Jun. 06, 2022).